RCA Review

March 1974 Volume 35 No. 1
RCARCI 35(1) 1-164 (1974)

RCA Review, published quarterly in March, June, September and December by RCA Research and Engineering, RCA Corporation, Princeton, New Jersey 08540. Entered as second class matter July 3, 1950 under the Act of March 3, 1879. Second-class postage paid at Princeton, New Jersey, and at additional mailing offices. Effective Jan. 1, 1971, subscription rates as follows: United States and Canada: one year $6.00, two years $10.50, three years $13.50; in other countries, one year $6.40, two years $11.30, three years $14.70. Single copies (except for special issues) up to five years old $3.00.

,4r

RCA Review

A technical journal published quarterly
by RCA Research and Engineering
In cooperation with the subsidiaries
and divisions of RCA.

Contents

An Introduction to the Science and Technology of Liquid Crystals

March 1974 Volume 35 Number 1

Control of Blooming in Charge-Coupled Imagers*

W. F. Kosonocky, J. E. Carnes, M. G. Kovac, P. Levine, and F. V. Shallcross**

RCA Laboratories, Princeton, N. J. 08540

R. L. Rodgers III

Electronic Components, Lancaster, Pa.

Abstract—Four approaches are described for controlling blooming in charge-coupled imagers. They are based on (a) an operational method that localizes blooming by accumulation regions around each sensing element, (b) static anti-blooming structures involving polysilicon blooming barrier gates, (c) dynamic anti-blooming structures employing ion-implanted blooming barriers, and (d) dynamic structures employing stepped-oxide blooming barriers. Experimental results are presented for charge-coupled area imagers with localization of blooming by the accumulation mode and for charge-coupled line imagers with types (c) and (d) dynamic blooming controls.

1. Introduction

While silicon-based imaging devices are not subject to material damage in the presence of optical overloads such as that experienced by earlier types of targets, the silicon devices do suffer from the spreading of overload-generated charge into adjacent regions. The phenomenon is called "blooming" and is especially objectionable in devices with high

* Except for the new data on the operation of the 256 × 160 charge-coupled imager, the experimental results described in this paper were presented at the 1972 IEEE International Electron Devices Meeting, Wash., D.C., Dec. 4-6, 1972, under the title "Dynamic Range and Blooming Control in Charge-Coupled Imagers."

** Presently with Dytron, Inc., Waltham, Massachusetts 02154.

sensitivity, since normal light sources become very large optical overloads in a low-light-level environment.

The effect of blooming on the operation of a charge-coupled imager is demonstrated in Fig. 1. The photographs shown here are detected by a 256 × 160 three-phase vertical frame transfer CCI.[1] The top

(a)

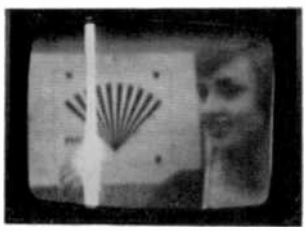

(b)

Fig. 1—T.V. pictures detected with 3-phase 256 × 160 charge-coupled image sensor.
(a) a nonblooming picture.
(b) The girl is holding a lighted match that results in blooming.

photograph shows a scene with no optical overload. The blooming in the lower photograph results from turning on an essentially point-light-source overload. The white region in the photograph covers an area that is considerably larger than the light source. The excess charge first spreads along the vertical lines. But under very intense overload it will also reach to the output register and produce a blooming in the horizontal direction. This clearly demonstrates the objectionable nature of blooming in a charge-coupled imager.

To make charge-coupled imagers capable of operation without blooming in the presence of large optical overloads, several methods of blooming control have been proposed and tested. The first technique is an operational one requiring no special structure within the CCI itself. It consists of holding one or two phases of the device in accumulation during light integration, and will be referred to as the

accumulation mode. The tests indicate this mode is useful in partially localizing blooming due to moderate optical overloads.

To obtain more effective control of blooming, several anti-blooming structures incorporated in CCI's have been proposed and test devices fabricated. These involve diffused bus drain lines adjacent to each CCD channel, which are used to remove optical-overload-generated charge before it can spread to adjacent locations. The various tech-

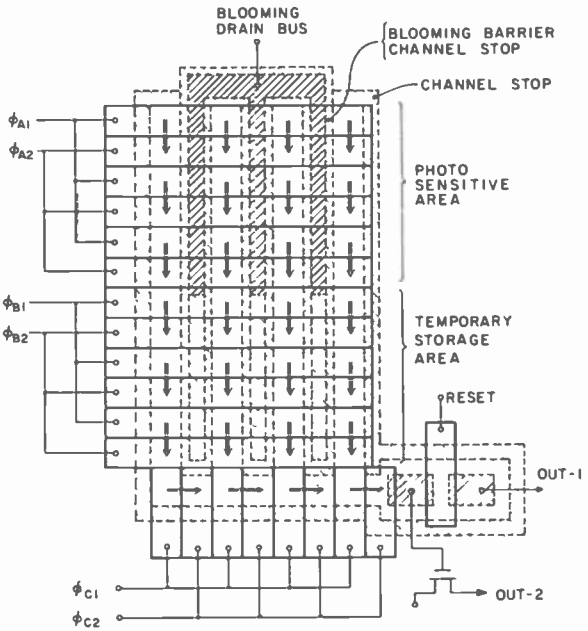

Fig. 2—Schematic of a 2-phase frame-transfer charge-coupled imager with blooming control.

niques differ in their method of producing a channel-confining barrier that controls the flow of charge into the blooming buses. The three basic categories involve barriers created by (1) field-shield gates, (2) diffused or ion-implanted channel regions, and (3) stepped-oxide channel stop regions. These three types of anti-blooming structures can be incorporated in the vertical frame-transfer CCI's very simply by placing the blooming drains in the channel stop regions between the adjacent CCD channels of the photosensitive area, as shown in Fig. 2. The maximum optical overloads that can be tolerated are limited in this case by the smearing effect, which occurs during the frame transfer time when the charge pattern is shifted from the photosensitive area to the temporary storage area. To avoid blooming as

well as smearing, one must incorporate optical shuttering during frame transfer or use a design of charge-coupled imager that has separate photosensitive elements scanned by nonilluminated charge-coupled registers.

2. Methods of Blooming Control

2.1 Accumulation Mode—An Operational Method of Blooming Control

As mentioned, one method of limiting blooming control in an illuminated register device, the accumulation method, is an operational method that does not require any additional structure to be built into the

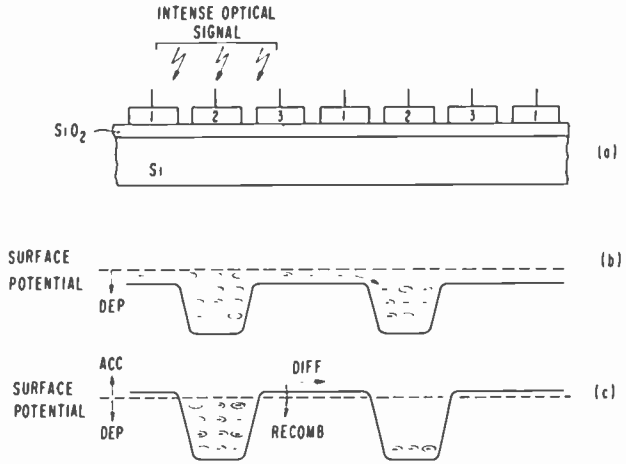

Fig. 3—Normal and accumulation modes of operation of charge-coupled imager.
(a) Cross-sectional view of three-phase CCD, (b) illustrating the normal mode of operation, and (c) the accumulation mode of operation for blooming control.

sensor. The concept of the accumulation mode is illustrated in Fig. 3 for the case of a three-phase CCD with diffusion channel stops. The standard mode and the accumulation mode are illustrated in the two surface potential diagrams. In the "standard mode" of operation, all three of the phases are biased into slight depletion, and in addition, the #2 electrodes are biased so as to form deep depletion regions for the collection of photogenerated carriers. In the case of an intense optical overload, the photogenerated carriers will fill up the wells and then spill down the channel into adjacent cells.

In the accumulation mode, the #1 and #3 electrodes are biased so that the underlying interface is in accumulation. This establishes a barrier and prevents the excess minority carriers from spilling freely

down the channel, since they will tend to recombine with holes in the accumulation regions.

2.2 Static Blooming Control

The operation of anti-blooming structure in which polysilicon field-shield channel stop gates are used to form the barriers between the illuminated CCD channels and the blooming bus drains is illustrated in Figs. 4 and 5. A CCI with two-phase polysilicon-aluminum gate charge-coupling structure is shown in this example. Fig. 4(a) shows

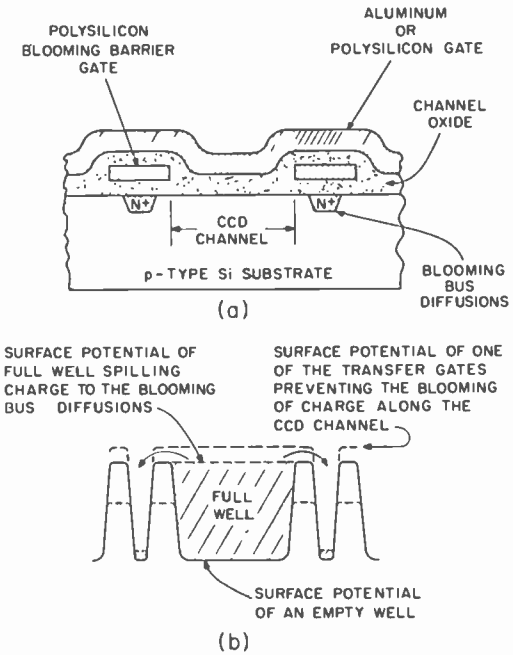

Fig. 4—Cross-sectional view perpendicular to charge flow of static blooming control structure using polysilicon field shield gates (a) and resulting surface potential (b). (Note: as shown by the dotted lines, the blooming barrier potential determines the size of the well.)

a cross-section of the CCD channel perpendicular to charge flow. The polysilicon blooming barrier gate is connected to an external bias that allows control of the barrier between the actual channel and the n+ diffusion used as the sink. The surface potential diagram is shown in Fig. 4(b). We refer to this method as the "static barrier" method because the blooming barrier can be set and controlled independently

of the phase clock voltages. The potential well is two dimensional—having four sides to it. The dashed line shows the surface potential of the transfer gates adjusted to prevent the blooming of charge along the channel. The potential of the blooming barrier set by the polysilicon electrode is slightly lower than the barrier set by the transfer gate. Thus, the excess charge will spill from the full well into the n+ blooming bus before it can spill down the channel. The cross-section of the structure along the channel and the potential profile is shown in Fig. 5. As shown here, the potential along the blooming barrier must always be below the highest barrier of the two-phase transfer electrodes in order to permit sideways spillage of the excess charge signal.

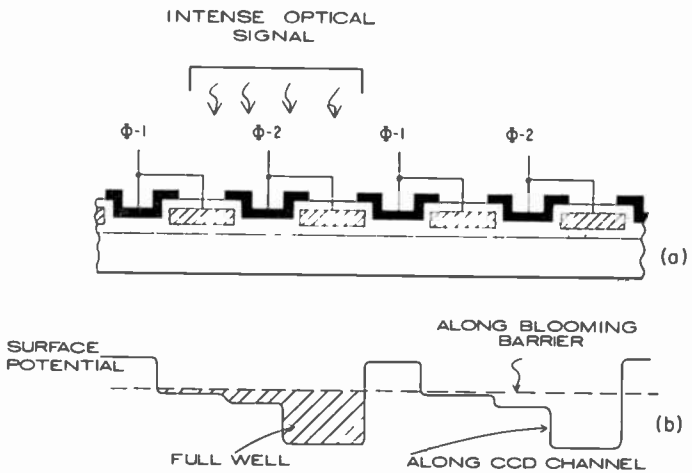

Fig. 5—Longitudinal cross section of structure shown in Figure 4(a) and resulting surface potential along the CCD channel during the optical integration time (b).

From Fig. 5(b) it is apparent that if the blooming barrier surface potential remains unchanged during the charge read-out period, loss of charge from the transferring packets into the blooming bus can occur. Thus, the optimum performance of this type of blooming control requires that the voltage applied to the blooming barrier gate during read-out be different from that applied during the integration period.

The independent control of the blooming barrier potential in the case of the static anti-blooming structure can, however, be used to provide an electronic shutter action. In this case, during the first part of the optical integration time, the blooming barrier is

adjusted so that all of the detected charge is removed by the n+ blooming drains. No charge is collected during this time and the effective integration time is reduced. The application of a large positive potential to the blooming drain diffusion will also control the sensitivity of the CCD sensor if the optical image is introduced on the back side of the substrate. This type of sensitivity control, however, is not very effective for radiation in the long wavelength region of the silicon absorption spectrum. Finally, the blooming control scheme illustrated in Figs. 4 and 5 does not require much more additional processing than structures employing the polysilicon guard rings for channel stops.[2] The blooming bus diffusion can be made at the same time as the normal source and drain diffusions for the CCI array.

2.3 Dynamic Blooming Control Methods

Unlike the static method (just described), which allows control of the blooming barrier height by an external voltage, the dynamic methods use the interaction of the phase voltage and an ion-implanted region or a stepped-oxide structure to determine the barrier.

a. Ion-implanted Blooming Barrier

The construction and operation of a CCI with a dynamic anti-blooming structure employing ion-implanted blooming barriers is illustrated in Figs. 6 and 7 for the case of a three-phase aluminum gate CCI with diffusion channel stops. The cross-sectional view of illuminated register perpendicular to the charge flow is shown in Fig. 6(a). If this device did not have the blooming control feature, heavily doped p+ diffused channel stops would define the channel. In the structure shown here, the diffused channel stop is replaced by an ion-implanted region and an n+ blooming bus. For a p-type substrate in the range of 10^{14} to 10^{15} cm^{-3}, a typical implant level would be in the 10^{16} cm^{-3} range. The spilling of the excess charge due to an optical overload into the blooming bus drains as illustrated by the surface potentials in Fig. 6(b). Note that the top dashed line shows the surface potential of one of the transfer gates that prevents the blooming of charge along the CCD channel.

The self-limiting action of the dynamic blooming method is illustrated in Fig. 7 which shows the cross-section of the structure and the surface potential profile along the CCD channel. Note that unlike the previously described static blooming control (see Fig. 5[b]) the blooming barrier potential (shown as dashed line) depends on the gate voltage and dips to a minimum value at the storage-well locations. When a well fills up due to intense optical overload, the surface poten-

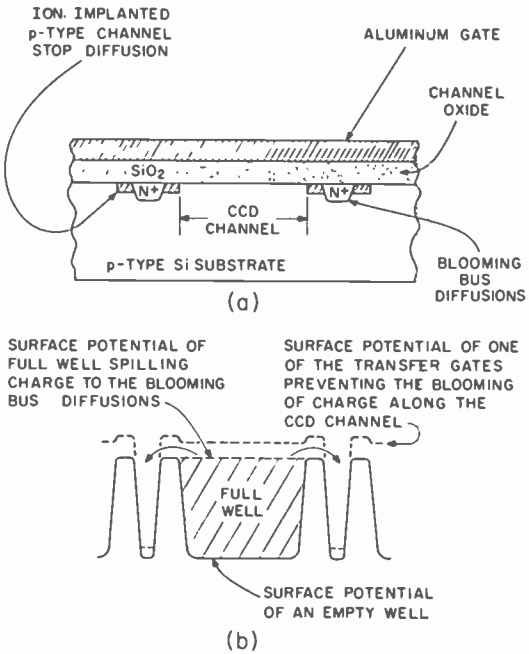

Fig. 6—Cross-sectional view perpendicular to charge flow of dynamic bloom-control structure using ion-implanted regions (a) and resulting surface potential (b).

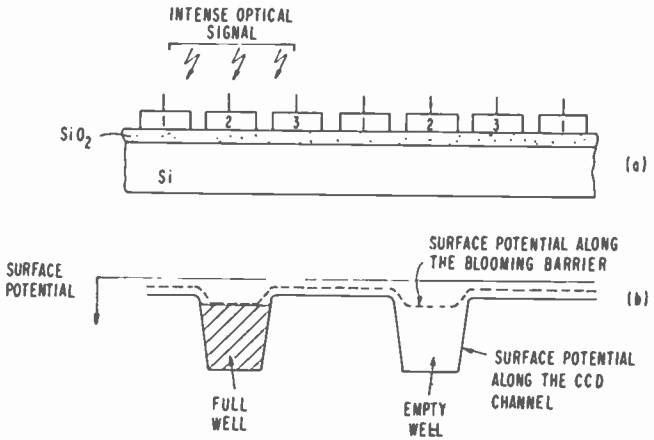

Fig. 7—Longitudinal cross-section of structure shown in Figure 6, and resulting surface potential along the CCD channel.

tial at the location rises only to the point where it meets this minimum surface potential along the blooming barrier.

The expected values of surface potentials for one specific anti-blooming structure with ion-implanted barriers is shown in Fig. 8.

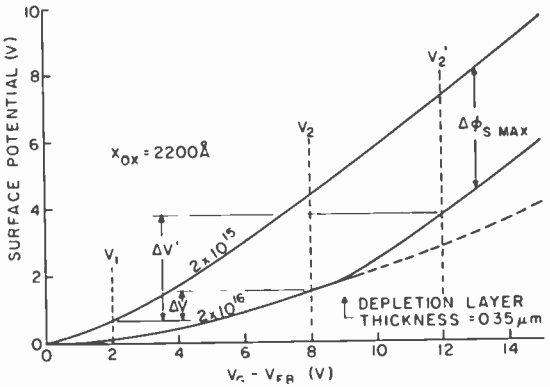

Fig. 8—Surface potentials as function of gate voltage for a dynamic anti-blooming structure with ion-implanted channel stops.

The upper curve represents the surface potential in the channel for substrate doping of $2 \times 10^{15}\,cm^{-3}$; the lower curve is the surface potential in the ion-implanted barrier region approximated by a 0.35μm thick layer with doping of $2 \times 10^{16}\,cm^{-3}$. The knee in the bottom curve corresponds to the point where the ion-implanted region is completely depleted. Assuming the clock voltages vary between V_1 and V_2, ΔV represents the difference between the barrier potential in the CCD channel under the transfer gates with clock voltage V_1 and the minimum blooming barrier potential under the storage gate with clock voltage V_2. However, if the clock voltage excursion $(V_2' - V_1)$ is made to exceed the knee of the bottom curve, the resulting potential difference $\Delta V'$ and the maximum charge stored tends to become independent of the value V_2' similar to the operation of a CCD with an ion-implanted barrier.[3]

b. Stepped-oxide blooming barrier

A second type of dynamic method of blooming control in illuminated registers is the stepped-oxide-barrier-method. This type of anti-blooming structure is most compatible with two-phase polysilicon-aluminum

gate construction, and this type of device was therefore used to demonstrate its operation. Experimental results for such line sensors are presented in Sec. 3.3. The construction and the operation of this type of structure is shown in Figs. 9, 10, and 11. The operation of

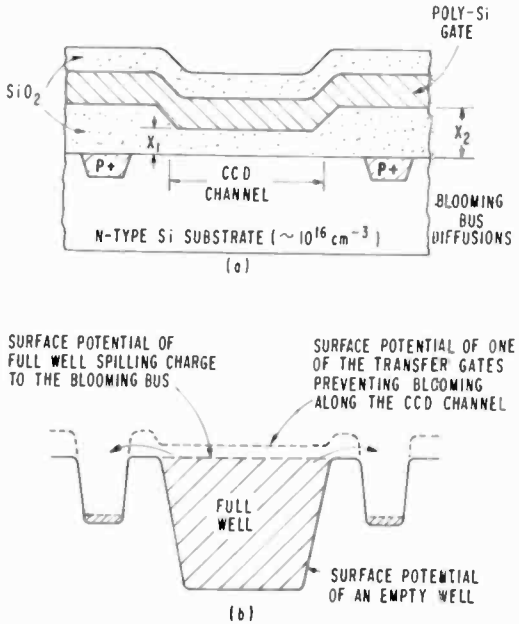

Fig. 9—Cross-sectional view perpendicular to charge flow of dynamic blooming control structure using stepped-oxide blooming barriers (a) and resulting surface potential (b)

this dynamic anti-blooming structure with stepped-oxide blooming barrier is similar to the ion-implanted case, except for additional constraints required to satisfy the two-phase operation. As shown in Fig. 9 the ion-implanted regions have been replaced by stepped-oxides with thickness X_2 as compared to the thickness of X_1 of CCD channels under the polysilicon gates. The charge-coupling structure and the surface potential profile along the CCD channel is shown in Fig. 10. Fig. 11 shows the expected surface potential variations as a function of gate voltage for an n-type substrate with doping density of 10^{16} type of structure is shown in Figs. 9, 10, and 11. The operation of cm^{-3} and oxide thicknesses $X_1 = 1000$Å, $X_2 = 2000$Å, and $X_3 = 2400$Å. The thickness of the channel oxides X_1 and X_3 under the polysilicon and the aluminum gates, respectively, were chosen for

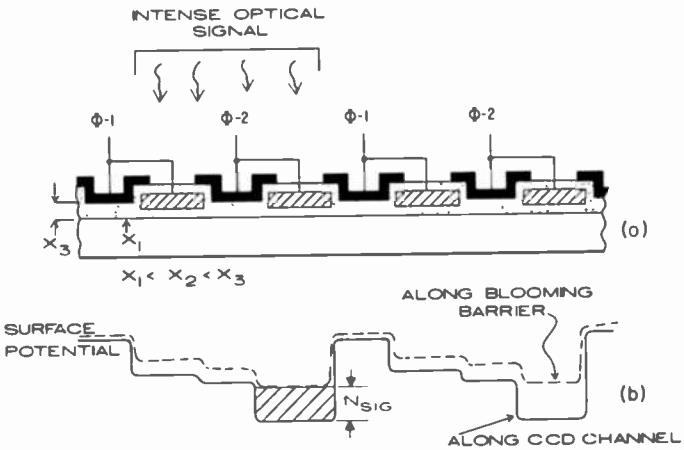

Fig. 10—(a) Longitudinal view of structure shown in Fig. 9 and (b) resulting surface potential along the CCD channel.

optimum two-phase operation for a substrate doping[4] of $10^{16}cm^{-3}$. The blooming barrier oxide under the polysilicon gates ($X_2 = 2000Å$) was chosen so that the maximum charge signal that could be stored is slightly smaller (by $\Delta V'''$) than the full well. This requires that $X_1 < X_2 < X_3$.

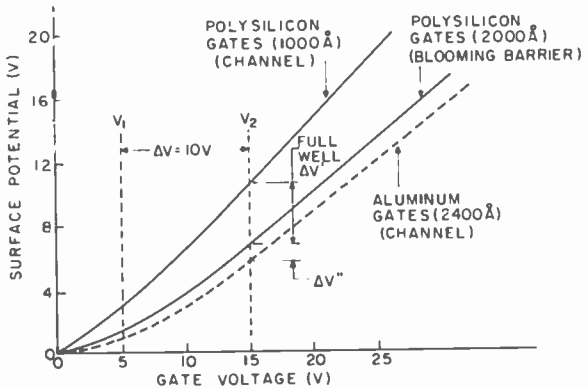

Fig. 11—Surface potentials as function of gate voltage for a dynamic anti-blooming structure with stepped-oxide blooming barrier.

3. Experimental Results

3.1 Operational Mode

Operational blooming control was tested on a 256 × 160 element, three-phase, charge-coupled imager having illuminated registers and frame storage. A schematic of this device is given in Fig. 12. Charge was

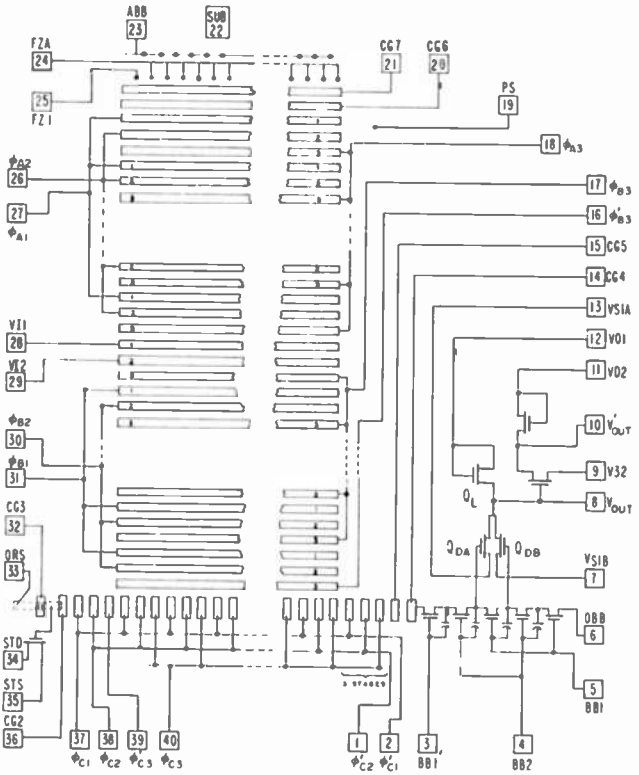

Fig. 12—Schematic of the 256 × 160 element charge-coupled image sensor.

collected during the optical integration period under phase A2. The area under phase A1 and phase A3 were accumulated during the integration period. The accumulated areas electronically extend the channel stops around each image storage cell preventing a free flow of any excess detected charge along the vertical registers. During the vertical blanking time, the charge pattern was transferred to the opaqued "B" storage register. The image is transferred, one line at a time, into the output register.

The effectiveness of this method was demonstrated by placing a shiny chrome ball in a scene illuminated by a bright light two feet from the ball and to the left of the scene. Fig. 13 shows a comparison of the results with and without the operational accumulation method of blooming control. Without the control, the characteristic vertical blooming stripe is present. With blooming control, very little blooming

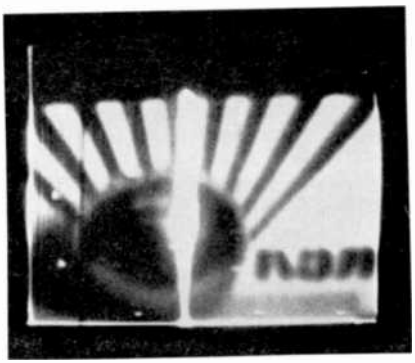

Normal Mode

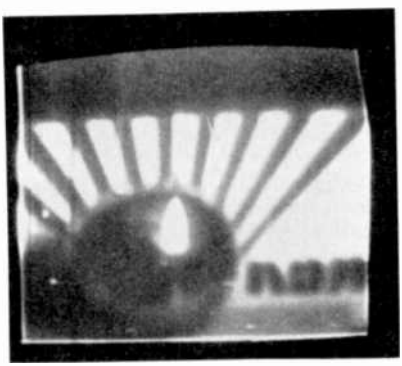

Low Blooming Mode

Fig. 13—256 × 160 element CCD image sensor operating in normal mode and with operational blooming control. Object is a chrome ball illuminated by a bright light two feet to the left of the scene.

is present. The specular overload in this highlight was greater than 10 times the maximum signal capability. Another, more recent, example of the effectiveness of the operational method for blooming control is shown in Fig. 14. Here, a fluorescent lamp represents an excessive optical overload.

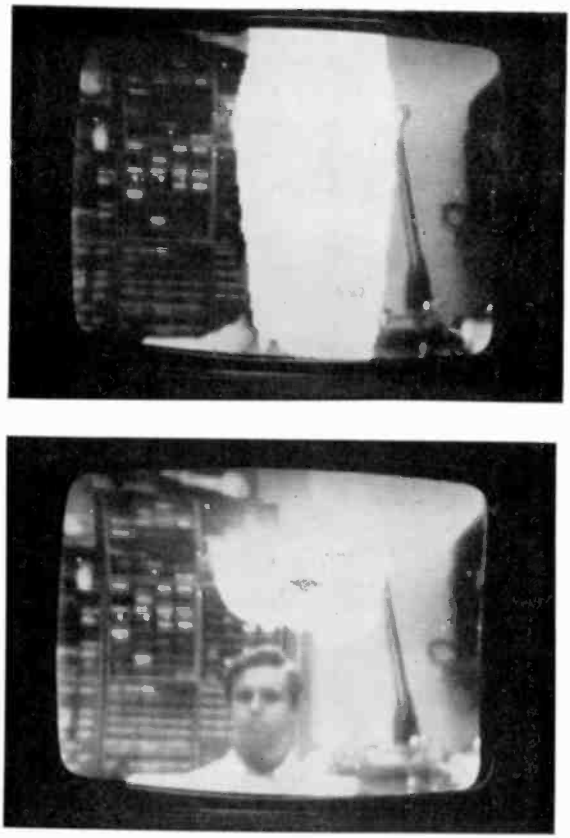

Fig. 14—256 × 160 element CCD image sensor operating (top) in normal mode and (bottom) with operational blooming control. A fluorescent lamp causes the optical overload.

3.2 Three-Phase Line Sensor with Ion-Implanted Blooming Barriers

The dynamic blooming control approach was demonstrated with both three-phase and two-phase line sensors. A photomicrograph of a 130 stage, three-phase, illuminated register CCD with ion-implanted blooming barriers is shown in Fig. 15.

The test structure employs 0.2-mil (5μm)-wide aluminum gates with 0.1-mil gaps. The 1-mil-wide channel has n+ diffused antiblooming buses on each side, separated from the channel by 0.3 mil (8μm) ion-implanted blooming barrier regions. The samples have been made on 5-8 ohm-cm, (100) oriented, p-type silicon wafers.

The ion implantation was carried out through the channel oxide

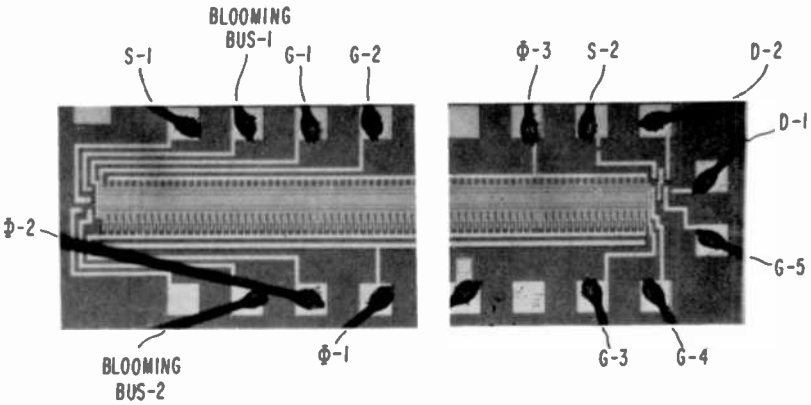

Fig. 15—130-stage, three-phase register with dynamic blooming control (ion-implanted barriers).

using 100-keV boron ions with a dose of either 7×10^{11} or 1.4×10^{12}cm^{-2}. To avoid channel effects, the implantation was performed at an angle of 7° to the wafer normal. Under these conditions, for the smaller dose, the maximum implanted boron concentration was calculated to be 3×10^{16}cm^{-3}, occurring at a depth of 0.12 μm into the silicon. The concentration was calculated to fall to 1×10^{15}cm^{-3} at 0.37 μm into the silicon. The calculated implant distribution before and after anneal is shown in Fig. 16.

Measurements of the threshold voltages in MOS test devices on

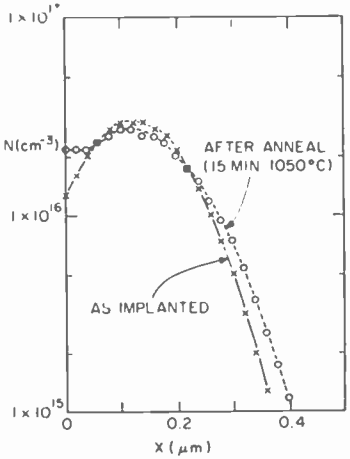

Fig. 16—Calculated implant distribution before and after anneal.

the chips indicated that compared to devices without implanted channels those with implanted channel regions had thresholds shifted approximately in proportion to the implant dosage; substrate doping had little effect on the amount of shift. The observed shifts for a $7 \times 10^{11}cm^{-2}$ dose were 2.1 V for a substrate doping of $2 \times 10^{15}cm^{-3}$ and 2.3 V for a doping of $5 \times 10^{14}cm^{-3}$. For a $1.4 \times 10^{12}cm^{-2}$ dose, the shift was 3.9 V on a $5 \times 10^{14}cm^{-3}$ substrate. Channel oxides were 2200 ± 200 Å thick. We have also built a similar line-scan device that has the standard diffused channel stops instead of the ion-implanted

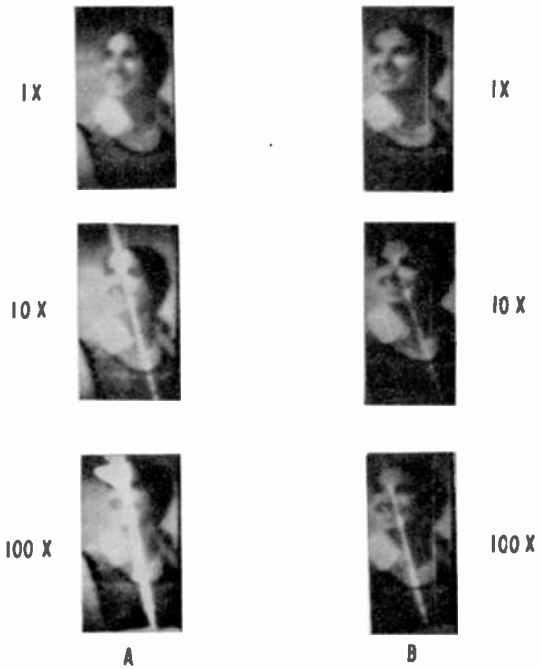

Fig. 17—Line scan pictures taken with devices similar to those shown in Figure 15: (A) without blooming control and (B) with blooming control.

barriers and the n+ blooming buses. Fig. 17 shows line-scan pictures obtained with each of these devices. The column of photographs on the left is for the line scanner with no blooming control. Electronic scan was in the horizontal direction, mechanical scan was in the vertical. At the top left is a picture produced with the illumination adjusted so that the highlights are just saturating. Next is a picture produced by cutting a slit in a neutral density filter (O.D. = 1). The incident illumination was increased to again bring the highlights in

the filtered regions just into saturation. Therefore, the highlights in the diagonal slit are overloaded by 10 ×. At the bottom is a photograph similar to the above, except the O.D. of the neutral-density filter was 2. Therefore, highlights in the slit are now at 100 × saturation. The blooming is apparent.

The column of photographs on the right shows the results of the same series of experiments carried out using the device shown in Fig. 15. The highlights in the slit were at 10 × and 100 ×, respectively. The control of blooming is evident.

In both cases the integration period was 5 msec and the readout was at 200 KHz giving an integrate-time to clock-period ratio of 10^3 so that optical smear was not a problem.

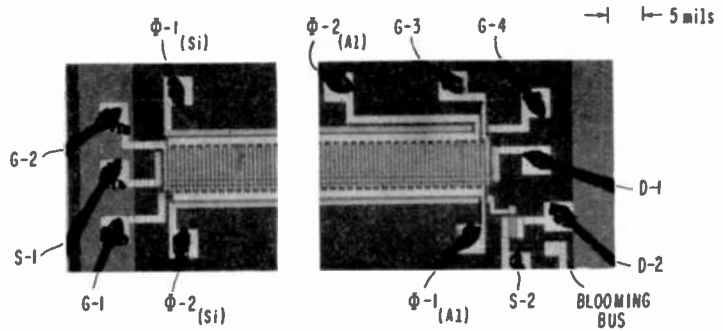

Fig. 18—128-stage, two-phase register with dynamic blooming control stepped-oxide barrier).

3.3 Two-Phase Line Sensors with Stepped-Oxide Blooming Barriers

The dynamic blooming control with stepped-oxide blooming barrier was studied with 64- and 128-stage, two-phase polysilicon-aluminum-gate, p-channel registers. The 64-stage registers had 5-mil (0.13 mm) wide channels, and the 128-stage registers were made with 0.5 mil (13 μm) wide channels. The photomicrographs of the 128-stage are shown in Fig. 18. These devices were made on 0.5 to 1.0 ohm-cm, n-type silicon substrates with (100) orientation. The gate structure for both types of devices have the same width. The different channel widths were obtained by changing only the channel stop mask. As can be noted in Fig. 18, the blooming bus diffusion surrounds the entire device. These devices were fabricated following our previously described procedure for two-phase polysilicon-aluminum gate CCD's.[4] However, the p+ diffusion masks were modified so that the p+ bloom-

ing bus diffusion was placed 0.3 mil (8 μm) inside the field oxides on both sides of the CCD channel. Also the thick field oxide was replaced by an oxide with thickness $X_2 = 2000$Å under the polysilicon gates in the field regions outside of the CCD channel. In the channel region the oxides under the polysilicon and aluminum gates were grown to $X_1 = 1000$Å and $X_3 = 2400$Å, respectively.

We have also constructed 2-phase line sensors with dynamic (stepped-oxide barrier) blooming control with blooming barrier oxide $X_2 = 3000$Å, which was larger than the channel oxide under the aluminum gates ($X_3 = 2400$Å). This was done to check if there might be a reduction in transfer efficiency in devices with oxide thickness $X_2 < X_3$. The tests showed that in the case of the devices having oxide thicknesses $X_2 > X_3$, as expected, the blooming control requires special gate biasing during the optical integration period. We have also found that the transfer efficiencies in both types of devices were not affected by the presence of the anti-blooming structure and were consistent with our standard 2-phase registers.[4]

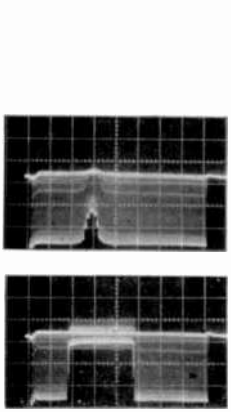

Fig. 19—Output signal of 64-stage, two-phase register with no blooming control.

A comparison of the operation of two similar 64-stage, illuminated register CCD's with and without blooming control is made in Figs. 19 and 20. The detected output of the 64-stage register with no blooming control is shown on the left Fig. 18. The top photographs shows the output signal obtained when the intensity of a light spot was adjusted to just give a saturated signal. The bottom photo shows the results of a 10 × optical overload. The carriers have spread in both directions and caused severe blooming. These results can be compared with those obtained on a similar 64-stage device with anti-blooming structure

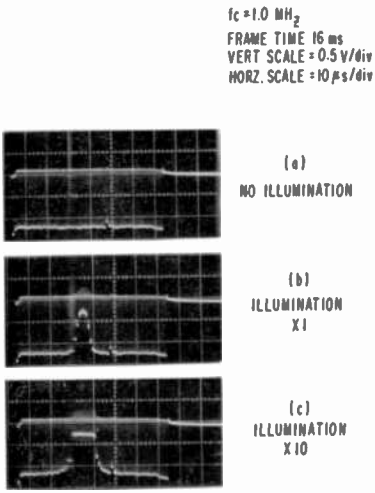

Fig. 20—Output signal of device similar to that of Figure 19, but with dynamic blooming control (stepped-oxide barrier).

shown in Fig. 20. The tests shown in these two figures were made by projecting an optical signal formed by an illuminated slit. To obtain even higher local contrast, an optical slit was painted on another 64-stage device with anti-blooming structure. Light was then projected on the device. The results of this test are shown in Fig. 21. In the top photo the light incident on the slit was adjusted to just

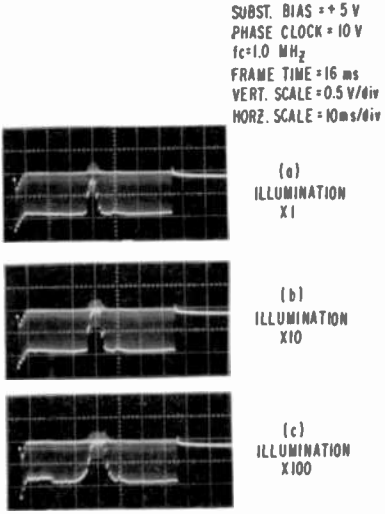

Fig. 21—Output signal of 2-phase register with dynamic blooming control (stepped-oxide barrier) illuminated through a slit painted on the register.

produce saturation. It was then adjusted to give a 10 × and 100 × overload. As can be seen in waveforms in Fig. 21, the edges of the painted slit were not completely straight and abrupt so skirts can still be seen on the envelope. Also the region on the left in Fig. 21(c) was beyond the opaque ink and was picking up scattered light. The frame time was 16 msec and readout was at 1MHz. The confinement of the spot is evident.

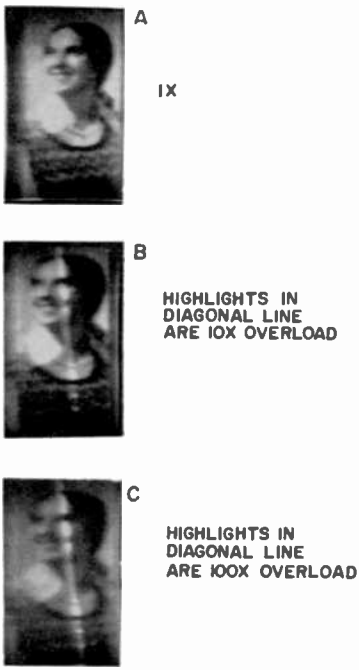

Fig. 22—Line scanned pictures using 128-stage, two-phase CCD with stepped-oxide antiblooming structure.

Line scanned pictures were made with a 128-stage 0.5-mil (13 μm) wide version of this two-phase device. These results are shown in Fig. 22. The highlights in the diagonal are at 1 ×, 10 × and 100 × saturation for this photograph. Readout was at 200 kHz and integration time was 5 msec. The containment of excess carriers is again evident.

4. Summary and Conclusions

In summary, charge-coupled image sensors are capable of low light level operation, and therefore it is desirable to have methods for controlling the large overloads that frequently occur in low level scenes and in scenes with specularly reflecting objects. Various methods of

blooming control have been investigated and the following conclusions can be made.

The accumulation mode is an operational way of limiting blooming and, although it does not completely eliminate blooming, this mode of operation can reduce it without requiring any additional structure.

The static blooming control using polysilicon blooming barrier gates is compatible with devices made with polysilicon field shield construction. The independent control of the blooming barrier in this method permits blooming control only during the optical integration time. With this type of anti-blooming construction, the charge-coupled imager with illuminated registers can be operated with some degree of electronic shutter action. A more effective electronic shutter operation can only be achieved in charge-coupled imagers designed with separate photosensor elements that are scanned by non-illuminated charge-coupled registers.

Dynamic methods of blooming control, where the barriers are established by the interaction of the clock voltages with either an ion-implanted region or a stepped-oxide region, are applicable to most charge-coupling structures. The tested devices operating with dynamic blooming control showed containment of $10\times$ and $100\times$ optical overloads. Higher overload containment is possible, but test equipment limitations prevented obtaining this information optically. However, electrical input tests indicate that overloads of 10^5 should pose no problem. The tests of line sensors with dynamic blooming control demonstrate that the presence of the dynamic blooming barriers does not reduce the transfer efficiency of these devices.

The maximum optical overload that can be tolerated by frame transfer charge-coupled imagers with illuminated registers is limited by smearing effects during the transfer of the detected image from the photosensitive area to the temporary storage area. The smearing effects increase in direct ratio to the size of the optical overload. Therefore, for maximum protection against smearing due to large optical overloads, a mechanical or electro-optic shutter should be used or the charge-coupled imager should be constructed using separate photosensor elements that incorporate some form of blooming control and are scanned by nonilluminated charge-coupled registers.

The selection of the method to be used in a particular device will be governed in large part by other system requirements and design objectives, as well as preference for device construction. In any event, the existence of these alternative approaches to blooming control serves to enhance the range of possible applications for charge-coupled imaging.

Acknowledgments

This work was partially supported by the Naval Electronic Systems Command under Contract N0039-73-C-0014. The authors would also like to thank B. F. Williams for many stimulating discussions concerning the control of blooming in charge-coupled imagers, E. C. Douglas for ion-implanting the test devices, W. S. Romito for fabrication of the two-phase devices, and V. L. Frantz for fabrication of the three-phase devices.

References:

[1] M. G. Kovac, F. V. Shallcross, W. S. Pike, P. K. Weimer, "Design, Fabrication, and Performance of a 128 x 160 Element Charge-Coupled Image Sensor," **CCD Applications Conf. Proc.**, pp. 37-42, Sponsored by Naval Electronics Laboratory Center, San Diego, Calif., Sept. 18-20, 1973.

[2] W. F. Kosonocky and J. E. Carnes, "Design and Performance of Two-Phase Charge-Coupled Devices with Overlapping Polysilicon and Aluminum Gates," **Technical Digest**, 1973 International Electron Devices Meeting, pp. 123-125, Dec. 3-5, 1973, Washington, D.C.

[3] R. H. Krambeck, R. H. Walden, and K. A. Pickar, "A Doped Surface Two-Phase CCD," **Bell Syst. Tech. J.**, Vol. 51, No. 8, p. 1849, Oct. 1972.

[4] W. F. Kosonocky and J. E. Carnes, "Two-Phase Charge-Coupled Devices with Overlapping Polysilicon and Aluminum Gates," **RCA Review**, Vol. 34, p. 164, March 1973.

Intermodulation Distortion in Resistive Mixers

Stewart M. Perlow
RCA Laboratories, Princeton, N. J. 08540

Abstract—This paper discusses the relationship between the nonlinear gain characteristic of a resistive mixer and intermodulation distortion. The analysis is divided into two distinct parts. First, a generalized equivalent circuit that is valid for large signals or small signals is derived. The purpose of the development used is to show in progressive steps the effects of the higher-order terms of the diode expansion. Once the generalized equivalent circuit is obtained, impedance-matching criteria are developed for optimum power-matching conditions. The second part of the analysis is a study of the series representation of the nonlinear gain equation obtained from the generalized equivalent circuit. The final result is an equation that predicts the amplitude of the intermodulation distortion at any of the intermodulation frequencies.

Introduction

Knowledge of the intermodulation distortion of an amplifier or converter is important because it is a measure of the fidelity of the device. The fidelity of an amplifier or frequency converter is described by the linearity of its gain characteristic. The gain is essentially constant over a certain range of input levels, but deviates greatly from linearity once a particular level is exceeded. This deviation from linearity is known as gain saturation, and operation in this region is characterized by a severely distorted reproduction of the input. Gain saturation and

noise figure are the upper and lower limits of dynamic range. In many applications, especially where high-level signals are to be processed, gain saturation is a much more important specification than noise figure.

If two or more signals are applied to the input of an amplifier or converter and are of sufficient level to cause gain saturation, the nonlinear gain characteristic produces nonlinear distortion that consists of mixing of the input signals. The resulting output contains, in addition to the original signals, responses at every sum and difference frequency. In the case of two signals of frequencies f_1 and f_2 applied to an amplifier, the output contains every frequency corresponding to $(m+1)\ f_1 \pm mf_2$ and $(m+1)\ f_2 \pm mf_1$, where m is any positive integer. That is, the output spectrum consists of equally spaced frequency responses, where the spacing is the difference between the two original frequencies. The output of a frequency converter would consist of the same spectrum, except that the center is shifted by the frequency of the local oscillator or pump source. The amplitude of the output at these intermodulation frequencies is determined by the degree of gain saturation. Therefore, the amount of intermodulation distortion, as determined by a two-tone test, is a very convenient criterion for specifying the upper limit of dynamic range or the linearity of an amplifier or converter.

The purpose of this analysis is to obtain a complete equivalent circuit for a resistive mixer diode in terms of diode parameter I_{sat} and the voltage levels present at the diode terminals. The complete equivalent circuit arrived at is easily adaptable for small- or large-signal analysis and is also reducible to an equivalent circuit for a square-law diode.

The analysis is carried out on a large-signal basis by assuming that three sinusoidal voltages (the signal, the local oscillator, and the intermediate frequency) are across the diode terminals. The exponential equation for the diode current is then expanded in a power series. The equivalent circuit is obtained using only the first two terms of the series. This is the case for a true square-law diode. Using this equivalent circuit for the diode in a mixer circuit, the gain equation is derived and is shown to exhibit saturation even though the diode is square law.

The effect of the other terms in the expansion, usually known as the diode nonlinearities, on the equivalent circuit and on predicted gain are then investigated. The final equivalent circuit obtained is perfectly general for any diode exponent and for any voltage level at the diode terminals. It leads to specific values needed for signal, load,

and local-oscillator resistances for optimum matching; and it also predicts the changes in resistance levels as the voltage levels are changed.

Using the equivalent circuit, the gain equation of the resistive-mixer diode is obtained, and an intermodulation analysis is performed. This analysis is based on the use of the envelope gain characteristics of the complete device for a single input signal, rather than the diode *I-V* characteristic. Intermodulation distortion is then predicted on the basis of applying more than one signal to the device, where the separation between the signal frequencies is much smaller than either signal frequency. Intermodulation distortion for any particular operating power level is then predicted.

Power Series Representation

The diode current is related to the voltages at the diode terminals by

$$i = I_{sat}(e^{\alpha v} - 1), \qquad [1]$$

where I_{sat} is the reverse saturation current. Expanding this equation in a series results in

$$i = I_{sat} \sum_{n=1}^{\infty} \frac{(\alpha v)^n}{n!} \qquad [2]$$

The desired voltages across the diode terminals are those due to the signal, local oscillator, and intermediate frequency output. The expression for the diode terminal voltage, is therefore,

$$v = V_s \cos(\omega_s t + \theta_s) + V_p \cos(\omega_p t + \theta_p) + V_o \cos(\omega_o t + \theta_o) \qquad [3]$$

where the subscript s indicates the signal frequency, p the pump or local oscillator frequency, and o the output intermediate frequency.

The sinusoids may be expressed in exponential form:

$$v = (v_s e^{j\omega_s t} + v_s^* e^{-j\omega_s t}) + (v_p e^{j\omega_p t} + v_p^* e^{-j\omega_p t}) + (v_o e^{j\omega_o t} + v_o^* e^{-j\omega_o t}) \qquad [4]$$

where

$$v_s = \frac{V_s}{2} e^{j\theta_s}$$

$$v_s^* = \frac{V_s}{2} e^{-j\theta_s}$$

Each term of the expansion contains a power relation of the diode terminal voltage. In general, when v is raised to a power, the result is a sum of sinusoids of several frequencies. Since the only frequencies of interest are those specified in Eq. [3], it is assumed that the appropriate filters will be added to the circuit to eliminate all the undesired frequencies. The actual calculations, although algebraically simple, are quite tedious and will not be listed here. The resulting expressions for v raised to a power are shown in Table 1, where only the three frequencies of interest remain. The relationship between these three frequencies is:

$$\omega_o = \omega_p + \omega_s.$$

Table 1—Expressions for Diode Terminal Voltage v Raised to a Power for ω_s, ω_p, and ω_o

Term	Amplitude	Phase
Signal Frequency ω_s		
v	V_s	θ_s
v^2	$V_o V_p$	$\theta_o - \theta_p$
v^3	$\frac{3}{4} V_s(V_s^2 + 2V_o^2 + 2V_p^2)$	θ_s
v^4	$\frac{3}{2} V_o V_p(V_o^2 + V_p^2 + 2V_s^2)$	$\theta_o - \theta_p$
Pump Frequency ω_p		
v	V_p	θ_p
v^2	$V_s V_o$	$\theta_o - \theta_s$
v^3	$\frac{3}{4} V_p(V_p^2 + 2V_s^2 + 2V_o^2)$	θ_p
v^4	$\frac{3}{4} V_s V_o(V_s^2 + V_o^2 + 2V_p^2)$	$\theta_o - \theta_s$
Output Intermediate Frequency ω_o		
v	V_o	θ_o
v^2	$V_p V_s$	$\theta_s - \theta_p$
v^3	$\frac{3}{4} V_o(V_o^2 + 2V_p^2 + 2V_o^2)$	θ_o
v^4	$\frac{3}{4} V_p V_s(V_s^2 + V_p^2 + 2V_o^2)$	$\theta_s - \theta_p$

It is interesting to note that in order to have information translated from the signal to output frequencies, the only term required is the squared term. This, of course, is the simplest form of mixer—the square-law mixer. Considering an idealized square-law diode of this type, Eq. 2 becomes

$$i = I_{sat}\left[\alpha V + \frac{(\alpha V)^2}{Z!}\right]. \qquad [5]$$

The meaning of the term "square-law diode" should be clarified. In common useage, when one refers to a square-law diode, it means that the voltages across the diode terminals are small enough to render negligible the third- and higher-order terms in the expansion. However, if the voltage is increased to high signal levels, these terms must be considered, and the nature of the response is completely changed. The square-law diode in this discussion refers to a diode characteristic whose expansion ends with the squared term for any terminal voltage, be it large or small. The reason for this clarification is that if one is talking about a diode that is square law for small voltages only, it is expected that when a large signal is used saturation and intermodulation distortion will occur. It will be shown that a mixer using a true square-law diode saturates as well and some degree of intermodulation is always present. The following analysis holds for the true idealized square-law diode.

Substituting Eq. [4] into Eq. [5] and collecting similar frequency terms results in the diode currents

$$\begin{aligned} i_o &= \alpha I_{sat}(v_o + \alpha v_s v_p) \\ i_p &= \alpha I_{sat}(v_p + \alpha v_o v_s^*) \\ i_s &= \alpha I_{sat}(v_s + \alpha v_o v_p^*), \end{aligned} \qquad [6]$$

where the total diode current is

$$i = i_o e^{j\omega_o t} + i_o^* e^{-j\omega_o t} + i_p e^{j\omega_p t} + i_p^* e^{-j\omega_p t} + i_s e^{j\omega_s t} + i_s^* e^{-j\omega_s t}. \qquad [7]$$

Equivalent Circuit and Gain Equation for Square-Law Diode

Using Eq. [7] and the mixer circuit shown in Fig. 1 results in the following circuit equations:

$$G_{To} v_o = \alpha^2 I_{sat} v_s v_p, \qquad [8]$$

$$i_{gp} = G_{Tp} v_p + \alpha^2 I_{sat} v_o v_s^*, \quad [9]$$

$$i_{gs} = G_{Ts} v_s + \alpha^2 I_{sat} v_o v_p^*, \quad [10]$$

where i_{gp} and i_{gs} represent the local-oscillator and signal current sources, i.e.,

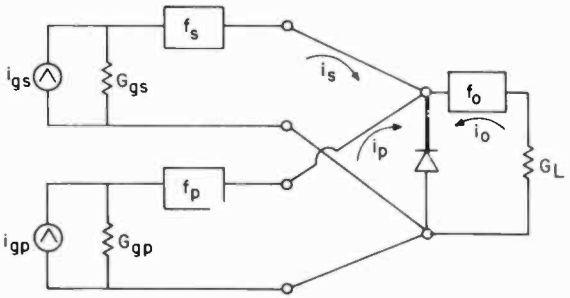

Fig. 1—Mixer circuit.

$$\text{Re}\,(i_{gp} e^{j\omega pt}) = \text{Re}\left(\frac{I_{sp}}{2} e^{j(\omega pt + \theta_{sp})}\right)$$

$$= I_{gp} \cos\,(\omega_p t + \theta_{sp}) \quad [11]$$

and the conductances G are

$$G_{To} = \alpha I_{sat} + G_L \quad [12a]$$

$$G_{Tp} = \alpha I_{sat} + G_{gp} \quad [12b]$$

$$G_{Ts} = \alpha I_{sat} + G_{gs} \quad [12c]$$

It is noted that the units of α are $(\text{volts})^{-1}$, and the units of I_{sat} are amperes, thus making αI_{sat} an equivalent conductance.

With Eqs. [8], [9], and [10], it is very easy to develop an equivalent circuit for the square-law diode that holds for both small and large signals. This circuit is shown in Fig. 2. The voltage gain of the circuit is the transfer function v_o/v_s. Using Eq. [8] and solving for the gain

$$\frac{v_o}{v_s} = \frac{\alpha^2 I_{sat}}{G_{To}} v_p. \quad [13]$$

Eq. [8] and [9] are now solved simultaneously to obtain v_p as a function of the pump source and signal. Substituting into Eq. [13] results in

$$\frac{v_o}{v_s} = \frac{\alpha^2 I_{sat}}{G_{To}G_{Tp}} \frac{i_{gp}}{[1 + \alpha^4 I_{sat} v_s^2/(G_{To}G_{Tp})]} \qquad [14]$$

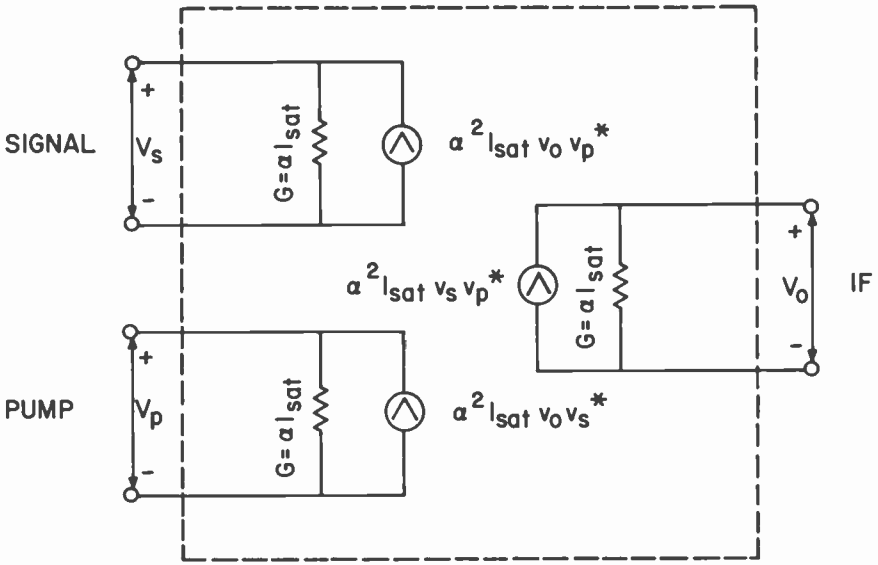

Fig. 2—Equivalent circuit of a square-law diode.

or

$$\frac{v_o}{v_s} = \frac{A_o}{1 + (A_1 v_s)^2} \qquad [15]$$

where

$$A_o = \frac{\alpha^2 I_{sat}}{G_{To}G_{Tp}} i_{gp}$$

$$A_1^2 = \frac{\alpha^4 I_{sat}^2}{G_{To}G_{Tp}}.$$

The gain has thus been shown to be a function of the signal level. It is this factor that produces saturation; as the signal level is increased, the gain begins to drop off. The saturation level, i.e., the point at which the maximum output occurs, is reached when the product $(A_1 v_s)^2$ is unity. The gain is never truly a constant; for small values of signal voltage, however, the $(A_1 v_s)^2$ term may be considered negligible compared to unity, and the gain can be considered a constant. The value the gain assumes for small signals is, therefore, A_o, the small signal gain.

These results are important because the idealized square-law diode mixer does indeed saturate if the local oscillator level is held constant.

The physical reason for this saturation is interesting. It occurs because, as the signal power is increased, the signal voltage rises causing mismatches in both pump and output circuit, which in turn produces a mismatch in the signal circuit. This mismatch reflects the incident signal power.

This can be seen by solving Eqs. [8] and [9] simultaneously for the pump-circuit input conductance:

$$G_{inp} = \frac{i_{gp}}{v_p} = G_{Tp} + \frac{\alpha^4 I_{sat}^2}{G_{To}} |v_s|^2 \qquad [16]$$

As the signal voltage increases, the pump circuit conductance is changed, thus reflecting the incident pump power. Similarly, the signal-circuit input conductance depends on the pump voltage developed across the diode:

$$G_{ins} = G_{Ts} + \frac{\alpha^4 I_{sat}^2}{G_{To}} |v_p|^2 \qquad [17]$$

Since the pump circuit conductance has changed, v_p will change, thus changing the signal-circuit input conductance. Even in this idealized case of a square-law mixer, these interactions are extremely complex, because all the terminal voltages interact with one another due to the dependence of input conductances on terminal voltage.

Effect of Third-Order Term on Equivalent Circuit

For diodes other than the true square-law type, other terms in the series expansion must be taken into account. The effect of these terms

(known as device nonlinearities) on the gain equation and, subsequently, the saturation level will now be investigated.

Adding the third term of the expansion to the current in Eq. [5] results in an additional term at each of the three frequencies that have the same phase as the original voltages. Since the phase-angle contributions are the same, the amplitude coefficients for just the output current can be combined as follows:

$$i_{\text{output}} = \alpha I_{\text{sat}} V_o \left[1 + \frac{\alpha^2}{8} (V_o^2 + 2V_s + 2V_p^2) \right] \cos(\omega_o t \theta_o) + \frac{\alpha^2}{2} I_{\text{sat}} V_s V_p \cos(\omega_o t + \theta_s + \theta_p). \quad [18]$$

Therefore, the nonlinearities due to the third term produce an additional current at each frequency whose magnitude depends upon all the voltages across the diode terminals.

The diode currents may now be written as

$$i_o = \alpha I_{\text{sat}}[v_o(1 + K_o) + \alpha v_s v_p], \quad [19a]$$

$$i_p = \alpha I_{\text{sat}}[v_p(1 + K_p) + \alpha v_o v_s^*], \quad [19b]$$

$$i_s = \alpha I_{\text{sat}}[v_s(1 + K_s) + \alpha v_o v_p^*], \quad [19c]$$

where

$$K_o = \frac{\alpha^2}{8} (v_o^2 + 2V_s^2 + 2V_p^2),$$

$$K_p = \frac{\alpha^2}{8} (V_p^2 + 2V_s^2 + 2V_o^2),$$

$$K_s = \frac{\alpha^2}{8} (V_s^2 + 2V_p^2 + 2V_o^2).$$

These currents are the same as those for the square-law case, except that the first term is multiplied by $(1 + K)$.

Using these currents and going through the same procedure used for the square-law diode, the voltage gain as a function of the pump voltage is the same (Eq. [13]), except that the total conductance in the output circuit, G_{T_o} now becomes

$$G_{To} = \alpha I_{sat}(1 + K_o) + G_L. \qquad [20a]$$

That is, the fixed conductance the diode presents, αI_{sat}, is multiplied by $(1 + K)$. The fixed portion of the diode conductance has now become a function of the voltage levels (magnitudes) at the diode terminals, which was not so for the square-law case.

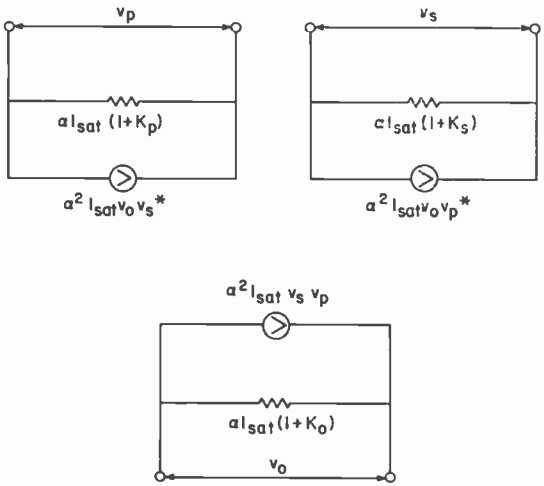

Fig. 3—Equivalent circuit of a diode using three terms in series expansion.

Similarly, the fixed conductances presented by the diode in the local oscillator and signal circuits become

$$G_{Tp} = \alpha I_{sat}(1 + K_p) + G_{gp}, \qquad [20b]$$

$$G_{Ts} = \alpha I_{sat}(1 + K_s) + G_{gs}. \qquad [20c]$$

The gain equation is in exactly the same form as for the square-law case, but with the new values of G_{To} and G_{Tp} replacing the original values. Note that the small-signal gain A_o and the saturation level coefficient $A_1{}^2$ are no longer fixed quantities but are now dependent on the diode terminal voltages. This is one of the principal differences between the square-law diode and non-square-law diode. A more detailed examination of this difference and the effect of pump power level on gain and intermodulation distortion will be made later.

The new equivalent circuit is shown in Fig. 3.

Effect of Fourth-Order Term on Equivalent Circuit

The effect of the fourth term of the expansion on the gain equation is found by adding it to the current and deriving the gain equation in the same manner as used previously. The resulting diode currents are

$$i_o = \alpha I_{sat}[v_o(1 + K_o) + \alpha v_s v_p(1 + L_o)], \quad [21a]$$

$$i_p = \alpha I_{sat}[v_p(1 + K_p) + \alpha v_o v_s^*(1 + L_p)], \quad [21b]$$

$$i_s = \alpha I_{sat}[v_s(1 + K_s) + \alpha v_o v_p^*(1 + L_s)], \quad [21c]$$

where

$$L_o = \frac{\alpha^2}{8}(V_s^2 + V_p^2 + 2V_o^2),$$

$$L_p = \frac{\alpha^2}{8}(V_s^2 + V_o^2 + 2V_p^2),$$

$$L_s = \frac{\alpha^2}{8}(V_o^2 + V_p^2 + 2V_s^2).$$

The effect of adding the fourth term is to change the equivalent-circuit current sources. The new equivalent circuit is shown in Fig. 4.

In general, the odd-order power terms change the equivalent-circuit diode conductances, while the even-order power terms change the equivalent-circuit current generators. It should be pointed out that the terms of the expansion also add dc currents to the sinusoidal currents. These dc currents are functions of the voltage levels at the diode terminals. Because of this, the dc bias will change with changes in signal and local oscillator input level.

The voltage gain expression for this case is of exactly the same form as the two previous cases. However, A_o and A_1 have again changed.

Complete Equivalent Circuit

Now that the effect of both the third- and fourth-order terms have been seen, generalizations as to the effect of all higher-order terms can be made. The voltage-gain expression always remains in the form of

Eq. [15]. However, G_{Ts}, G_{To}, and G_{Tp} become diode-terminal-voltage sensitive. They can be written in the form

$$G_{To} = \alpha I_{sat}(1 + K_o') + G_L, \qquad [22a]$$

$$G_{Tp} = \alpha I_{sat}(1 + K_p') + G_{gp}, \qquad [22b]$$

$$G_{Tp} = \alpha I_{sat}(1 + K_s') + G_{gs}, \qquad [22c]$$

where K_p', K_o', are functions of the voltage levels (magnitudes) at the diode terminals. Note that they do not vary sinusoidally. Their values are determined from contributions of all the odd-order terms of the expansion.

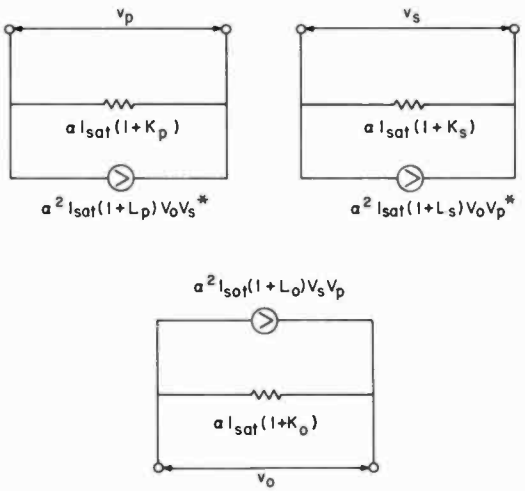

Fig. 4—Equivalent circuit of a diode using four terms in series expansion.

The effect of all the even-order terms is to multiply the equivalent-circuit current sources by $(1 + L_o')$, $(1 + L_p')$ for the output, local oscillator, and signal circuits, respectively. The values of L_o', L_p', and L_s' are also functions of the voltage levels at the diode terminals.

The diode currents may be expressed in the form of Eq. [7] by using the closed-form solution for the sum of all the even-order term contributions and the sum of all the odd-order term contributions.

$$i_s = \alpha I_{sat}[V_s(1 + K_s') + \alpha V_o V_p^*(1 + L_s')], \qquad [23a]$$

$$i_p = \alpha I_{sat}[V_p(1 + K_p') + \alpha V_o V_p^*(1 + L_p')], \quad [23b]$$

$$i_o = \alpha I_{sat}[V_o(1 + K_o') + \alpha V_s V_p(1 + L_o')], \quad [23c]$$

where

$$1 + K_s' = 2\frac{I_1(\alpha V_s)}{\alpha V_s} I_o(\alpha V_p) I_o(\alpha V_o),$$

$$1 + K_p' = 2\frac{I_1(\alpha V_p)}{\alpha V_p} I_o(\alpha V_s) I_o(\alpha V_o),$$

$$1 + K_o' = 2\frac{I_1(\alpha V_o)}{\alpha V_o} I_o(\alpha V_p) I_o(\alpha V_s),$$

$$1 + L_s' = 2I_o(\alpha V_s)\frac{I_1(\alpha V_p)}{\alpha V_p}\frac{I_1(\alpha V_o)}{\alpha V_o},$$

$$1 + L_p' = 2I_o(\alpha V_p)\frac{I_1(\alpha V_s)}{\alpha V_s}\frac{I_1(\alpha V_o)}{\alpha V_o},$$

$$1 + L_o' = 2I_o(\alpha V_o)\frac{I_1(\alpha V_p)}{\alpha V_p}\frac{I_1(\alpha V_s)}{\alpha V_s}.$$

$I_o(\alpha V)$ and $I_1(\alpha V)$ are modified Bessel functions of the first kind. Their values may be easily determined from Bessel function tables for any specified value of (αV).

Note that for small voltages (i.e., V_s, V_p, and V_o all approaching zero), the higher-order terms of the original expansion, Eq. [2], are negligible, and mixer operation is square-law. It is therefore expected that these currents would be reduced to the square-law currents, Eq. [7]. This is true, since, as the voltages approach zero,

$$\lim_{V \to 0} I_1 \frac{(\alpha V)}{\alpha V} = \frac{1}{2}, \quad [24]$$

$$\lim_{V \to 0} I_o(\alpha V) = 1. \quad [25]$$

and Eqs. [23] reduce to the square-law currents of Eq. [7].

Eqs. [23] describes the complete equivalent circuit for the diode. It is shown in Fig. 5.

Impedance-Matching Criteria

For optimum power-matching conditions, the source and load impedance should be matched to the input impedance of the appropriate circuit. Since these input impedances depend on the magnitudes of the voltages at each port, the circuits must be rematched for any change in voltage

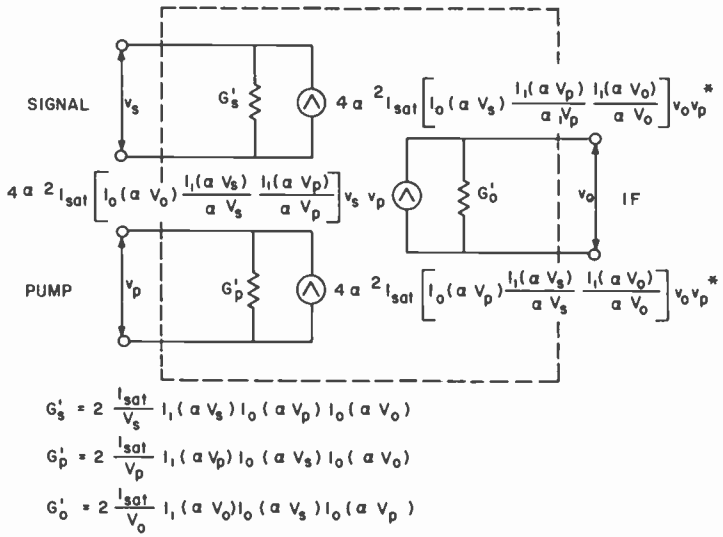

Fig. 5—Complete equivalent circuit of diode.

levels if optimum matching is to be achieved. Using the equivalent circuit, the required source and load conductances are found to be

$$G_{gs} = G_s' \sqrt{1 - \left[\frac{I_1(\alpha V_p)}{I_0(\alpha V_p)}\right]^2}, \qquad [26a]$$

$$G_L = G_o' \sqrt{1 - \left[\frac{I_1(\alpha V_p)}{I_0(\alpha V_p)}\right]^2}, \qquad [26b]$$

where

$$G_s' = 2\frac{I_{sat}}{V_s} I_1(\alpha V_s) I_0(\alpha V_p) I_0(\alpha V_o), \qquad [27a]$$

$$G_o' = 2\frac{I_{sat}}{V_o} I_1(\alpha V_o) I_o(\alpha V_s) I_o(\alpha V_p). \qquad [27b]$$

For small voltage levels, these conductances approach the values for the square-law diode, that is,

$$G_L = G_{gs} = G_{gp} = \alpha I_{sat}. \qquad [28]$$

The optimum matching conditions for the square-law diode thus require equal conductances for the two sources and the load. For a typical diode with an α of 20 and I_{sat} of 10×10^{-6}, the source and load impedances are 5000 ohms.

For a real mixer this case is quite unlikely, since the conversion efficiency is related to the pump power, which is usually made large to keep the efficiency as large as possible. $I_o(\alpha V_p)$ is therefore not equal to unity and must appear in the equation. This case, in which αV_s and αV_o are considered much smaller then αV_p, is the real small-signal case. It is the one used for small-signal analysis of the resistive mixer.

For these conditions, V_s and V_o approach zero; and the required source and load conductances G_{gs} and G_L become

$$g_{gs} = \alpha I_{sat} \sqrt{I_o^2(\alpha V_p) - I_1^2(\alpha V_p)}, \qquad [29a]$$

$$g_L = \alpha I_{sat} \sqrt{I_o^2(\alpha V_p) - I_1^2(\alpha V_p)}, \qquad [29b]$$

where a small letter g is used to indicate values associated with the small-signal case.

It is interesting to see that the required source and load impedances are equal and are functions of the diode parameters and the pump or local-oscillator voltage only. If the local-oscillator source is fixed, they are constants. The values for G_{gs} and G_L are in exact agreement with the values found from Pantell's small-signal equivalent circuit for a nonlinear resistance.[1] This analysis, however, is further generalized since Eqs. [26] and [27] will give the impedance levels for large-signal voltages as well as for small.

To get an idea of the source and load resistances required for the small-signal matching conditions, αV_p must first be calculated. The matching network for the pump circuit varies with mixer configura-

tion. For single-diode mixers the pump may be either loosely or tightly coupled to the diode, depending upon the requirements for isolating the pump circuit from the antenna. For this example let it be assumed that the diode pump impedance is about 100 ohms. The pump voltage with 1 mw of pump power is therefore

$$v_p = \frac{P_p R_p}{2} = 0.316 \text{ volts.}$$

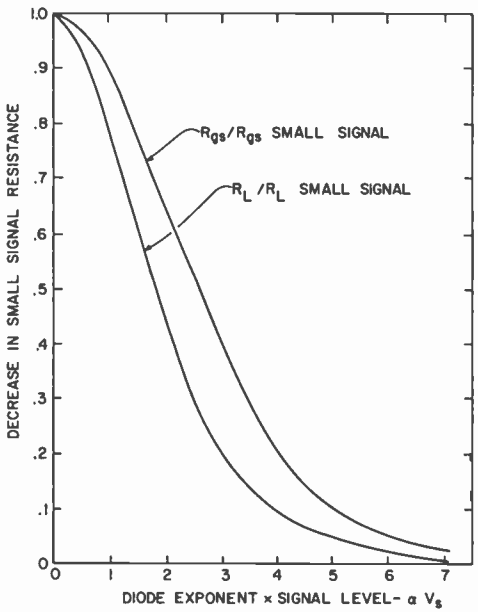

Fig. 6—Variation in input and output impedance as a function of signal voltage amplitude.

Therefore,

$$\alpha V_p = 6.32,$$
$$I_o(\alpha V_p) = 88,$$
$$I_1(\alpha V_p) = 81.$$

The small-signal input and output impedance is therefore

$$r_{ys} = r_L = \frac{1}{\alpha I_{sat}\sqrt{I_o^2(\alpha V_p) - I_1^2(\alpha V_p)}} = 146 \text{ ohms.}$$

If the signal level is appreciable, then its effect on the small-signal conductances must also be considered:

$$G_{gs} = g_{gs} 2 \frac{I_1(\alpha V_s)}{\alpha V_s} I_o(\alpha V_o),$$

$$G_L = g_L 2 \frac{I_1(\alpha V_o)}{\alpha V_o} I_o(\alpha V_s).$$

Fig. 6 shows the variation in input and output impedance as a function of signal-voltage amplitude. For this figure, a conversion loss of 10 dB was assumed. This is a typical value. Note that the load resistance decreases more rapidly than the input resistance. This is due to the fact that the modified Bessel functions vary much more rapidly at large argument values, and V_o was considered to be approximately one-third of V_s. If no conversion loss were present, both curves would be the same as the R_{gs}/r_{gs} curve.

Gain Equation and Intermodulation Distortion

To evaluate the intermodulation distortion properties of the resistive diode, it is best to look first at the specific case of the square-law diode. For square-law operation, all terminal voltages are assumed to be small and the gain equation is

$$v_o = \frac{A_o v_s}{1 + (A_1 V_s)^2}. \qquad [15]$$

Eq. [15] may be put in a power series expansion for $|A_1 v_s| < 1$. Therefore,

$$v_o = A_o v_s \sum_{n=0}^{\infty} (-1)^{n+2} (A_1 v_s)^{2n}. \qquad [30]$$

If an equal-amplitude two-tone test is used to measure intermodulation distortion, two signals of frequencies f_a and f_b are applied to the input. The output contains responses at every sum and difference frequency due to the distortion of the device. The frequencies of interest for intermodulation distortion specifications are those that are

closest to the two original frequencies. These correspond to $(m+1)f_a - mf_b$ and $(m+1)f_b - mf_a$.

For analysis purposes, it is more convenient to assume a double-sideband suppressed-carrier signal (DSBSC)applied to the input. This signal is of the form

$$\begin{aligned} V_{\text{signal}} &= (V_s \cos \epsilon t) \cos \omega_s t \\ &= \frac{1}{2} V_s \cos (\omega_s + \epsilon) t + \frac{V_s}{2} \cos (\omega_s - \epsilon) t, \end{aligned} \qquad [31]$$

where

$$\epsilon \ll \omega_s.$$

This is equivalent to two signals at the input with

$$\omega_a = \omega_s + \epsilon,$$

$$\omega_b = \omega_s - \epsilon.$$

The intermodulation frequencies corresponding to $(m+1)f_a - mf_b$ and $(m+1)f_b - mf_a$ now become $f_s \pm (2m+1)E$. This technique greatly simplifies the analysis, since multiple-tone input signals are not needed in the derivation of the gain equation.

With the DSBSC signal applied to the input, Eq. [30] may be written

$$\hat{v}_o = A_o |V_s| [\hat{v}_s - (A_1 V_s)^2 \hat{v}_s^3 + (A_1 V_s)^4 \hat{v}_s^5 - \cdots] \qquad [32]$$

where $\hat{v}_s = \cos \epsilon t$.

Eq. [32] is put in series form for easy identification of the intermodulation distortion terms. That is, when V signal is of the form $\cos (\omega_s + \epsilon) t + \cos (\omega_s - \epsilon) t$, the second term in the expansion, along with the first term, gives rise to the desired output. In addition, the second term contributes to the first intermodulation distortion product of the form $K \cos (\omega_s \pm 3\epsilon) t$, or, if ω_a and ω_b are used, $K \cos (2\omega_a - \omega_b) t$ and $K \cos (2\omega_b - \omega_a) t$.

Each intermodulation distortion product are usually referred to by the order of the particular term in the series expansion in which it appears. For example, the intermodulation due to the second term of

the expansion would be called the third-order intermodulation distortion because that term is of the third order. However, since many terms of the expansion will be considered, and since more than one term will contribute to intermodulation distortion when (A_1V_s) is large, the intermodulation distortion products will be referred to by the number corresponding to m in the foregoing notation. Therefore, the first intermodulation product is obtained when $m = 1$.

The intermodulation distortion products will be produced in each of the higher-order terms of the expansion. Their amplitudes will be the product of $(A_1V_s)^{2m}$, and the coefficient of the intermodulation frequency will be obtained from $\cos(2n+1)\epsilon t$. The total intermodulation distortion amplitude will be the sum of all these contributions.

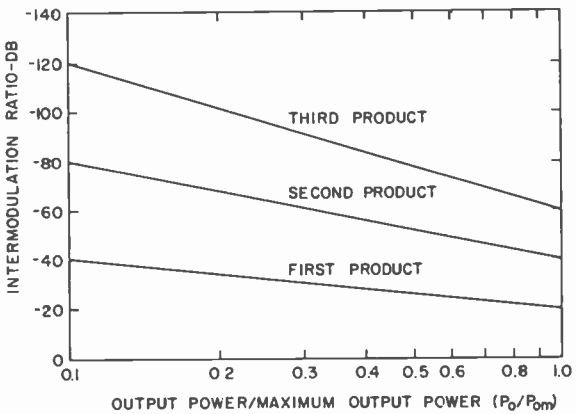

Fig. 7—Intermodulation distortion ratios.

It is more convenient to express the coefficients of the expansion, $(A_1V_s)^{2m}$, as functions of the output power level. This has already been done in an analysis for the square-law parametric up-converter:[2]

$$[A_1V_s]^2 = \frac{(P_o/2)/P_{om}}{[1-(P_o/2)]/[P_{om} \pm \sqrt{(1-P_o)/P_{om}}]} \qquad [33]$$

where $P_{om} = 2G_L(A_o/2A_1)^2$ is the maximum output power of the mixer, i.e., the output power when the mixer becomes saturated.

The coefficients of the expansion, Equation [32], may now be found for any specified value of P_o/P_{om}. This analysis has already been performed, and the results are shown in Fig. 7. It should be noted here that the intermodulation distortion products are exactly the same as those obtained in a square-law parametric upconverter.[2]

Examination of Eq. [32] shows that the intermodulation distortion ratio, which is the ratio of the intermodulation distortion product to the desired output, is a function of the magnitudes of coefficient of each term in the expansion, while the term multiplying the whole series, $A_o v_o$, determines the output level.

The definition of P_{om} given is mathematical with respect to its derivation. It is interesting to get a physical concept of this very important quantity. As defined, P_{om} is

$$P_{om} = 2G_L \left(\frac{A_o}{2A_1} \right)^2 . \qquad [34]$$

Substituting the values from Eqs. [12] and [15] into Eq. [34] results in

$$P_{om} = \frac{1}{4} \left(\frac{i_{gp}}{2} \right)^2 \frac{1}{G_{gp}} . \qquad [35]$$

This result shows that P_{om} is proportional to the pump power, i.e.,

$$P_{om} = \frac{1}{4} P_p . \qquad [36]$$

The plots shown in Fig. 7 may be written in analytic form as

$$\mathrm{IMR_m(dB)} = m \left[2 \frac{P_o}{P_{om}} \mathrm{(dB)} - 19.5 \right] . \qquad [37]$$

Therefore, the first intermodulation distortion product ratio is

$$\mathrm{IMR_1(dB)} = 2 \frac{P_o}{P_{om}} - 19.5. \qquad [38]$$

Since P_{om} is proportional to P_p, Eq. [36], it is easily seen that an increase in pump power will decrease the intermodulation distortion. If the pump power is increased by 1 dB, the intermodulation distortion ratio is decreased by 2 dB. The intermodulation distortion in a resistive mixer can, therefore, be reduced by increasing the pump power; for every 1-dB increase in pump power, the intermodulation distortion ratio is decreased by two decibels.

It is sometimes more convenient to express the intermodulation distortion ratio in terms of the input power rather than the output power. In this form, the maximum signal power for a specified amount of intermodulation distortion is easily determined. For output powers up to 60% of P_{om}, the ratio of output power to input power is approximately equal to the small-signal power gain A_o^2. The maximum error is about 2 dB when $P_o/P_{om} = 0.6$. The conversion efficiency of most resistive mixers is approximately −6 dB, or

$$\frac{P_o}{P_s} = \frac{1}{4} \text{ if } \frac{P_o}{P_{om}} \leq 0.6. \quad [39]$$

Under the conditions of Eq. [39] and using Eq. [36],

$$\frac{P_o}{P_{om}} = \frac{P_s}{P_p} \text{ if } \frac{P_o}{P_{om}} \leq 0.6. \quad [40]$$

Therefore, for all practical purposes, P_o/P_{om} may be replaced by P_s/P_p. Eq. [38] may now be rewritten

$$\text{IMR}_1\,(\text{dB}) = 2\frac{P_s}{P_p}\,(\text{dB}) - 19.5. \quad [41]$$

Experimental Results

Intermodulation distortion tests were made on several types of mixers. The test results for a balanced mixer are shown in Fig. 8.

Fig. 9 contains experimental test values along with a plot of Eq. [41] for two different types of mixers. Four different values of pump power were used for each mixer. The measured values agree excellently with the theoretical values. The maximum deviation in intermodulation distortion ratio is only 4 dB.

Conclusions

Gain saturation and intermodulation distortion occur even when an ideal square-law diode is used in a mixer circuit. This is due to the dependence of the current flowing in the input circiut of the diode on the output or intermediate-frequency voltage, Eq. [7]. It is for this reason that, if the output voltage is left out of the analysis, a square-

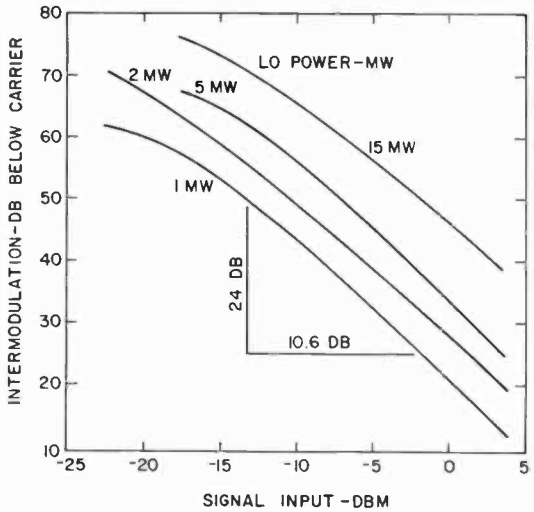

Fig. 8—Intermodulation distortion ratio in balanced mixer.

law diode mixer will not exhibit gain saturation or intermodulation distortion.

The analysis presented herein produces a complete equivalent circuit of a diode mixer. The equivalent circuit is completely general

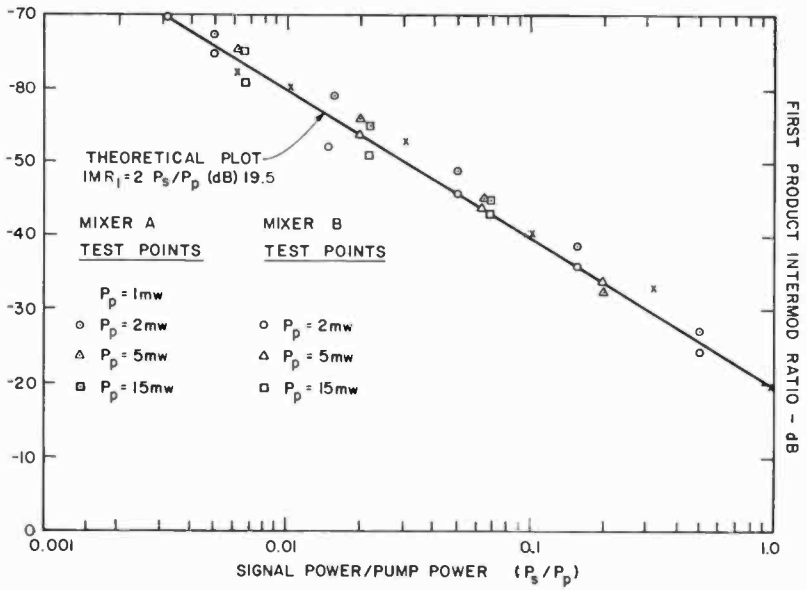

Fig. 9—Experimental test values for two different mixers compared to theoretical values (Eq. [41]).

and can be reduced to the equivalent circuit of an ideal square-law diode or to a small- or large-signal equivalent circuit. Using this circuit to derive the gain equation of the mixer results in the prediction of intermodulation distortion ratios as a function of the output power/maximum-output power or signal power/pump power. The equation expressing this relationship is

$$\mathrm{IMR}_1(\mathrm{dB}) = 2\frac{P_o}{P_{om}}(\mathrm{dB}) - 19.5 \approx 2\frac{P_s}{P_p}(\mathrm{dB}) - 19.5. \qquad [42]$$

This is exactly the same equation that has been derived for the parametric upper sideband upconverter.[2]

The intermodulation analysis was carried out by using the envelope gain characteristic of the complete mixer for a single input signal rather than the diode *I-V* characteristic. A double-sideband suppressed-carrier signal was used on the input, which is equivalent to a two-tone test with the difference between the two signal frequencies much smaller than the signal frequencies themselves. This technique greatly simplifies the analysis since multiple-tone input signals are not needed in the derivation of the gain equation.

Since the analysis was performed assuming a wideband frequency-response characteristic, any inherent reduction of bandwidth at the output of the mixer may be taken into account by simply subtracting from Eq. [42] the attenuation (in dB) at the intermodulation frequencies due to the bandpass characteristic.

Eq. [42] also shows that increasing the pump power will decrease the intermodulation distortion. A 1-dB increase in pump power decreases the intermodulation distortion ratio by 2 dB.

Bibliography:

[1] R. H. Pantell, "General Power Relationships for Positive and Negative Nonlinear Resistive Elements," **Proc. IRE,** Vol. 46, p. 1910, Dec. 1958.

[2] S. M. Perlow and B. S. Perlman, "A Large Signal Analysis Leading to Intermodulation Distortion in Abrupt Junction Varactor Upconverters," **IEEE Trans. MTT,** Vol. MTT-13, No. 6, p. 820, Nov. 1965.

[3] P. Torrione and S. Yuan, "Multiple-Input Large Signal Mixer Analysis," **RCA Rev.,** Vol. 26, p. 276, June 1965.

[4] L. Becker and R. L. Ernst, "Nonlinear-Admittance Mixers," **RCA Rev.,** Vol. 25, p. 662, Dec. 1964.

Review of Gas-Breakdown Phenomena Induced by High-Power Lasers—I*

I. P. Shkarofsky

RCA Limited, Ste. Anne de Bellevue, Quebec

Abstract—This review concerns high-power laser interaction with gaseous media leading to breakdown. Laser-induced gas breakdown, the mechanisms involved, and experimental data are summarized. CO_2 lasers and atmospheric breakdown are of particular interest here. Phenomena related to discharges maintained, guided, or controlled by lasers are included. Finally the dynamics of a laser-induced breakdown spark and the expansion waves possible are outined.

1. Gas Breakdown

1.1 Concepts

If radiation intensity exceeds a certain threshold value, the medium can break down. The transmitted radiation is then greatly attenuated, and this can severely affect the use of high-power laser beams.

* Two additional papers in this series, "Review of High-Power Laser Damage to Materials" and "Review of Industrial Applications of High-Power Laser Beams", are planned for future issues of *RCA Review*.

The field of gas breakdown by lasers is still not completely understood even though hundreds of papers have been published in the last five years. Studies have been made of the threshold dependence on pressure, wavelength, type of gas, and pulse duration as well as the properties, development, and decay of the spark. For the sake of brevity, we will consider here mainly results for CO_2 lasers. The discussion follows that of Alcock,[1] DeMichelis,[2] and Raizer[3] (Ref. [3] contains a bibliography of papers up to May 1968).

The two mechanisms generally invoked to explain the breakdown phenomenon are illustrated in Fig. 1 (after Bunkin and Prokhorov[4]; also given in Alcock[1]).

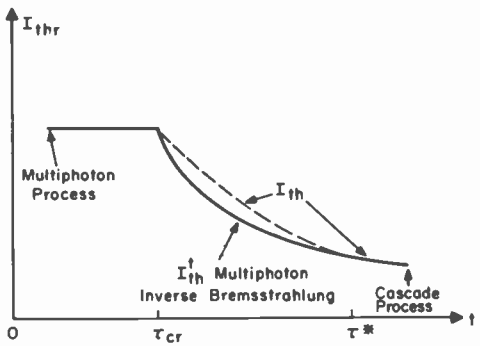

Fig. 1—Predicted variation[4] of threshold intensity with pulse duration

The first mechanism is the multiphoton ionization process, and it is important only at low pressures and in the case of extremely short (subnanosecond) pulses. In this process, an atom absorbs a number of photons, leading directly to ionization or to excitation followed by photo-ionization. Although the cross section for this mechanism is extremely small, nonetheless the process depends strongly on intensity as I^n. Here, n is the number of photons absorbed, equal to the integral part of $1 + E_I/\hbar\omega$ where E_I is the ionization energy and h is Planck's constant. This mechanism may also supply the initial electrons, especially if any impurity with a low ionization potential is present. The intensity breakdown threshold has a very weak dependence on pressure as $p^{-1/n}$. For very short pulses, when there isn't enough time for an avalanche type of breakdown to develop, the multiphoton process is operative. The multiphoton effect is the high-frequency version of the tunnel effect in which one electron is extracted from an atom by a static or low-frequency field; the two effects are limiting cases of the

same process. Some modifications of this picture arise due to the possible existence of local fields exceeding the average field; the strong electric field acts to smear out the atomic upper levels and to affect the atomic intermediate levels. All of these factors tend to decrease the breakdown field, as compared to values computed without these corrections.

In the opposite limit, at high pressures and long pulse lengths, the second mechanism of cascade ionization dominates. A few initial electrons in the illuminated region, upon colliding with the heavy particles, gain energy from the em wave by inverse bremsstrahlung, until they attain an energy sufficiently high to induce ionization. This is a cascade process that continues until a sufficient number of electrons are produced, leading to breakdown in the focal region. The dotted line in Fig. 1 indicates the dependence that the breakdown threshold would have were the cascade process also operative at shorter pulse durations. The solid curve, however, shows the actual variation in the transition region, where a third process, called avalanche multiphoton inverse bremsstrahlung, is thought to operate. That is, an initial electron can absorb several photons simultaneously in the presence of the high laser intensity. The electron energy thus increases more rapidly until, when it is sufficiently high, ionization ensues. Repetition leads to avalanche. One can also have in the transition region an alternative process, whereby the electron energy in a very strong field need only increase sufficiently for excitation of the atom, which subsequently becomes rapidly ionized by absorbing only a few quanta.

Within the cascade ionization regime, if n_o is the initial electron density and n_f is the final density at breakdown, we have

$$n_f = n_o e^{\nu_i t} = n_o 2^k \text{ or } k = \ln(n_f/n_o)/\ln 2 = 1.44 \ln(n_f/n_o), \qquad [1]$$

where k is the number of generations in the cascade and ν_i is the ionization frequency. For example, for $n_o = 10^6$ and $n_f = 10^{19}\,\text{cm}^{-3}$, we have $k \approx 43$. The above presumes that no losses occur. More accurately, with particle loss,

$$dn/dt = (\nu_i - \nu_a)\, n - \nabla^2(Dn) - \beta n^2 \qquad [2]$$

has to be solved, where ν_a is the attachment frequency, D is the diffusion, and β is the recombination coefficient. The rate of energy ($\bar{\epsilon}$) gain by electrons is given by

$$\frac{d\bar{\epsilon}}{dt} = \frac{e^2 E^2_{\text{rms}} \nu_{\text{eff}}}{m(\omega^2 + \nu^2_{\text{eff}})}, \qquad [3]$$

where E_{rms} is the rms electric field of the laser, related to intensity I by

$$E_{rms} = (I/\epsilon_o c)^{1/2} = 19.41\, I^{1/2}, \qquad [4]$$

and E is in V/cm and I in W/cm^2. Also ν_{eff} is the effective electron–heavy-particle collision frequency, c is the velocity of light, e is the electron charge, and m is its mass. Offsetting this energy gain are possible losses due to elastic and inelastic collisions, energy losses that are, however, often unjustifiably neglected.

To achieve breakdown, we require that the gain given in Eq. [3] within the pulse time τ_p be greater than kE_I, where E_I is the ionization energy. In the absence of particle and energy losses, this reduces to the threshold condition:

$$I_{th} = \frac{\epsilon_o mckE_I(\nu^2_{eff} + \omega^2)}{e^2\tau_p\nu_{eff}}. \qquad [5]$$

Thus for short pulses the breakdown condition actually depends on the energy flux, $I\tau_p$ (measured in J/cm^2), in the absence of losses. If $\omega \gg \nu_{eff}$, which is so at atmospheric pressure, $I_{th} \propto \nu^{-1}_{eff} \propto p^{-1}$. If $\nu_{eff} \gg \omega$, which occurs at very high pressure, $I_{th} \propto \nu_{eff} \propto p$.

The longest pulse duration for which Eq. [5] is valid is determined by the loss times. In air, attachment is a major loss process. Diffusion can also be important for long pulses, in which case

$$I_{th} \propto \nu^{-2}_{eff} \propto p^{-2}. \qquad [6]$$

A first-order correction is to replace the factor k in Eq. [5],

$$k \rightarrow k + \left(\frac{D}{\Lambda^2} + \nu_a\right)\frac{\tau_p}{\ln 2}, \qquad [7]$$

where Λ is the diffusion length $\approx a/2.4$ and a is the spot radius.

Energy losses due to both elastic and inelastic collisions also should be considered. In weaker fields, the electron may lose energy to excitation much more often than to the occasional ionization. We see that if D or ν_a are important, i.e., if τ_p is greater than the loss time, the breakdown depends on I_{th} (measured in W/cm^2) and τ_p is not of concern.

Recently Canavan et al[5] at AFWL have performed a numerical solution of the energy distribution in clean air in order to predict break-

down thresholds for the CO_2 laser. Electrons are produced by impact ionization and lost by attachment to O_2 molecules. The inverse bremsstrahlung absorption by electrons, stimulated emission upon collisions, and excitation of vibrational and electronic states are included. Their predictions for standard temperature and pressure air (see Fig. 2) show a breakdown requirement of 10 J/cm^2 for very short pulses (less than 10 ns) and a threshold of 4×10^9 W/cm^2 for CW or for pulses greater than 0.1 msec. When $\tau_p < 10^{-8}$ sec, the energy lost to

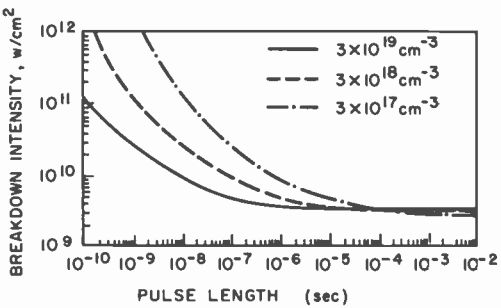

Fig. 2—Air breakdown flux[5] for 10.6 μm laser radiation as a function of pulse length for various final electron densities indicated in the figure.

excitation is small compared to that invested in ionization. Longer pulses waste an increasing fraction of the absorbed energy in excitation until, eventually, the decreased ionization rate balances the attachment losses, giving the constant I_{th} condition independent of τ_p.

Fig. 1 indicates that the shortest pulse duration for Eq. [5] to be operative is τ^* where[4]

$$\tau^* = \frac{k\bar{\varepsilon}E_I}{\nu_{\text{eff}}(\hbar\omega)^2}, \qquad [8]$$

where $\bar{\varepsilon} \approx e^2E^2/m\omega^2$ (for $\omega > \nu_{\text{eff}}$) is the average energy of the electrons.

In the transition region, the multiphoton inverse bremsstrahlung process has a threshold given by[4]

$$I_{\text{th}}{}^t = \epsilon_0 mc\hbar^2\omega^4/(e^2\bar{\varepsilon}) \qquad [9]$$

The transition region lies between τ^* and τ_{cr}, where

$$\tau_{cr} \approx kE_I/(\nu_{eff}\bar{\epsilon}). \qquad [10]$$

If $\tau < \tau_{cr}$, the multiphoton process is presumed to operate, since collisional processes are too infrequent. Typically, for ruby laser radiation, τ^* is 0.3 ns and τ_{cr} is 10 ps.

Anomalous results (see Sec. 1.2) have been observed that do not fit into the above picture. One of the main anomalies is the observed dependence of breakdown intensity on spot diameter. Further mechanisms, in addition to the various particle and energy losses mentioned above, are then postulated to explain some of these effects. These are:

(a) Particulate matter in the focusing region that provides the initial electrons.
(b) Atomic-excitation with resonant-radiation trapping. At some stage during the ionization process, electrons can create excited neutral particles. The excited atoms lose energy by radiation. For large focal spots, this radiation can be reabsorbed leading to a lower threshold breakdown.
(c) Self-focusing. The excited atoms have a polarizability much higher than the unexcited particles and this gives rise to an increase in the refractive index and to self-focusing. After some plasma is formed, the radial plasma displacement produces a central minimum in electron density or to a further increase in refractive index and further self-focusing.
(d) Superelastic collisions in rare gases at low pressure.
(e) Intense stimulated Raman scattering, which causes an energy loss.

1.2 Experimental Results

Table 1 gives experimentally observed values for laser breakdown of atmospheric air at various wavelengths.[6-15]

Pressure Dependence

The breakdown threshold varies as p^{-1} for cascade ionization (see Eq. [5]) when $\omega \gg \nu_{eff}$ and as p^{-2} with diffusion or attachment losses. Minck[16] investigated this dependence in N_2, H_2, He, and Ar for pressures between 0.3 and 100 atm using a ruby laser (3-5 Mw, 25 ns). For the molecular gases, the decrease of threshold with pressure was less steep than for the rare gases. Gill and Dougal[17] did a similar investigation of ruby laser (30 Mw, 50 ns) threshold versus pressure between 7-200 atm and found minima in Ar, N_2, and He at pressures above 100 atm. Theory predicts a minimum when $\nu_{eff} \approx \omega$.

For CO_2 laser radiation, the minimum pressure for breakdown

usually occurs at less than 45 atm and furthermore the threshold values are much lower (see Table 1). Experimental results are shown in Fig. 3(a) for Xe[18], in Fig. 3(b) for Ar,[18,19] and in Fig. 3(c) for H_2, N_2, Ar, and He[20] breakdown, all showing minima (except for H_2) in thresholds. The results of Generalov et al[18] were produced by a Q-switched CO_2 laser of 10 kW peak, 0.3-1.5 μs and 50-250 pps, focused

Table 1—Laser Breakdown Thresholds in Air

Laser Wavelength (μ)	Focal Spot Diam. (μm)	Pulse Duration (ns)	Threshold W/cm^2 or J/cm^2	Ref.
10.6	—	less than 1ns	10J/cm^2	[5] (theory)
10.6	—	greater than 10^{-4}s	4×10^9 W/cm^2	[5] (theory)
0.694	200	30	5×10^{10}	[6]
1.06	200	10	0.3J (9×10^{10} W/cm^2)	[7]
0.53	200	7.7	0.5J (2×10^{11} W/cm^2)	[7]
1.06	—	0.01	5×10^3 J/cm^2	[8]
0.694	—	0.05	1.5×10^{14}	[9]
0.694	200	0.02—0.1	3.5×10^{12}	[10]
0.694	17	0.02—0.1	1.5×10^{14}	[10]
1.06	50	1.6	10^{12}	[11]
1.06	50	40	6×10^{11}	[11]
1.06	500	1.6 or 40	4×10^{10}	[11]
10.6	100	200	3×10^9	[12]
10.6	300	300	10^9	[12]
0.347	28	8	1.3×10^{11}	[13]
0.347	100	8	5×10^{10}	[13]
0.694	60	10	1.3×10^{11}	[13]
10.6	—	200	2×10^9	[14]
10.6	76	160	7×10^9	[15]
10.6	152	160	2.5×10^9	[15]
10.6	228	160	1.3×10^9	[15]

to an 80-μm-diameter spot. In He, they found that the threshold increased noticeably with increasing purity of the gas. Their results are compared by Alcock[1] with those of Smith[19] in Ar. Smith's work was done with a CO_2 laser of 100 kW and 0.2 μs, and he found it necessary to pre-ionize the gas. Pre-ionization, providing a 10^{11} cm^{-3} electron density, was obtained from a dc discharge with 2 cm electrode spacing in atm Ar. Without pre-ionization, no breakdown occurred even at 10^9W/cm^2. As compared to 1.06-μm radiation, the threshold for 10.6 μm is about 1000 times less. The results by Hill et al[20] in Fig. 3(c) are obtained with a TEA CO_2 laser (1 Mw, 200 ns, 100 μm diameter spot). Except for H_2, no pre-ionization is needed for the various gases. Between 250 and 3000 Torr, they find a pressure dependence as p^{-1} for Ar and He, whereas for N_2 and H_2 the dependences are as $p^{-2/3}$ and $p^{-1/3}$, respectively. They note that recombination loss is appreciable at

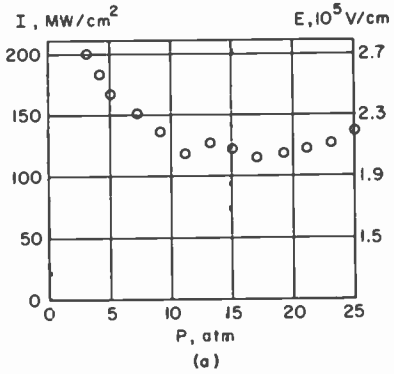

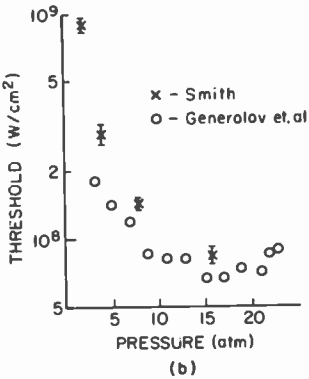

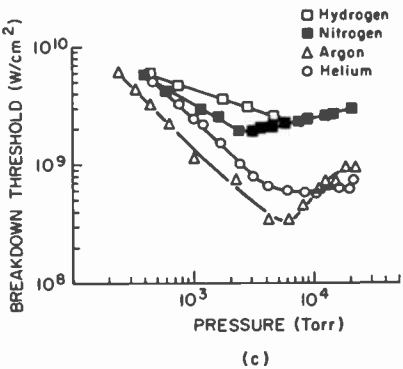

Fig. 3—Gas breakdown thresholds as a function of pressure at 10.6 μm radiation: (a) in xenon after Generalov et al,[18] (b) in argon after Generalov et al[18] and Smith,[19] and (c) in various rare and molecular gases after Hill et al.[20]

higher pressures in Ar. At 1 atm the threshold is an order of magnitude higher than predicted by simple cascade theory, suggesting another electron loss process such as production of excited states. In molecular gases, vibrational excitation also causes deviations from simple cascade theory. Cohn et al[21] have investigated the threshold conditions with a TEA CO_2 laser (0.9 J, 200 ns, 10^{10} W/cm^2) for He and Ar breakdown in the presence of a magnetic field (up to 8.7 teslas) directed along the laser propagation direction. The theoretical variation of $\nu_{eff}/(\nu^2_{eff} + \omega_b^2)$ (with $\omega_b = eB/m$, B being the magnetic field) can explain the experimental results semiquantitatively. No pre-ionization was required, although particulate impurities may have been present.

The threshold for breakdown in a mixture of Ar and He at 80 atm was investigated by Mulchenko and Raizer[22] using both an Nd and a ruby laser. Pure Ne has a higher breakdown threshold than pure Ar. However, a minute addition of Ne to Ar sharply decreases the breakdown threshold using the Nd laser but not with the ruby laser. No satisfactory explanation could be given. (It would be very interesting to repeat this experiment with a CO_2 laser.) With addition of a small amount of Ar to Ne, the threshold is again decreased sharply with the Nd laser but much less noticeably with the ruby laser. This is explained in terms of the greater probability of two-photon absorption of excited Ne atoms for ruby radiation as compared to 1.06-μm radiation.

Although the transition through τ_{cr} in Fig. 1 has been observed[9] in nitrogen at about 0.26 atm with a 50 ps ruby laser, DeWhurst et al,[23] using an Nd laser, have not observed such a transition in the rare gases. The threshold keeps on increasing in Ar as the pressure is decreased. Superelastic collisions are invoked to explain this result.

Dependence on Pulse Duration

Although Eq. [5] predicts a τ_p^{-1} behavior on pulse duration, experiments by Belland et al[11] find an intensity ratio of only about 3, instead of 25, as τ_p is changed from 40 to 1.6 ns; in addition, they find a decrease in threshold as the spot size is increased. They attribute these effects to self-focusing of the laser radiation.

Further evidence of self-focusing was obtained by interferograms,[24] with 10 ns ruby pulses in atmospheric air breakdown, which showed filaments several 100 μm long and a diameter about 10 μm, or 0.1 times the beam size. Additional plasma blobs were generated successively at intervals of 200-400 μm as the plasma advanced at a rate of 4×10^7 cm/sec towards the laser. Similarly, Bunkin et al[10] observed, with 20-100 picosecond ruby laser pulses, discrete breakdown regions separated by 1.5-2 mm in the focal region in air breakdown, with points as

small as 15 μm, although the beam spot size was 200 μm in diameter. Even though diffusion is completely negligible in the picosecond range, the decrease in breakdown threshold with increase in spot size was observed and attributed to self-focusing. Changes in the medium properties were also evident in that at a laser intensity just below breakdown, strong nonlinear scattering was observed from those points that seemed to break down at the higher intensities.

Smith[12] measured the Ar gas breakdown versus pressure (0.1-4 atm) and pulse duration with 50 and 200 ns pulses from a TEA CO_2 laser. Results are shown in Fig. 4(a). The pressure dependence, in Fig. 4(a), is $p^{-0.7}$ and is weaker than expected. Since the number of J/cm^2 is

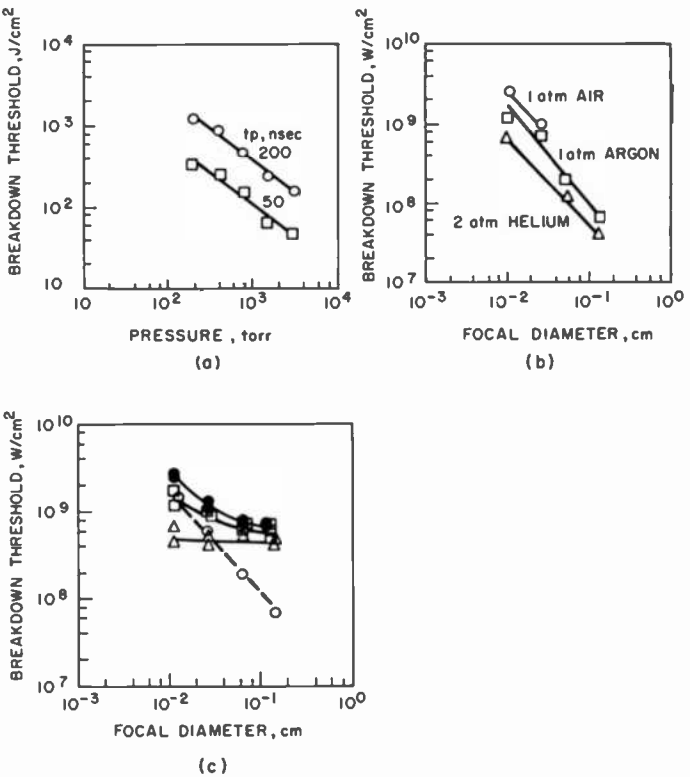

Fig. 4—Gas breakdown thresholds with a CO_2 laser beam in (a) argon with a focal spot diameter of 0.01 cm for various pulse widths,[12] (b) air, helium, and argon with a laser pulse duration of 200 ns,[12] and (c) helium for various initial electron densities. In (c) Δ, $n_{e_0} \approx 10^{13}$ cm^{-3}; $\square$, $n_{e_0} \approx 2 \times 10^{11}$ cm^{-3}; $\bullet$, no preionization; o, no preionization but with particulate matter probably present (data in (b)).

proportional to τ_p, it appears that I (in W/cm^2) is independent of τ_p. This points towards a balance between energy absorption and energy loss for pulses longer than 50 ns in Ar. Sec. 1.1 shows that such a behavior can be expected at longer pulse lengths.

Dependence on Spot Size

It was found[25] that the breakdown threshold intensity decreases as the spot size increases. Such an effect is contradictory to Eq. [5], but would arise if diffusion effects were important. However, the observations encompass[10] subnanosecond pulses, which are so short that there is no time for diffusion to operate. The decrease of gas-breakdown threshold with increasing beam diameter has significant bearing on the propagation of high-power pulsed CO_2 radiation.

Smith[12] has also performed measurements on the CO_2 laser breakdown dependence on the focal diameter in air, Ar, and He. Results are shown in Fig. 4(b). He states that air can be broken down if some contaminant is present, but dry nitrogen doesn't breakdown even at 10^{10} W/cm$_2$. Both Figs. 4(a) and 4(b) indicate an electron loss mechanism. However, Smith claims that this is not diffusion, since Fig. 4(b) doesn't show a Λ^{-2} variation but rather a Λ^{-1} variation. for focal diameters greater than 10^{-2} cm as used in these experiments, diffusion times are too long and can be neglected. He ascribes the loss process as due to atomic-excitation resonant-radiation trapping, discussed at the end of the previous subsection. A different explanation is given by Canavan et al[5] and Marquet et al[14]. They ascribe the observed dependence on spot size to the presence of particulate contaminants, viz., on the probability of finding within the focal volume a particle that is sufficiently large to produce the initial plasma.

Marquet et al[14] also use a TEA laser (3 J, 3×10^6 W peak) for air breakdown experiments. For very clean air, no breakdown occurs even at 10^{10} W/cm^2, agreeing with Smith. For ordinary air containing micron dust particles, the threshold is 2×10^9 W/cm^2 (see Table 1). With 20-μm particles dropped in, the threshold can be reduced to 10^8 W/cm^2. The breakdown threshold over the 0.4-1 atm range varies as $p^{-2/3}$ for ordinary air.

Preionization can provide an important source of initial electrons for gas breakdown as found by Smith. Recently, controlled experiments on the effect of pre-ionization were performed by Brown and Smith[26] with CO_2 TEA laser striking pure He (no particulates) at atmospheric pressure. An afterglow in the medium provided a controlled level of 10^{10}-10^{13} cm^{-3} pre-ionization. Fig. 4(c) shows the breakdown threshold versus spot size for various pre-ionization levels

and includes the data for He shown in Fig. 4(b). With a high initial electron density (about 10^{13} cm^{-3}), the threshold is much lower than without pre-ionization and it doesn't show any spot-size dependence. This is because at these high densities, the diffusion process is ambipolar and the diffusion time consequently is long, even though the spot diameter is small. On the other hand, at lower initial densities, and for focal diameters smaller than the Debye length, free electron diffusion occurs with a resultant dependence on focal size. The data taken from Fig. 4(b), showing a volume dependence for large focal volumes, is now ascribed to the presence of particulate matter.

A complementary experiment using UV as a pre-ionization source was reported by Robinson,[17] also using a TEA CO_2 laser (200 μm diameter) to break down Ar gas at pressures between 100-600 Torr. The UV source is a spark discharge that can be positioned 3.8-12.7 cm away from the laser focal region. He finds as well that with fresh gas, breakdown is much harder than in a gas in which ionization is once achieved. In the presence of UV, a lowering of the threshold is observed, the degree increasing with decreasing distance between the UV source and the focal region and with decrease in pressure. UV-initiated electrons seem to exist even 1 ms after the UV pulse, since threshold lowering is still observed then. Besides Ar, the lowering is also found in N_2 and He but not in CO_2, air, and a laser mixture of CO_2, He, and N_2. This is attributed to the presence of dust particles in the latter gases, which provide more initial electrons than the UV source.

More recent results for breakdown with a CO_2 laser (0.26 J, 0.16 μs, 10^{10} W peak) are reported by Chan et al.[15] They measure breakdown as a function of pressure between 0.3 and 13 atm and for various spot sizes. The gases used are Ar, Ne, He, O_2, and air. Results are shown in Figs. 5(a-d) and 6. Breakdown is defined by them as the intensity providing breakdown for 50% of the shots (rather than 1% as defined by Smith and coworkers) after ionization is once initiated. Clean unused gases are much more difficult to break down. Their results are fitted (not shown in the figures here) with an approximate theory that includes various particles and energy-loss mechanisms. Even for large beam spots, some loss process is found to occur. Energy losses due to inelastic collisions are important, especially for the molecular gases. In atomic gases, the decrease in threshold with pressure becomes less rapid as the focal volume becomes larger. Since it never decreases as rapidly as p^{-2}, free electron diffusion is not the only loss mechanism. Inelastic collisions are also important for the inert gases. In all gases, the threshold is observed to decrease as the focal volume

increases. Figs. 5(d) and 6 show that breakdown in oxygen and in air is rather insensitive to pressure in the 0.3-13 atm range.

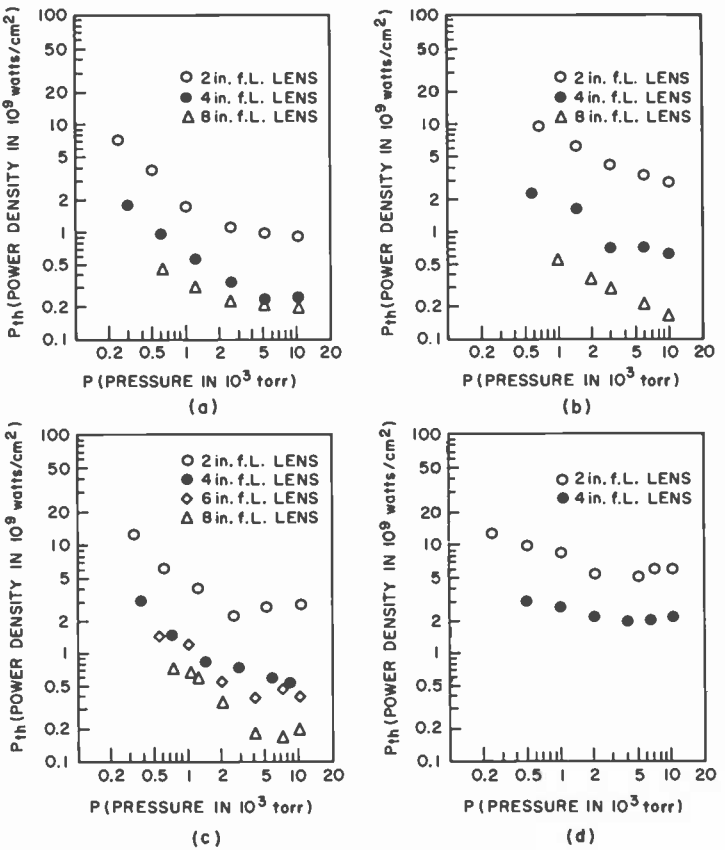

Fig. 5—Power density threshold[15] versus gas pressure at different breakdown volumes with a CO_2 laser beam in (a) argon, (b) neon, (c) inch fl lenses are, respectively, 76 μm, 152μm, 228 μm, and 304 μm.

Berger and Smith,[28] using a double-discharge TEA laser (9 J, 70 ns, 45 MW peak), investigate breakdown in a mixture of CO_2, He, and N_2. Their results are shown in Fig. 7 as a function of focal diameter for various pressures. At atmospheric pressure and for beam diameters larger than 0.2 cm, the threshold levels off at 1.4×10^8 W/cm^2, or 10 J/cm^2 for the 70-ns pulse. For lower pressures the dependence is as $p^{-0.7}$, similar to that in Ar. The dependence on spot size is attributed either to atomic-excitation resonant-radiation trapping or to particu-

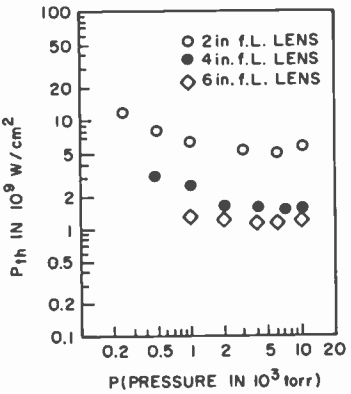

Fig. 6—Breakdown threshold[15] in air with a CO_2 laser beam. Conditions as in Fig. 5.

late matter. If the mixture is ionized as in a lasing medium, they estimate that the threshold is reduced to 5 J/cm^2, giving the threshold formula $5p^{-0.7}$. This sets an upper limit on the operating pressure of pulsed CO_2 lasers. The laser output however increases with p. They estimate that in a lasing mixture, the laser saturation flux varies as $0.5p$ in J/cm^2. Combining these two formulas yields the maximum operating pressure in CO_2 lasing media for given extraction efficiencies. This pressure lies in the 2-4 atm range.

In the same work, Berger and Smith also give experimental values on breakdown thresholds of atmospheric air versus pulse duration for various spot diameters. Results are shown here in Fig. 8. The 45° lines only apply if the threshold is above its minimum value of 10 J/cm^2.

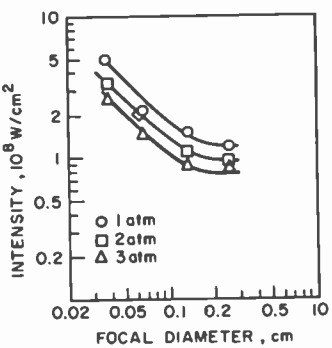

Fig. 7—Breakdown threshold[28] with a CO_2 laser in a 5:1:1 mixture of $He:N_2:CO_2$ at 1, 2, and 3 atm.

Besides the work of Berger and Smith, breakdown within the CO_2 laser cavity is also investigated by Tulip et al[29] and by Karlov et al.[30] Tulip et al[29] produce breakdown in air by focusing the radiation inside a TEA CO_2 laser cavity. Pressure cells can be placed in the high-intensity focal region and breakdown can be investigated to pressures less than 100 Torr. They observe an initial intense breakdown followed later by a sequence of less-intense breakdown points. Most of the laser energy within the 200-ns pulse is absorbed by the initial breakdown. Karlov et al,[30] using again a TEA CO_2 laser, but with a

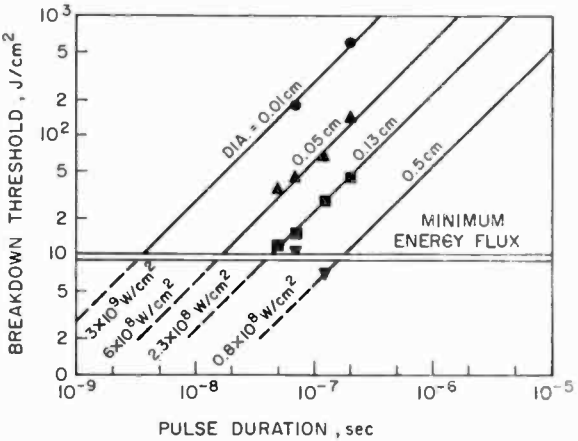

Fig. 8—CO_2 laser breakdown threshold energy flux[28] of atmospheric pressure air as a function of pulse duration. The 45° lines are drawn through the experimental points and each is labelled by the appropriate beam diameter.

longer pulse of 10 μs, observe new effects. Just before breakdown, the radiation develops self-modulation and the laser pulse breaks up into a series of pulses. The pulses stop after 30 μs, the quenching being due to self-defocusing associated with the decrease of refractive index by the electron density.

Wavelength Dependence

Experiments[31,32] with different laser wavelengths at constant pressure reveal that the breakdown threshold intensity has a maximum in the 0.3—1 μm wavelength region and becomes lower both for larger and smaller wavelengths. As already mentioned, at 10.6 μm, the threshold is lower by several orders of magnitude, which is to be expected ($I_{th} \propto \lambda^{-2}$) from Eq. [5] with $\omega \gg \nu_{eff}$. The decrease at short wave-

lengths however disagrees with the theory for cascade ionization. Multiphoton ionization is also ruled out because of the strong pressure dependence that is observed. No satisfactory explanation exists, although a mechanism has been suggested for the situation where electron excitation of atoms is an important energy-loss mechanism. There is a possibility that this loss is reduced at shorter wavelengths due to more rapid multiphoton ionization from excited states.

Alcook et al[13] also observe a similar decrease upon comparing wavelengths of ruby and 0.347 μm radiation used to break down air, CH_4, and D_2. In H_2, however, an increase in threshold is found at low pressure. They also observe in H_2 and CH_4 a pronounced knee in the pressure dependence above atmospheric. This is attributed to loss of incident radiation by intense stimulated Raman scattering. Mennicke[33] also finds that the Raman process is operative in the initial phase of breakdown of H_2, D_2, and N_2 solid targets.

2. Additional Laser Breakdown Situations

In this section we discuss three additional breakdown situations involving lasers. The first concerns discharges maintained by lasers, the second is discharges guided by lasers, and the third is spark gaps controlled by lasers.

2.1 Discharge Maintained by Lasers

A discharge ignited by some other means (e.g., another laser) can be maintained by a laser whose intensity is weaker than the breakdown threshold and with the plasma positioned in the laser's focal region. A cw CO_2 laser has been shown[34-37] capable of maintaining a continuous discharge. The initial breakdown of the gas can be accomplished with another pulsed CO_2 laser.

Generalov et al[34] investigate "optical discharges" in Xe and Ar at pressures of 1-45 atm maintained by 40-250W of cw CO_2 laser power. They observe a conical glow region along the diverging cone of the beam, and the discharge stability is associated with this geometry. The conical glow represents a "combustion wave," propagating from the breakdown point to an outer stationary position towards the laser, where the intensity is too low to maintain the discharge. With 40 W cw power maintaining a 6.5-atm Xe discharge, the plasma velocity decreases rapidly from 10^3 cm/sec to zero in this cone. With increasing power at a given pressure, the discharge increases in size. At a given laser power, there are upper and lower pressure limits for

which a stable horizontal discharge exists. The energy input by the laser should balance losses due to heat conduction and radiation. At relatively low pressures (about 1—2 atm) heat conduction losses prevail and depend little on pressure. Since laser energy absorption increases with pressure, threshold power decreases as the pressure increases. Between 10 and 25 atm, the threshold is independent of pressure, since radiation losses are balanced here. For still higher pressures, there is a limit on the stability possible with a horizontal beam due to convective effects. With a vertical beam position, no upper limit is observed, even up to 45 atm, although occasional "tongues" of flame occur in the 30-45 atm range, again associated with convective flow. Generalov et al also measure an average transmission of 40% of the laser energy, which corresponds to an optical thickness of the plasma approximately equal to unity. For 250-W laser input in Ar gas, the electron density at 2 atm is $3.5 \times 10^{17}\,cm^{-3}$ and about $5 \times 10^{17}\,cm^{-3}$ in the 4—16 atm range. The electron temperature is about 23,400 °K at 2 atm and decreases to 15,000 at 4 atm and 13,000°K at 16 atm. To a first approximation, the gas temperature is about the same.

Moody[35] also investigates a cw discharge in Ar ignited by a pulsed CO_2 laser and maintained by a cw CO_2 laser. They measure an increase in the breakdown threshold field of the pulsed beam when the cw laser field is on. The change in threshold depends on gas pressure and on cw power. At 1 atm with 324 W of cw power, the threshold is increased by 38%. They suggest that this effect occurs because the cw field is heating the neutral atoms within the breakdown volume and, thereby, lowering their number density. This results in a lower electron–neutral collision frequency and in a higher breakdown threshold (see Eq. [5]).

Similar studies to those of Generalov et al[34] were performed by Franzen.[36,37] He uses a TEA CO_2 laser to pre-ionize Ar gas and a cw CO_2 laser to maintain the plasma. (His breakdown threshold values[36] in Ar with the TEA laser itself are similar to those of Chan et al[15] shown in Fig. 5(a).) CW breakdown[36] is obtained in Ar at 4.4 atm with 150 W cw power (TEM_{11} mode), and it is necessary to decrease the focal half-angle, θ, to less than 5 mrad. This corresponds to a cw intensity of $2 \times 10^6\,W/cm^2$ as compared to the breakdown threshold of $4.2 \times 10^8\,W/cm^2$ for the TEA laser by itself, i.e., about two orders of magnitude less intensity. A conical discharge region is found to exist, whose luminosity increases with cw power. At 300 W input, the pressure could be reduced to 2.4 atm before extinction occurs. Spatial extents of a few millimeters with a continuum emission peaked

in the UV are typical plasma characteristics. In later work[37], Franzen uses a cw laser operating in the TEM_{20} mode to maintain the plasma but finds that successful ignition depends on the energy of the pulsed TEA CO_2 laser. Too high a pulse energy fails to ignite the continuous plasma, the optimum energy being less than 40 mJ, or near the breakdown threshold value for the pulsed laser itself. Ignition failure at high energies is attributed to electron density reduction caused by a plasma expanding too rapidly. Values for the threshold cw power necessary to maintain the discharge in various gases (Xe, Kr, Ar, Ne, He, and N_2) are given, and generally lie between 1.5×10^6 and 1.2×10^7 W/cm^2 for pressures between 4 and 12 atm, respectively. For 280 W input, the lowest pressure could be reduced below 1 atm only in Xe. Plasmas are more easily obtained in the noble gases with the lowest ionization potentials.

Continuous plasmas sustained by lasers may have important implications. If a plasma exists, such as that produced by laser breakdown of targets, then further propagation to the target may be severely hampered by the 100-fold lower threshold of laser intensity that can maintain this plasma. On the other hand, if a high-temperature and high-density cw plasma is desired, this can be obtained, as described, with relatively low laser input power.

2.2 Discharges Guided by Lasers

A high-voltage electrical breakdown streamer (or ionizing potential wave) can be induced to travel through the atmosphere along a path traversed beforehand by a high-power laser pulse. The laser can either generate an ionization breakdown tail[38,39] or it can produce a thermal rarefraction channel.[40] In the former case, the trail lifetime is short, since it is limited by electron recombination. In the latter case, the rarefraction channel decays much more slowly via thermal conduction and convection. By arranging for the laser channel to be in contact with a high-voltage electrode, a breakdown streamer can be initiated that will subsequently travel in this same channel.

Consider first the laser ionization trail. Using an Nd-glass laser[38,39] 86 J, 2.2 GW, 35 ns, 10^{11} W/cm^2, 0.38 cm diam.), a 350 kV streamer is made to propagate 28 cm along a laser trail in a straight path, rather than the crooked one it would follow if unguided. The gap between electrodes is 63 cm in this case and the discharge is fired 40 μs after the laser pulse. The streamer propagates by means of ionization avalanche processes starting at its tip where the diameter is small and the electric field is intense. The streamer tends to follow the laser

trail within which the cascade ionization process is more rapid or efficient. Where the laser intensity is lower, the discharge assumes an irregular path. The streamer velocities for 300 kV are between 10^5 and 10^6 cm/sec. The average electric field required to produce the interelectrode discharge is reduced from 7.3 to 5.5 kV/cm. Luminous beads from optical breakdown sometimes appear along the guided path.

The work on the thermal rarefraction channel in air was accomplished[40] with a CO_2 laser. Air absorbs a significant fraction of the 10.6—μm laser energy passing through it. It is heated rapidly and consequently expands, generating a transient low pressure cylinder through which the electrical streamer can travel. In the experiment, air is doped with ammonia to produce stronger laser absorption. A 50—75 W CO_2 laser, with a pulse width of 0.15 sec, is made to traverse a 50-cm air column vertically, in order to minimize convective effects. The absorbed energy is about 5 J. The high-voltage pulse is applied just prior to the laser termination. With 112-kV pulse and 10% ammonia, the arc discharge is guided without irregularities through 12.7 cm. With 15% ammonia and a laser pulse width of 0.3 sec, the absorbed energy is about 11 J and the arc length is extended to 14 cm.

Potential applications[39] include electrical energy transmission, improved devices for controlling and studying natural lightning, novel techniques for use with high-voltage power sources, and the establishment of antenna-like regions for communication purposes.

2.3 Spark Gaps Controlled by Lasers

Even below the breakdown threshold intensity, laser radiation focused between electrode gaps can trigger sparks at high speed over modest distances and at relatively high average fields (greater than 1.5×10^4 V/cm). This provides an inherently safe, simple, high-current, and high-voltage ns switch. Additional advantages are (a) no electrical coupling between laser trigger and high-voltage gap, (b) the capability of splitting the laser beam in order to trigger multigaps synchronously, and (c) jitters of the order of only 1 ns and formative time lags less than that observed in electrical triggering. For high-voltage gaps, the breakdown is attributed to ionization avalanche streamers. For low-voltage gaps (below 2kV but sufficient laser power to form a plasma) ultraviolet emission from the plasma plays a role in reducing the formation time lag between laser firing and the spark discharge.

Pendleton and Guenther[41] use a ruby laser (80 MW, 10^{10} W/cm^2, 10 ns half width) to trigger a gap whose spacing is 0.4—1.5 cm and study the time delay between laser pulse and current gap flow. Delay times less than 10 ns are observed in SF_6 at atmospheric pressure. The delay varies inversely with electric field, gas pressure, and focal-point distance from the anode surface. Results are also obtained for N_2 and air at varying pressures between 100 and 1400 Torr. Further works are reported by Guenther and Bettis[42] and Guenther and McKnight.[43] Akmanov et al[44] use a UV laser beam at 0.265 μm (4th harmonic of Nd laser) with 10 ns pulse duration and 3×10^8 W/cm^2 to break down an air gap of 1 cm. The breakdown voltage is 13 kV instead of 17 kV, which it would be without the laser. Also the laser energy density would have to be at least 100 times higher without the applied voltage. Vladimirov et al[45] investigate the resistence characteristics of the laser spark gap. A ruby laser (7 MW, 15 ns) is used by Khan and Walsh[46] to trigger various gases. Faster switching, viz., a lesser delay time, is observed by using O_2 or air instead of N_2 or by increasing the amount of Ar added to N_2. Other efforts in this field, to name a few more, are those of Klewe et al.,[47] Schmitter,[48] Pillsticker,[49] and De Whurst et al.[50] Pillsticker[49] finds that it is beneficial to admit the laser beam to the gap through a hole in one of the electrodes in order for the beam to be parallel to the electric field direction. This provides a high value of the first Townsend coefficient. A high pressure is desirable in the gap and the laser pulse should be short. De Whurst et al[50] investigate picosecond triggering with a 7-ps mode-locked Nd glass laser. They obtain formative time delays of the order of 1 ns. They attribute the few electrons present before avalanche to thermoionic emission from the cathode within the focal area.

At Hydro-Quebec (IREQ), a ruby laser is being used to test extra-high voltage circuit breakers for high-voltage transmission lines.* An Nd–glass laser (30 J,25 ns) will also be used to trigger a series of spark gaps with voltages up to 1.5 MV and with rated interrupting capacitors up to 6×10^{10} volt-amperes.†

3. Dynamics of the Laser Spark

3.1 Spark Parameters

Starting with the classic works of Ramsden and Davies[51] and Ramsden and Savic,[52] there have been a multitude of experiments and interpretations on the dynamics of the laser spark.

* *Laser Weekly*, p. 6, June 18, 1973.
† *Laser Weekly*, p. 4, June 11, 1973.

Generally, it is found that immediately after breakdown and while the laser pulse is still on, the plasma expands towards the focusing lens, i.e., towards the laser. The transverse expansion is very much less. An abrupt attenuation occurs in the laser transmitted signal, mainly due to laser absorption. Initial velocities are of the order of 10^7 cm/sec, and in laser-scattering experiments, one observes corresponding Doppler shifts. The initial electron densities are of the order of a few times 10^{19} cm^{-3} and the electron temperatures are about 10^5—10^6 °K. At these values, the absorption length for laser radiation is very small, less than a millimeter. On the other hand, the characteristic reradiated photons having $\hbar\omega \approx \kappa T$ are in the very far UV and their photon mean free path is long (several centimeters). Consequently, the absorption layer within the spark for laser energy is thin and abrupt, whereas the plasma is more or less transparent to its own spontaneous radiation.

Based on their laser scattering experiment, Ramsden and Davies[51] conclude that the ion temperature (T_i) is less than 10 eV so that $T_i \ll T_e$. This conclusion is in disagreement with theory, which predicts $T_e \approx T_i$. Tomlinson[53] attributes this discrepancy to self-focusing, which creates localized interfaces of ionization. Laser energy scattered from such regions would not be appreciably broadened and thus a low T_i value would be deduced. He also provides experimental evidence for this phenomenon and finds centers of 10 μm diamater, although the focal spot is 30μm.

3.2 Expansion Mechanisms

At least four types of expansion waves are postulated to explain the total time history of the spark.

Radiative Detonation Wave

The first is called the radiative detonation wave and occurs while the laser is on. The laser supplies the reaction energy, which, after absorption by the plasma, drives a detonation as given by the Chapman–Jouget theory. The velocity of the detonation or hydrodynamic expansion shock front is given by[2, 3]

$$v_{\parallel} = \left[\frac{2(\gamma^2 - 1)\, P_o\, t)}{\rho_o \pi r^2} \right]^{1/3}, \qquad [11]$$

where γ is the adiabatic index, P_o is the absorbed laser power, r is the expanding spot radius, and ρ_o is the density in front of the shock

front. [Raizer[3] points out that ρ_o should be used rather than the density behind the shock front as written in Ramsden and Savic.] If θ is the half angle of the focused incident beam, z is distance towards the laser, and r_o is the minimum focal radius, then $r = r_o + z \tan\theta \approx z \tan\theta$ and the flow expands to fill up the solid angle subtended by the focusing lens. Integrating $v_\parallel = dz/dt$ gives

$$z = \left[\frac{2(\gamma^2-1)}{\pi\rho_o \tan^2\theta}\right]^{1/5}\left\{\frac{5}{3}\int [P_o(t)]^{1/3}\,dt\right\}^{3/5}. \qquad [12]$$

If P_o is constant in time, we have

$$z = \left(\frac{5}{3}\right)^{3/5}\left[\frac{2(\gamma^2-1)P_o}{\pi\rho_o \tan^2\theta}\right]^{1/5} t^{3/5}. \qquad [13]$$

The specific internal energy after absorption is then increased by

$$\epsilon = \frac{\gamma}{(\gamma^2-1)\ (\gamma+1)}\, v_\parallel{}^2 = \frac{2^{2/3}\gamma}{(\gamma^2-1)^{1/3}\ (\gamma+1)}\left(\frac{P_o}{\pi r^2 \rho_o}\right)^{2/3}$$
$$= \frac{2\gamma}{(\gamma+1)\ v_\parallel}\,\frac{P_o}{\rho_o \pi r^2}. \qquad [14]$$

The perpendicular (lateral) expansion velocity is given by

$$v_\perp = [\gamma(\gamma-1)\epsilon]^{1/2} = \gamma v_\parallel/(\gamma+1). \qquad [15]$$

Ramsden and Savic[52] show that the $z \propto t^{0.6}$ prediction agrees with the observed $t^{0.65}$ dependence for the ruby-laser-induced expansion. The $(P_o/\pi r^2)^{1/3}$ slow variation in Eq. [11] for $v_\parallel$ is found correct by Mandelshtam et al.[54] Daiber and Thompson[55] give a formula generalizing Eq. [13] for a Gaussian time pulse shape for $P_o(t)$ and find that the time lags from laser start to breakdown and breakdown to peak power are important parameters. The slopes for $\ln z$ versus t vary between 0.6 and 0.9, depending on experimental conditions. Further corrections can be given to include lateral expansion which reduces the above estimated $v_\parallel$. Using a ruby laser (0.7 J, 30 ns) to produce sparks in H_2 and He at 1—11 atm, Iznatov et al[56] study the time dependence of $v_\perp$ and $v_\parallel$. The values of $v_\parallel$ generally agree with Eq.

[11]. For late times, $v_{\parallel}$ decreases more rapidly for a gas at lower density. The explanation is that at higher pressure (11 atm), the absorption layer is thin and a laser supported detonation wave arises. At the lower pressure (1.75 atm), the energy release and absorption are not well localized and consequently the velocity is decreased.

Raizer[3] points out that if any of the ionization or breakdown mechanisms produces a supersonic heat wave that exceeds the detonation velocity in Eq. [11], then no shock wave is produced. A shock only occurs if the heat wave is subsonic with respect to the detonation wave.

Recently, Ahlborn[57] discusses extensively the dynamics of heat waves. Heat waves with abrupt steps in pressure and temperature result upon laser absorption within layers that are thin compared to the spark dimension. The shock velocity is on the other hand associated with momentum discontinuity, and, in general, the hydrodynamic and thermodynamic discontinuities travel at different velocities. The former travels at the local sonic speed as a sound or rarefraction wave if the momentum step is small and at the shock velocity if the step is large. The temperature or enthalpy step propagates, however, at a velocity proportional to $P_o/\pi r^2 \rho_o$. If the heat wave is supersonic, the shock wave is not observed. In many laser spark experiments, the laser input is so high that the wave starts off as supersonic; eventually, however, a shock wave must break loose after the velocity of the heat front decreases to the hydrodynamic velocity and becomes subsonic.

Radiation Transport Wave

This wave is described by Raizer.[3] He assumes that after breakdown the plasma radiates thermal energy, which ionizes the gas ahead of the laser absorption layer. As mentioned in Sec. 3.1, the mean free path for this thermal radiation is much larger than the spark dimensions. The gas in front then acquires the ability to absorb laser radiation and is rapidly heated. The boundary of the high-temperature region moves towards this heated gas, resulting in an expansion wave. The velocity of the expansion wave is close to the hydrodynamic velocity. It is most likely that the radiative and shock waves move together with the former heating the gas ahead of the shock front.

A similar mechanism, postulated by Ahlborn,[58] is valid during the final stages of a decaying spark after laser shutoff. He assumes that the shock is driven by a subsonic radiation front, which is powered by black body radiation from the center plasma (rather than by the heat wave associated with laser absorption). He deduces the behavior

$$v = \left[\frac{(g_2 + 1)^2 (g - 1)}{4g_2} \frac{P_o}{\rho_o \pi r^2} \right]^{1/3}, \qquad [16]$$

where g_2 and g are effective adiabatic indexes behind the shock and the radiation front. He assumes $P_o/\pi r^2$ to be proportional to the black-body surface radiation intensity, which in turn is proportional to T^4 and to $r^{-1/2}$. Thus, $v \propto r^{-4}$ and one gets $r \propto t^{0.2}$. Indeed, Daiber and Thompson[55] observe a $t^{0.21}$ dependence in the late decay stages of the spark, and this theory may explain their result.

Breakdown Wave

A third type of wave, envisoned by Raizer,[3] occurs during the fast rising portion of the laser pulse. When the power is appreciably in excess of threshold, breakdown at the focus occurs before peak power is attained. Further breakdowns can occur at various points in front of the focus at later times when the time-integrated laser energy has reached sufficient strength. For a triangular laser pulse shape, the breakdown wave travels at a constant velocity given by

$$v = \frac{dz}{dt} = \frac{r_o}{t_c \tan \theta} \text{ and } z = v(t - t_c), \qquad [17]$$

where t_c is the time of onset of the first breakdown at the focus and r_o is the initial focal radius. Now $t_c \approx r_o \tau_p^{1/2}/P_o^{1/2}$ where τ_p is the pulse duration and P_o is the laser power. Thus

$$v \approx \left(\frac{P_o}{\tau_p} \right)^{1/2} \frac{1}{\tan \theta}. \qquad [18]$$

For long pulse widths and short focal lengths, the breakdown wave velocity is of the order of $10^5 - 10^6$ cm/sec, much less than the hydrodynamic velocity. However, for short pulse widths and long focal lengths, the breakdown wave velocity can even exceed the hydrodynamic velocity. In this case, the elongated focal region is first traversed by the breakdown wave and then, when the channel expands sufficiently, the hydrodynamic mechanism takes over, either driven by laser radiation or by black-body radiation.

Ambartsumyan et al[59] interpret their results in terms of a breakdown wave. Alcock et al[60] explain their results in terms of a traveling-ionization breakdown wave with pre-ionization ahead of the breakdown wave. Krobkin et al[61] observe a discontinuous breakdown struc-

ture as the spark moves towards the laser. They interpret this in terms of a combined radiation transport wave and breakdown wave. The initial breakdown region becomes opaque to the laser radiation, but the gas in front becomes heated by plasma radiation leading to a new breakdown point, and the process repeats itself.

Taylor Blast Wave

A fourth type of wave occurs after the laser is shut off. This is the Taylor blast wave, described in Zeldovich and Raizer.[62] Although the initial energy release is in the shape of an elongated spark, it attains a spherical shape in the course of time. The blast velocity is given by

$$v = \frac{2}{5}\xi_o^{5/2}\left(\frac{\epsilon}{\rho_o}\right)^{1/2} r^{-3/2} = \frac{2}{5}\xi_o\left(\frac{\epsilon}{\rho_o}\right)^{1/5} t^{-3/5}, \qquad [19]$$

where ϵ is the total energy of the explosion and

$$\xi_o = \left[\frac{75}{16\pi}\frac{(\gamma-1)\ (\gamma+1)^2}{(3\gamma-1)}\right]^{1/5}.$$

Integration yields

$$r = \xi_o(\epsilon/\rho_o)^{1/5}t^{2/5}. \qquad [20]$$

Experimentally, Ramsden and Savic[52] interpret their $r \propto t^{0.38}$ dependence observed after laser shutoff in terms of the above blast wave. Since this wave occurs late in the afterglow, it may not be visible. Hall[63] produces blast waves in Ar (1-mm pressure and containing a Ta target) with a ruby laser. He verifies the above theory and finds $r \propto (\epsilon/\rho_o)^{0.18}$, in fair agreement with the 0.2 power predicted above. At higher pressures, the front surface develops instabilities. Hohla et al[64] also use a ruby laser (100 MW, 15 ns) to produce breakdown in gases at pressures from 200 Torr to 10 atm, and observe approximately spherical blast waves. For mach number greater than 4 in inert gases, or greater than 2 in diatomic gases, they verify the dependence of

$$\frac{r}{(\epsilon/\rho_o)^{1/3}} \propto \left[\frac{t}{(\epsilon/\rho_o)^{1/3}}\right]^{2/5}.$$

Adopting a value of $\gamma = 5/3$ provides better agreement than $\gamma = 7/5$. However, the predicted velocity is much too low for still later times. When the mach number is less than 2, the velocity barely falls below the sound velocity of the undisturbed gas.

At McGull University, Lee and Knystautas[65] apply the possibility of spherical blast wave formulation with lasers to ignition of chemically reactive gases and subsequent combustion. The laser spark is a perfect point energy source, free of contamination and heat transfer complications. They use a 120 MW, 10 ns ruby laser with a focal spot of 120 or 240 μm. Ignition is obtained in both nondetonable gases (propane-air or acetylene-oxygen-nitrogen mixtures) at atmosphere pressure or detonable gases (acetylene-oxygen mixture) at 20—120 Torr initial pressure. In the latter, a metal rod is used to produce some initial photoelectrons. No laser energy absorption is found before breakdown. The blast wave dynamics are influenced by the ratio of the laser spark energy to the total energy released by chemical reactions at any instant of time. For short times after ignition, this ratio is much greater than one and the $r \propto t^{2/5}$ blast wave variation applies. For long times, the ratio is less than unity, and the energy released by chemical reaction dominates the shock motion, which then changes to a Chapman–Jouguet detonation wave. It is found that for nondetonable gases, the effect of chemical reactions has negligible influence on the shock or blast wave motion. The reaction front then decouples rapidly from the shock. For detonable mixtures, there exists a critical energy above which direct initiation of a spherical detonation wave occurs. This critical laser energy varies inversely with the initial pressure of the mixture. For energies well above critical, the reaction and shock waves decouple, but close to critical the decoupling is followed by the re-establishment to a spherical detonation wave.

3.3 Results with TEA CO_2 Lasers

We will now discuss results obtained with TEA CO_2 lasers. Prior to breakdown with a TEA CO_2 laser (0.5 MW), Isenor and Richardson[66] observe luminesence in molecular gases (50 — 1000 Torr pressure) that absorb 10.6 μm radiation. The luminescence is characteristic of the molecular spectra of the dissociation products and is therefore associated with the dissociation of the molecules before ionization.

George et al[67] use a repetitive TEA CO_2 laser (1 — 2MW, 0.25 J, 12 pps) and investigate the first 15 μs of the laser produced spark. At 0.4 μs after breakdown, they find that the plasma is comprised of a dense hot core and a tenuous outer shell. The expansion energy seems

to have been dissipated by this time and the spark is virtually at a standstill.

Marquet et al[14], using a TEA laser, observe a plasma lasting for about 10 μs. For a laser input flux of 2×10^9 W/cm^2, the initial front velocity is 1.6×10^6 cm/sec, consistent with that expected from a laser-supported detonation wave model. After laser shut-off, a blast wave propagates out to a distance of 0.5 cm.

New effects are observed by Gravel et al,[68] who investigate sparks in various gases at pressures of 100 Torr to 1 atm with a TEA CO_2 laser having 0.1 — 0.6 J and 1 MW peak power. They find the existence of a filament that increases rapidly in length as the pressure is reduced towards the breakdown threshold. After breakdown, the plasma expands towards the laser at a velocity of 3×10^5 cm/sec. By the end of the initial 400-ns laser spike, the velocity is 10^6 cm/sec. Following this, the 5-μs tail of the laser pulse does not appear intense enough to support further expansion, and the luminosity *regresses* rapidly back towards the focal point. Eventually, the plasma becomes transparent and breakdown occurs again near the focus. After 1.5 μs, the strong absorption of the laser results in the production of shock waves which now travel both in the forward and backward directions.

Offenberger and Burnett[69] produce breakdown in H_2 at 50 — 700 Torr pressure with a TEA single-mode CO_2 laser (10 MW peak, 5×10^9 W/cm^2). At pressures above 100 Torr, the spark moves preferentially towards the focusing lens. This motion is consistent with the existence of a breakdown wave (Eq. [17]) during the rising portion of the laser pulse, followed by a laser-supported detonation wave (Eq. [11]). The predicted breakdown velocity is 4×10^7 cm/sec while that observed is 3×10^7 cm/sec at 150 Torr. At higher pressures (200 — 700 Torr) and at later times during the decay, they observe a second luminous front that propagates back towards the focal point, similar to that found by Gravel et al.[68] They explain this as due to the creation of two oppositely directed shocks by the pressure and density discontinuities during the spark decay. At low pressures, below 100 Torr, two luminous fronts are observed, one propagating backward towards the focusing lens and the other moving in the forward direction. The former correlates well with a laser supported detonation wave (Eq. [11]) and the latter is associated with incomplete laser absorption in the backward wave.

The above experiments were performed with TEA CO_2 lasers having a characteristic pulse comprised of an initial spike several hundred ns in width followed by a long tail of several μs. In contrast, MacPherson and Gravel[70] use an actively-mode-locked TEA CO_2 laser

having a train of pulses 3ns half-width separated by 25 ns. Some pulses have up to 3 — 5 MW peak power. Initial breakdown is produced in air at an estimated threshold of 8×10^6 V/cm or 1.7×10^{11} W/cm^2. After breakdown, the laser transmitted energy is sharply reduced. They observe a sequence of breakdown points whose positions move from the focus towards the laser during the first half of the pulse train; later the points regress towards the focus. As compared to their work with the normal pulsed TEA laser,[68] the present initial expansion, because of the short pulse length, is more like a blast-wave than a wave driven by laser radiation. Nonetheless, the present initial velocity (6×10^6 cm/sec) is comparable, because of the higher peak power in the mode locked laser. They do not find an exact $t^{2/5}$ variation (Eq. [20]) as expected for a blast wave. These results are compared with those of Wang and Davis[71] who use a mode-locked Nd-glass laser. Wang and Davis observe the initial migration towards the laser and it follows a $t^{2/5}$ blast wave dependence, but they do not observe the later return of the breakdown points towards the focus.

4. Summary

We have reviewed gas breakdown phenomena that occur at high incident laser powers. The breakdown mechanisms are expounded and experimental results on the threshold dependences on pressure, pulse duration, spot size and wavelength are summarized. Plots of results derived with CO_2 lasers are given. Additional breakdown interactions are then discussed, such as discharges maintained, or guided, or controlled by lasers. A final subsection considers the dynamics of the laser spark, namely four types of expansion waves, and recent results with TEA CO_2 lasers. Much of the phenomena involved still remain to be clarified.

Acknowledgment

This work was sponsored in part by the Defence Research Establishment Valcartier, Quebec, under DSS Contract Serial No. 2GR1-0325, DSS File No. 03GR.CD7020421.

References:

[1] A. J. Alcock, "Recent Developments in Laser Induced Gas Breakdown," NRC Report, Ottawa, presented at Symp. on High Power Molecular Lasers, Laval Un., Quebec City (1972).
[2] C. DeMichelis, "Laser Induced Gas Breakdown: a Bibliograpichal Review," **J. Quant. Electronics,** Vol. QE-5, p. 188 (1969).
[3] Yu. P. Raizer, "Breakdown and Heating of Gases Under the Influence of a Laser Beam," **Sov. Phys. Uspekhi,** Vol. 8, p. 650 (1966).

[4] F. V. Bunkin and A. M. Prokhorov, "Polarization, Matiere et Rayonnement," Societé Francaise de Physique, Paris, Presses Un. de France, p. 157 (1969).
[5] G. H. Canavan, W. A. Proctor, P. E. Nielsen, and S. D. Rockwood, "CO_2 Laser Air Breakdown Calculations," paper J3 presented at 7th Int. QE Conf., Montreal, May (1972).
[6] P. Nelson, P. Veyrie, M. Berry and Y. Durand, "Experimental and Theoretical Studies of Air Breakdown by Intense Pulse of Light," **Physics Lett.**, Vol. 13, p. 226 (1964).
[7] S. A. Akhmarov, A. I. Kovrygin, M. M. Strukov and R. V. Khokhlov, "Frequency Dependence of the Threshold of Optical Breakdown of Air," **JETP Lett.**, Vol. 1, p. 25 (1965).
[8] A. J. Alcock and M. C. Richardson, "Creation of a Spark by a Single Subnanosecond Laser Pulse," **Phys. Rev. Lett.**, Vol. 21, p. 667 (1968).
[9] I. K. Krasyuk, P. P. Pashinin and A. M. Prokhorov, "Investigation of Breakdown in N_2 Under the Influence of a Picosecond Ruby Laser Pulse," **JETP Lett.**, Vol. 9, p. 354 (1969).
[10] F. V. Bunkin, I. K. Krasyuk, V. M. Marchenko, P. P. Pashinin and A. M. Prokhorov, "Structure of a Spark Produced by a Picosecond Laser Pulse Focused in a Gas," **Sov. Phys. JETP**, Vol. 33, p. 717 (1971).
[11] P. Belland, C. De Michelis and M. Mattioli, "Self-Focusing in Laser Induced Gas Breakdown," **Optics Comm.**, Vol. 4, p. 50 (1971).
[12] P. C. Smith, "Gas Breakdown Dependence on Beam Size and Pulse Duration with 10.6 μ Wavelength Radiation,'" **Appl. Phys. Lett.**, Vol. 19, p. 405 (1971).
[13] A. J. Alcock, K. Kato and M. C. Richardson, "New Features of Laser-Induced Breakdown in the Ultraviolet," **Optics Communications**, Vol. 6, p. 342 (1972).
[14] L. C. Marquet, R. J. Hull and D. E. Lencioni, "Studies in Breakdown in Air Induced by a Pulsed CO_2 Laser," paper J2 presented at 7th QE Conference, Montreal (1972). Also D. E. Lencioni, "The Influence of Dust on 10.6 μm Laser-Induced Air Breakdown," **Appl. Phys. Lett.**, Vol. 23, p. 12 (1973).
[15] C. H. Chan, C. D. Moody and W. B. McKnight, "Significant Loss Mechanisms in Gas Breakdown at 10.6 μ," **J. Appl. Phys.**, Vol. 44, p. 1179 (1973).
[16] R. W. Minck, "Optical Frequency Electrical Discharges in Gases," **J. Appl. Phys.**, Vol. 35, p. 252 (1964).
[17] D. H. Gill and A. A. Dougal, "Breakdown Minima Due to Electron-Impact Ionization in Super-High Pressure Gases Irradiated by a Giant-Pulse Laser," **Phys. Rev. Lett.**, Vol. 15, p. 845 (1965).
[18] H. A. Generalov, V. I. Zimakov, G. I. Kozlov, V. A. Masyukov and Yu. P. Raizer, "Gas Breakdown Under the Influence of Long-Wave Infrared Radiation of a CO_2 Laser," **JETP Lett.**, Vol. 11, p. 228 (1970).
[19] D. C. Smith, "Gas Breakdown with 10.6 μ Wavelength CO_2 Laser Radiation," **J. Appl. Phys.**, Vol. 41, p. 4501 (1970).
[20] G. A. Hill, D. J. James and S. A. Ramsden, "Breakdown Thresholds in Rare and Molecular Gases Using Pulsed 10.6 μm Radiation," **J. Phys. D, Appl. Phys.**, Vol. 5, p. L97 (1972).
[21] D. R. Cohn, C. E. Chase, W. Halverson and B. Lax, "Magnetic-Field-Dependent Breakdown of CO_2-Laser-Produced Plasma," **Appl. Phys. Lett.**, Vol. 20, p. 225 (1972).
[22] B. F. Mulchenko and Yu. P. Raizer, "Laser Breakdown of Mixtures of Neon with Argon and the Role of Photoionization of Excited Atoms," **Sov. Phys. JETP**, Vol. 33, p. 349 (1971).
[23] R. J. De Whurst, G. J. Pert, S. A. Ramsden, "Breakdown in Gases with a Mode-Locked Train and Single Picosecond Light Pulses at 1.06 μm," **Proc. 10th Int. Conf. on Phen. in Ionized Gases**, Oxford, Vol. 1, p. 220 (1971).
[24] M. C. Richardson and A. J. Alcock, "Interferometric Observation of Plasma Filaments in a Laser-Produced Spark," **Appl. Phys. Lett.**, Vol. 18, p. 357 (1971).
[25] A. J. Alcock, C. DeMichelis and M. C. Richardson, "Breakdown and Self-Focusing Effects in Gases Produced by Means of a Single-Mode Ruby Laser," **J. Quant. Elec.**, Vol. QE-6, p. 622 (1970).
[26] R. T. Brown and D. C. Smith, "Laser-Induced Gas Breakdown in the Presence of Preionization," **Appl. Phys. Lett.**, Vol. 22, p. 245 (1973).
[27] A. M. Robinson, "Laser-Induced Gas Breakdown Initiated by Ultraviolet Photoionization," **Appl. Phys. Lett.**, Vol. 22, p. 33 (1973).
[28] P. J. Berger and D. C. Smith, "Gas Breakdown in the Laser as the Limitation of Pulsed High-Pressure CO_2 Lasers," **Appl. Phys. Lett.**, Vol. 21, p. 167 (1972).
[29] J. Tulip, K. Manes and H. J. Seguin, "Intracavity Radiation Induced Air Breakdown in a TEA CO_2 Laser," **Appl. Phys. Lett.**, Vol. 19, p. 433 (1971).
[30] N. V. Karlov, V. M. Komissarov, G. P. Kuzmin and A. M. Prokhorov, "Effect of Plasma Mirror in the Breakdown of Air in a CO_2 Laser Cavity," **JETP Lett.**, Vol. 16, p. 65 (1972).
[31] H. T. Buscher, R. G. Tomlinson and E. K. Damon, "Frequency Dependence of Optically Induced Gas Breakdown," **Phys. Rev. Lett.**, Vol. 15, p. 847 (1965).
[32] A. J. Alcock, C. De Michelis and M. C. Richardson, "Wavelength Dependence of Laser-Induced Gas Breakdown Using Dye Lasers," **Appl. Phys. Lett.**, Vol. 15, p. 72 (1969).

[33] H. Mennicke, "Observation of High-Order Stimulated Raman-Antistokes Radiation and Its Role in the Initial Phase of Plasma Production by Lasers," Max-Planck Inst. Report IPP IV/40, July (1972).
[34] N. A. Generalov, V. P. Zimakov, G. I. Kozlov, V. A. Masyukov and Yu. P. Raizer, "Experimental Investigation of a Continuous Optical Discharge," **Sov Phys. JETP,** Vol. 34, p. 763 (1972).
[35] C. D. Moody, "Effects of CW Power on the Pulsed Gas Breakdown Threshold in Argon at 10.6 μ Radiation," **App. Phys. Lett.,** Vol. 22, p. 31 (1973).
[36] D. L. Franzen, "CW Gas Breakdown in Argon Using 10.6 μm Laser Radiation," **Appl. Phys. Lett.,** Vol. 21, p. 62 (1972).
[37] D. L. Franzen, "Continuous Laser-Sustained Plasmas," **J. Appl. Phys.,** Vol. 44, p. 1727 (1973).
[38] J. R. Vaill, D. A. Tidman, T. D. Wilkerson and D. W. Koopman, "Propagation of High-Voltage Streamers Along Laser-Induced Ionization Trails," **Appl Phys. Lett.,** Vol. 17, p. 20 (1970).
[39] D. W. Koopman and T. D. Wilkerson, "Channeling of an Ionizing Electrical Streamer by a Laser Beam," **J. Appl. Phys.,** Vol. 42, p. 1883 (1971).
[40] K. A. Saum and D. W. Koopman, "Discharges Guided by Laser-Induced Rarefaction Channels," **Phys. Fluids,** Vol. 15, p. 2077 (1972).
[41] W. K. Pendleton and A. H. Guenther, "Investigation of a Laser Triggered Spark Gap," **Rev. Sci. Inst.,** Vol. 36, p. 1543 (1965).
[42] A. H. Guenther and J. R. Bettis, "Laser Triggered Megavolt Switching," **J. Quant. Elec.,** Vol. QE-3, p. 581 (1967).
[43] A. H. Guenther and R. N. McKnight, "A Laser Triggered 50 pps High Voltage Switch with Nanosecond Jitter," **Proc. IEEE** Vol. 55, p. 1504 (1967).
[44] A. G. Akmanov, L. A. Rivlin and V. S. Shildyaev, "Optically Initiated Directed Electric Breakdown in Air," **JETP Lett.,** Vol. 8, p. 258 (1968).
[45] V. I. Vladimirov, G. M. Malyshev, G. T. Razdobarin and V. V. Semenov, 'Investigation of an Electric Discharge Across a Laser Spark," **Sov. Phys. Tech. Phys.,** Vol. 14, p. 677 (1969).
[46] S. H. Khan and D. Walsh, "Effect of Various Gases on Formative Times of Laser-Triggered Spark Gaps," **Electronics Letters,** Vol. 6, p. 551 (1970).
[47] R. C. Klewe, M. B. C. Quigley and B. A. Tozer, "Space-Charge Injection. A New Technique for Studying Nonuniform Field Breakdown Phenomena," **Appl. Phys. Lett.,** Vol. 15, p. 155 (1969).
[48] K. H. Schmitter, "Funkenstrecker mit Optischer Triggerung," **Laser und angew. Strahltech.** No. 3, p. 9 (1970).
[49] M. Pillsticker, "Effects of Optical Components on the Triggering of Spark Gas by a Laser Beam," (in German), Inst. fur. Plasmaphys., Garching. Report IPP 4/102 (1972); "Laser Triggered High-Voltage Spark Gaps," Int. Symp. uber Hochspannungstechnik Proc., pp. 619, 626, Munchen, March 9-14 (1972).
[50] R. J. De Whurst, G. J. Pert and S. A. Ramsden, "Picosecond Triggering of a Laser-Triggered Spark Gap," **J. Phys. D, Appl. Phys.,** Vol. 5, p. 97 (1972).
[51] S. A. Ramsden and W. E. R Davies "Radiation Scattered from the Plasma Produced by a Focused Ruby Laser Beam," **Phys. Rev. Lett.,** Vol. 13, p. 227 (1964).
[52] S. A. Ramsden and P. Savic, "A Radiative Detonation Model for the Development of a Laser Induced Spark in Air," **Nature,** Vol. 203, p. 1217 (1964).
[53] R. G. Tomlinson, "Scattering and Beam Trapping in Laser Produced Plasmas in Gases," **J. Quant. Elec.,** Vol. QE-5, p 591 (1969).
[54] S. L. Mandelshtam, P. P. Pashinin, A. V. Prokhindeev, A. M. Prokhorov, and N. K Sukhodrev, "Study of the Spark Produced in Air by Focused Laser Radiation," **Sov. Phys. JETP,** Vol. 20, p. 1344 (1965).
[55] J. W. Daiber and H. M. Thompson, "Laser Driven Detonation Waves in Gases," **Phys. Fluids,** Vol. 10, p. 1162 (1967).
[56] A. B. Iznatov, I .I. Komissarova, G. V. Ostrovskaya and L. L. Shapiro, 'Holographic Studies of a Laser Spark. III Spark in Hydrogen and Helium " **Sov. Phys. Tech. Phys.,** Vol. 16, p. 550 (1971).
[57] B. Ahlborn and J. D. Strachan, "Dynamics of Step Heat Waves in Gases and Plasmas," **Can. J. Phys.,** Vol. 51, p. 1416 (1973).
[58] B. Ahlborn, "Decaying Laser Sparks," **Phys. Lett.,** Vol. 40A p. 289 (1972).
[59] R. V. Ambartsumyan, et al., "Heating of Matter by Focused Laser Radiation," **Sov. Phys. JETP,** Vol. 21, p. 1061 (1965).
[60] A. J. Alcock, C. De Michelis, K. Hamal and B. A. Tozer, "Expansion Mechanism in a Laser Produced Spark," **Phys. Rev. Lett.,** Vol. 20, p. 1095 (1968).
[61] V. V. Krobkin, et al., "Investigation of the Air Spark Produced by Focused Laser Radiation, III," **Sov. Phys. JETP,** Vol. 26 p. 79 (1968).
[62] Ya. B. Zeldovich and Yu. P. Raizer, "Physics of Shock Waves and High-Temperature Hydrodynamic Phenomena," **Academic Press, N. Y.,** Vol. 1, pp. 93-99 (1967).
[63] R. B. Hall, Laser Production of Blast Waves in Low Pressure Gases," **J. Appl. Phys.,** Vol. 40, p. 1941 (1969).

[64] K. Hohla, K. Büchl, R. Wienecke and S. Witkowski, "Energiebestimmung der Stoswelle eines Laserinduzierten Gasdurchbruchs," **Zeits. fur Naturf.**, Vol. 24a, p. 1244 (1969).
[65] J. H. Lee and R. Knystautas, "Laser Spark Ignition of Chemically Reactive Gases," **AIAA J.**, Vol. 7, p. 312 (1969).
[66] N. R. Isenor and M. C. Richardson, "Dissociation and Breakdown of Molecular Gases by Pulsed CO_2 Laser Radiation," **Appl. Phys. Lett.**, Vol. 18, p. 224 (1971).
[67] E. V. George, G. Bekefi and B. Yaakobi, "Structure of the Plasma Fireball Produced by a CO_2 Laser," **Phys. Fluids**, Vol. 14, p. 2708 (1971).
[68] M. Gravel, W. J. Robertson, A. J. Alcock, K. Büchl and M. C. Richardson, "Forward Going Filament in Sparks Induced by 10.6 μ Laser Radiation," **Appl. Phys. Lett.**, Vol. 18, p. 75 (1971).
[69] A. A. Offenberger and N. H. Burnett, "CO_2 Laser-Induced Gas Breakdown in Hydrogen," **J. Appl. Phys.**, Vol. 43, p. 4977 (1972).
[70] R. W. MacPherson and M. Gravel, "Sequential Dielectric Breakdown of Air by the Focused Radiation from a Mode Locked CO_2 TEA Laser," **Optics Comm.**, Vol. 4, p. 160 (1971).
[71] C. C. Wang and L. I. Davis Jr., "New Observations of Dielectric Breakdown in Air Induced by a Focused Nd Glass Laser with Various Pulse Widths," **Phys. Rev. Lett.**, Vol. 26, p. 822 (1971).

An Introduction to the Science and Technology of Liquid Crystals

E. B. Priestley and Peter J. Wojtowicz

RCA Laboratories, Princeton, N. J.

The liquid crystalline state of matter was discovered in 1888 by the Austrian botanist F. Reinitzer and named in 1889 by the German physicist O. Lehmann. Although sometimes considered laboratory curiosities, liquid crystals are quite common; it is estimated that about one of every 200 organic materials exhibits liquid crystalline behavior. Scientific interest in these mesogenic materials grew steadily from their discovery by Reinitzer until about 1930, and then began to wane. In the early 1960's renewed interest developed in liquid crystalline phases and at present there is a strong resurgence in all aspects of liquid-crystal research. This renewed interest occurred, in part, because liquid crystals represent interesting systems in which important phase transitions and critical phenomena can be studied. The major impetus, however, is undoubtedly the wide variety of applications in which liquid crystals have been found useful. Early applications of liquid crystals utilized the optical properties of cholesterics for temperature and pressure sensing. From an applications standpoint, current interest centers principally around the use of nematic, cholesteric, and smectic liquid crystals in a variety of display, optical, and storage devices.

At present, the liquid-crystal activity at the RCA Laboratories is quite extensive, ranging from basic research to device engineering.

Some time ago, therefore, a weekly study seminar on the subject of liquid crystals was instituted. It was our original intention that this seminar would stimulate increased interaction among individuals from different disciplines who share a common interest in liquid crystals. The resulting series of lectures are being published in the *RCA Review* beginning with this issue. We believe these lectures will serve as a useful primer in both the science and technology of liquid crystals for those using or contemplating the use of liquid crystals in practical devices. The series is intended to be a tutorial introduction to the subject and, as such, is not meant to be a review of the field of liquid crystals. Thus, no attempt has been made to include exhaustive compilations of literature references.

Included in this issue are introductions to the basic physics and chemistry of liquid crystals, introductions to the molecular theory of nematics, and a discussion of the experimental determination of the degree of order in nematics. Subsequent lectures, which will appear in future issues, will focus on the phenomenological theories of liquid crystals; their optical, electrical, and electro-optic properties; and the applications of liquid crystals in devices.

Liquid Crystal Mesophases

E. B. Priestley

RCA Laboratories, Princeton, N. J. 08540

Abstract—The concept of a mesophase is discussed and liquid crystals are shown to be ordered fluid mesophases. Thermotropic and lyotropic liquid crystals are differentiated. Particular attention is given to the nature of the molecular ordering in the various liquid-crystal mesophases. Polymorphism is defined and several examples are considered. Finally, some of the consequences of simultaneous liquid-like and solid-like behavior in a single phase are discussed qualitatively.

1. Mesophases

Everyday experience has led to universal familiarity with substances that undergo a single transition from the solid to the isotropic liquid phase. The melting of ice at 0°C to form liquid water is perhaps the most common such phase transition. There are, however, many organic materials that exhibit more than a single transition in passing from solid to liquid, thereby necessitating the existence of one or more intermediate phases. It is not surprising that the molecular ordering in these intermediate phases, known as "mesophases", lies between that of a solid and that of an isotropic liquid. The partial ordering of the molecules in a given mesophase may be either translational or rotational, or both. Clearly, translational order can be realized regardless of molecular shape, whereas rotational order has

meaning only when the constituent molecules are nonspherical (elongated). Thus, there is good reason to expect molecular structure to be an important factor in determining the kind and extent of ordering in any particular mesophase.

Two basically different types of mesophases have been observed. First, there are those that retain a 3-dimensional crystal lattice, but are characterized by substantial rotational disorder (i.e. disordered crystal mesophases), and second, there are those with no lattice, which are therefore fluid, but nevertheless exhibit considerable rotational order (i.e., ordered fluid mesophases). Molecular structure *is* in fact important and, generally speaking, molecules comprising one of these two types of mesophase are distinctly different in shape from molecules comprising the other. Indeed, with the possible exception of some polymorphous smectic materials, there are no known substances that show both disordered crystal and ordered fluid mesophases.

1.1 Disordered Crystal Mesophases

Disordered crystal mesophases are known as "plastic crystals".[1] In most cases plastic crystals are composed of "globular" (i.e. essentially spherical) molecules, for which the barriers to rotation are small relative to the lattice energy. As the temperature of such a material is raised, a point is reached at which the molecules become energetic enough to overcome these rotational energy barriers, but not sufficiently energetic to break up the lattice. The result is a phase in which the molecules are translationally well ordered but rotationally disordered, i.e., a disordered, or plastic crystal. Further increase in the temperature will result eventually in the molecules becoming energetic enough to destroy the lattice, at which point a transition to the isotropic liquid occurs. Perhaps the most striking property of plastic crystal mesophases is the ease with which they may be deformed under stress. It is this softness or "plasticity" that gives these mesophases their name.

A detailed discussion of plastic crystals is outside the scope of this lecture. However, those interested in pursuing the subject further are directed to Ref. [1] which provides an excellent elementary review of the properties of plastic crystals.

1.2 Ordered Fluid Mesophases

Ordered fluid mesophases are commonly called "liquid crystals"[2-6] and are most often composed of elongated molecules. In these mesophases, the molecules show some degree of rotational order (and in some cases

partial translational order as well) even though the crystal lattice has been destroyed. Lack of a lattice requires that these mesophases be fluid; they are, however, *ordered* fluid phases. It is this simultaneous possession of liquid-like (fluidity) and solid-like (molecular order) character in a single phase that makes liquid crystals unique and gives rise to so many interesting properties.

In what follows, the various ordered fluid mesophases are described, with particular attention being given to the nature of the molecular ordering in each case. Also, some of the consequences of simultaneous liquid-like and solid-like behavior in a single phase are discussed qualitatively. Later lectures will deal at length with many subjects we can consider only briefly here.

2. Types of Liquid Crystals

Two types of liquid crystal mesophases must be differentiated, viz. thermotropic and lyotropic. Thermotropic liquid crystals are of interest both from the standpoint of basic research and also for applications in electro-optic displays, temperature and pressure sensors, etc. Lyotropic liquid crystals, on the other hand, are of great interest biologically and appear to play an important role in living systems.

2.1 Thermotropic Liquid Crystals

The term "thermotropic" arises because transitions involving these mesophases are most naturally effected by changing temperature. Materials showing thermotropic liquid crystal phases are usually organic substances with molecular structures typified by those of cholesteryl nonanoate and N-(p-methoxybenzylidene)-p'-n-butylaniline (MBBA) shown in Fig. 1. Axial ratios of 4-8 and molecular weights of 200-500 gm/mol are typical for thermotropic liquid crystal mesogens. In this type of liquid crystal, every molecule participates on an equal basis in the long range ordering.

2.2 Lyotropic Liquid Crystals

Solutions of rod-like entities in a normally isotropic solvent often form liquid-crystal phases for sufficiently high solute concentration. These anisotropic solution mesophases are called "lyotropic liquid crystals".[7-9] Although the rod-like entities are usually quite large compared with typical thermotropic liquid-crystal mesogens, their axial ratios are seldom greater than ~15. Deoxyribonucleic acid (DNA), certain viruses (e.g., tobacco mosaic virus (TMV)), and many synthetic poly-

peptides all form lyotropic mesophases when dissolved in an appropriate solvent (usually water) in suitable concentration. The conformation of most of these materials is quite temperature sensitive, i.e. the rods themselves are rather unstable with respect to temperature changes. This essentially eliminates the possibility of thermally inducing phase transitions involving lyotropic mesophases. A more natural parameter which can be varied to produce such transitions is the solute concentration. The principal interaction producing long range order in lyotropic liquid crystals is the solute–solute interaction; solute–solvent interactions are of secondary importance. To a good approximation, then, only the rod-like entities (solute) participate in the long range ordering.

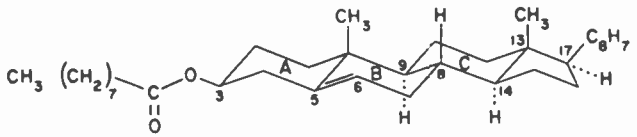

CHOLESTERYL NONANOATE

(a)

N-(P-METHOXY BENZYLIDENE)-P′-BUTYLANILINE (MBBA)

(b)

Fig. 1—Examples of molecular structures that give rise to thermotropic mesophases.

3. Classification According to Molecular Order

With the distinction between thermotropic and lyotropic mesophases in mind, we proceed to the classification of these mesophases using a scheme based primarily upon their symmetry. This scheme, first proposed by Friedel in 1922,[10] distinguishes three major classes—the nematic, the cholesteric, and the smectic.

3.1 Nematic Order

The molecular order characteristic of nematic liquid crystals is shown

schematically in Fig. 2. Two features are immediately apparent from the figure:

(1) There is long range orientational order, i.e., the molecules tend to align parallel to each other.

(2) The nematic phase is fluid, i.e., there is no long range correlation of the molecular center of mass positions.

In the state of thermal equilibrium the nematic phase has symmetry ∞/mm and is therefore uniaxial. The direction of the principal axis $\hat{n}$ (the director) is arbitrary in space.

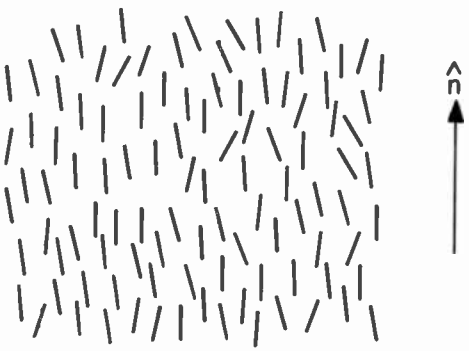

Fig. 2—Schematic representation of nematic order.

3.2 Chlosteric Order

Fig. 3 shows the equilibrium structure of the cholesteric phase. As in the nematic phase, lack of long range translational order imparts fluidity to the cholesteric phase. On a local scale, it is evident that cholesteric and nematic ordering are very similar. However, on a larger scale the cholesteric director $\hat{n}$ follows a helix of the form

$$n_x = \cos(q_o z + \phi)$$
$$n_y = \sin(q_o z + \phi)$$
$$n_z = 0$$

where both the direction of the helix axis z in space and the magnitude of the phase angle ϕ are arbitrary. Thus the structure of a cholesteric liquid crystal is periodic with a spatial period given by

$$L = \frac{\pi}{|q_o|}.$$

The sign of q_o distinguishes between left and right helicies and its magnitude determines the spatial period. When L is comparable to optical wavelengths, the periodicity results in strong Bragg scattering of light. If the wavelength of the scattered light happens to be in the visible region of the spectrum, the cholesteric phase will appear brightly colored.

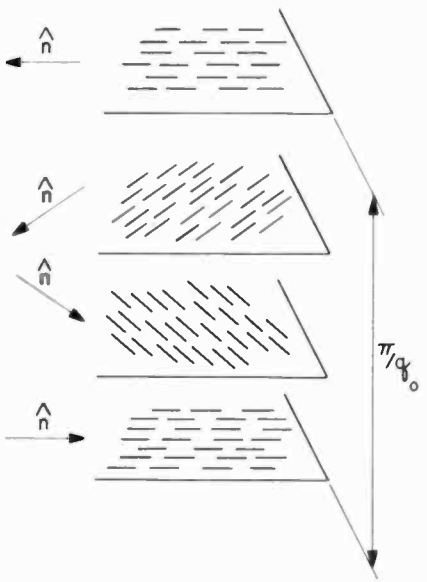

Fig. 3—Schematic representation of cholesteric order.

It is interesting to note that a nematic liquid crystal is really nothing more than a cholesteric with $q_o = 0$ (infinite pitch). In fact, the two are subclasses of the same family, the distinction being whether the equilibrium value of q_o is identically zero, or finite. If the constituent molecules are *optically inactive*, i.e., are superimposable on their mirror image, then the mesophase will be nematic. If, on the other hand, the constituent molecules are *optically active*, i.e., are not superimposable on their mirror image, then the mesophase will be cholesteric (except if the molecule and its mirror image are present in precisely equal amounts, i.e. a "racemic" mixture, in which case the mesophase will again be nematic).

Finally, a comment on nomenclature is in order. Cholesteric liquid

crystals get their name historically from the fact that the first materials that were observed to exhibit the characteristic helical structure were esters of cholesterol. It would be useful to continue identifying as "cholesteric" those mesophases whose constituent molecules are derivatives of cholesterol, and to use the term "chiral nematic" to identify mesophases formed by optically active, non-steroidal molecules.

3.3 Smectic Order

As many as eight smectic phases have been tentatively identified; however, except for three that have been reasonably well characterized, considerable uncertainty still exists about the exact nature of the molecular ordering in these phases.

We will discuss only the three best understood smectic phases, the smectic A, C, and B phases. All three appear to have one common feature, viz. one degree of translational ordering, resulting in a layered structure. As a consequence of this partial translational ordering, the smectic phases are much more viscous than either the nematic or cholesteric phase.

Smectic A Order

Within the layers of a smectic A mesophase the molecules are aligned parallel to the layer normal and are uncorrelated with respect to center of mass position, except over very short distances. Thus, the layers are individually fluid, with a substantial probability for inter-layer diffusion as well. The layer thickness, determined from x-ray scattering data, is essentially identical to the full molecular length. At thermal equilibrium the smectic A phase is optically uniaxial due to the infinite-fold rotational symmetry about an axis parallel to the layer normal. A schematic representation of smectic A order is shown in Fig. 4(a).

Smectic C Order

Smectic C order is depicted in Fig. 4(b). X-ray scattering data from several smectic C phases indicates a layer thickness significantly less than the molecular length. This has been interpreted as evidence for a uniform tilting of the molecular axes with respect to the layer normal. The fact that the smectic C phase is optically biaxial is further evidence in support of a tilt angle. Tilt angles of up to 45° have been

observed and in some materials the tilt angle has been found to be temperature dependent. As in the smectic A phase, the layers are individually fluid and inter-layer diffusion can occur, although most likely with somewhat lower probability.

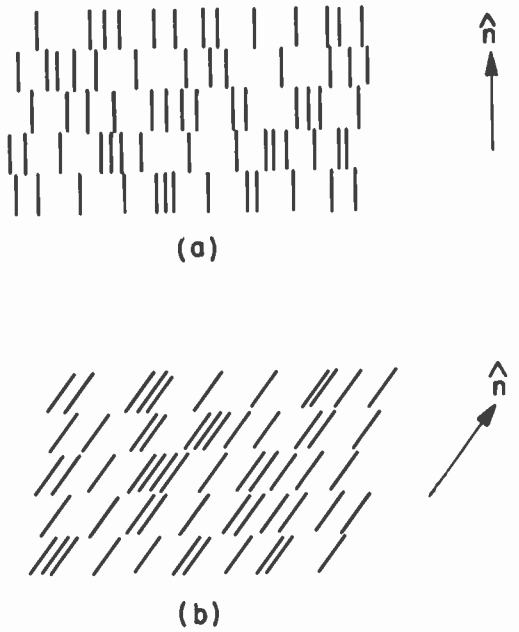

Fig. 4—Schematic representation of two types of smectic order: (a) smectic A order; (b) smectic C order.

Smectic B Order

In addition to the layered structure, x-ray scattering data indicate ordering of the constituent molecules *within* the layers of the smectic B phase. Hence, the layers are no longer fluid, in contrast to the smectic A and C phases. However, the mechanical properties of the smectic B phase are quite different from those that would be expected for a material having full 3-dimensional order; thus, we are forced to conclude that the ordering, whatever its detailed nature, cannot be of the sort familiar in solids. It has been suggested that the smectic B phase may in fact be a plastic crystal.[11] If so, this would be very interesting as it would provide the first opportunity to investigate both disordered-crystal and ordered-fluid mesophases in a single material

(for any polymorphous smectic substance having a smectic B phase). This model is not the only one possible for the smectic B phase, however. It could also be that this phase is composed of a collection of 2-dimensional solid layers coupled by very weak forces, such that the layers could slip over one another quite easily.[11] Although, in principle, these two models are experimentally distinguishable, there are no data that differentiate between them at present. Smectic B phases can be either biaxial or uniaxial depending upon whether or not there is a finite tilt angle of the sort discussed above.

4. Polymorphism in Thermotropic Liquid Crystals

Many thermotropic materials have been observed to pass through more than one mesophase between the solid and isotropic liquid phases. Such materials are said to be "polymorphous". One can predict the order of stability of these mesophases on a scale of increasing temperature simply by utilizing the fact that raising the temperature of any material results in progressive destruction of molecular order. Thus, the more ordered the mesophase, the closer in temperature it lies to the solid phase. From the description of the various types of order given in Sec. 3, we can immediately draw the following conclusions:

(1) For a material having nematic and smectic trimorphous phases, the order of mesophase stability with increasing temperature will be
solid → smectic B → smectic C → smectic A → nematic → isotropic
This order of stability is in complete agreement with experimental observation.

(2) For a material having nematic and/or smectic phases, but not all those listed in (1), the order of stability can be obtained from that shown in (1) by simply deleting those phases not present. This is also confirmed experimentally.

(3) For materials having both cholesteric and smectic mesophases, the order is identical to that shown in (1) except the word "nematic" is replaced by "cholesteric". The following have been experimentally observed:

(a) solid → cholesteric → isotropic

(b) solid → smectic A → cholesteric → isotropic.

Finally, we note that there are no known examples of polymorphism involving both nematic and cholesteric mesophases (recall the dis-

cussion of molecular symmetry in Sec. 3.2). Of course, in the presence of an external electric or magnetic field, a cholesteric liquid crystal can be forced into a nematic structure. Such field induced distortions have been studied extensively.

5. Molecular Structure of Thermotropic Mesogens

At present there is no way of predicting *with certainty* whether or not a given molecule will exhibit liquid-crystal mesophases. However, the presence of common structural features in the majority of thermotropic liquid-crystal mesogens makes possible certain generalizations regarding the types of molecules most likely to show liquid-crystalline behavior. The two structural features that appear essential are (1) the constituent molecules must be elongated and (2) they must be rigid. It should be borne in mind that these are *only* generalizations, and exceptions do exist.

We have already encountered one group of structurally related compounds that often form liquid-crystal phases, viz. the substituted cholesterols. It is evident from Fig. 1(a) that these molecules are elongated and quite rigid, thereby satisfying the two criteria above. As mentioned earlier, all mesophases produced by molecules of this type have finite pitch due to the optical activity of the parent cholesterol molecule.

As a second group, we consider molecules whose structures can be represented schematically as

with $n = 0$, 1, or 2. Many of these molecules exhibit nematic and smectic mesophases and, if optically active, may give rise to chiral nematic mesophases. It is apparent even from this crude representation that the requirement of elongated molecules is satisfied by this structure. The need for rigidity is satisfied, in general, by restricting the linkage groups to those containing multiple bonds. Fig. 5 shows three nematogenic molecules that serve to illustrate the structure for $n = 0$, 1, and 2, respectively. In the p-pentyl-p′-cyanobiphenyl (PCB) molecule, the biphenyl is considered as a single aromatic group. Thus $n = 0$, there are no linkage groups, and the substituents are $-C_5H_{11}$ and $-CN$. The p-azoxyanisole (PAA) molecule illustrates the case for $n = 1$. Its two phenyl aromatic groups are linked by an azoxy group

and both substituents are CH_3O-. Notice the double bond between the nitrogens of the linkage group. An example of the $n = 2$ case is provided by the 2,6-di-(p-methoxybenzylideneamino)-naphthalene molecule. The aromatic groups are phenyl, naphthyl and phenyl respectively, with two $-CH = N-$ linkage groups and two CH_3O- substituents. Again the linkage groups contain double bonds to provide the requisite rigidity. Brown *et al*[2] list many other aromatic linkage, and substituent groups that can be combined in the manner indicated to form potentially mesomorphic molecules.

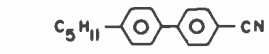

P-PENTYL-P'-CYANOBIPHENYL (PCB)

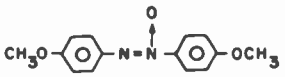

P-AZOXYANISOLE (PAA)

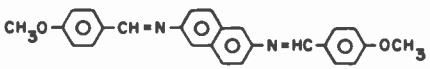

2,6-DI-(P-METHOXY BENZYLIDENEAMINO)-NAPHTHALENE

Fig. 5—Examples of themotropic nematogens.

A word of caution is in order at this point. This purely "mechanical" approach to "organic synthesis" is not to be taken too seriously. It has many obvious shortcomings, not the least of which is its total disregard for the laws of chemical combination. In spite of this, one can very quickly write down a great many structures that do not violate any chemical principles and that have a good chance of showing liquid crystal mesophases. However, one should not be at all surprised by the appearance of the occasional "dud".

Finally, there are other classes of materials, such as the substituted monocarboxylic acids, that also form liquid-crystal mesophases. However, they represent relatively few of the known thermotropic meso-

gens. For more details concerning the relationship of molecular structure to liquid crystallinity and for a discussion of these other classes of mesomorphic materials, the reader is referred to the following lecture[13] and references therein.

6. Properties of Ordered Fluid Mesophases

The combination of molecular order and fluidity in a single phase results in several remarkable properties unique to liquid crystals. By now, it is quite evident that the constituent molecules of liquid crystal mesophases are structurally very anisotropic. Because of this shape anisotropy, all the molecular response functions, such as the electronic polarizability, are anisotropic. The long range order in the liquid-crystal phases prevents this molecular anisotropy from being completely averaged to zero, so that all the *macroscopic* response functions of the bulk material, such as the dielectric constant, are anisotropic as well. We have, therefore, a flexible fluid medium whose response to external perturbations is anisotropic.

Consider the dielectric tensor $\epsilon_{\alpha\beta}$. In the uniaxial nematic phase (chosing the z-axis parallel to the nematic axis), $\epsilon_{\alpha\beta}$ has the form

$$\epsilon_{\alpha\beta} = \begin{pmatrix} \epsilon_\perp & 0 & 0 \\ 0 & \epsilon_\perp & 0 \\ 0 & 0 & \epsilon_\parallel \end{pmatrix}$$

with an anisotropy defined by $\Delta\epsilon = \epsilon_\parallel - \epsilon_\perp$. Here $\epsilon_\parallel$ and $\epsilon_\perp$ refer to the dielectric constant parallel and perpendicular to the nematic axis, respectively. The response of a nematic liquid crystal to an external electric field depends on both the sign and magnitude of $\Delta\epsilon$. If $\Delta\epsilon$ is positive, the lowest energy state in the presence of the field will be that in which the nematic axis lies parallel to the field. For a negative $\Delta\epsilon$, the lowest energy state will be that in which the nematic axis is perpendicular to the field. Due to the fluid nature of the phase, the field strength necessary to cause such realignment of the nematic axis is not very large. This ability to control the orientation of the nematic axis by means of weak external fields is the basis for several applications of nematic liquid crystals in optical display devices.

Cholesteric liquid crystals have also been put to practical use. In this case, it is primarily the sensitivity of the pitch to changes in temperature, pressure, etc. that are of interest. Recall that when the pitch of a cholesteric is equal to an optical wavelength, Bragg scattering occurs. It is evident that by choosing a cholesteric of appropriate pitch, changes in temperature and pressure can be monitored by means

of the accompanying color change of the material. Cholesteric liquid crystals are especially useful in applications where large-area temperature or pressure profiles must be determined.

Largely because of their high viscosity, smectic liquid crystals have not come into widespread use. While it seems unlikely they will be useful in any application where speed of response is important. they may be valuable as storage media.[13]

References:

[1] J. G. Aston, "Plastic Crystals," in **Physics and Chemistry of the Organic Solid State,** pp. 543-583, ed. by D. Fox, M. M. Labes, and A. Weissberger, Interscience Pub., N.Y., N.Y. (1963).

[2] G. H. Brown, J. W. Doane, and V. D. Neff, **A Review of the Structure and Physical Properties of Liquid Crystals,** CRC Press, Cleveland, Ohio (1971).

[3] G. Durand and J. D. Litster, "Recent Advances in Liquid Crystals," in **Annual Reviews of Materials Science,** Vol. 3, pp. 269-292, ed. by R. A. Huggins, Annual Reviews, Inc., Palo Alto, Calif. (1973).

[4] I. G. Chistyakov, "Liquid Crystals," **Sov. Phys. Usp.,** Vol. 9, p. 551 (1967).

[5] A. Saupe, "Recent Results in the Field of Liquid Crystals," **Angew. Chem. Int. Ed.** (English), Vol. 7, p. 97 (1968).

[6] G. W. Gray, **Molecular Structure and the Properties of Liquid Crystals,** Academic Press, N.Y., N.Y. (1962).

[7] A. S. C. Lawrence, "Lyotropic Mesomorphism in Lipid-Water Systems," **Mol. Cryst. Liquid Cryst.,** Vol. 7, p. 1 (1969).

[8] P. A. Winsor, "Binary and Multicomponent Solutions of Amphiphilic Compounds," **Chem. Rev.,** Vol. 68, p. 1 (1968).

[9] P. Ekwall, L. Mandell, and K. Fontell, "Solubilization in Micelles and Mesophases and the Transition from Normal to Reversed Structures," **Mol. Cryst. Liquid Cryst.,** Vol. 8, p. 157 (1969).

[10] G. Friedel, "Les états Mésomorphes de la Matière," **Ann. de Physique,** Vol. 18, p. 273 (1922).

[11] P. G. de Gennes, "Some Remarks on the Polymorphism of Smectics," **Mol. Cryst. Liquid Cryst.,** Vol. 21, p. 49 (1973).

[12] A. W. Levine, "Structure-Property Relationships in Thermotropic Liquid Crystals," **RCA Rev.,** Vol. 35, No. 1, p. 94 (1974).

[13] F. J. Kahn, "IR-Laser-Addressed Thermo-Optic Smectic Liquid-Crystal Storage Displays," **Appl. Phys. Lett.,** Vol. 22, p. 111 (1973).

Structure-Property Relationships in Thermotropic Organic Liquid Crystals

Aaron W. Levine

RCA Laboratories, Princeton, N. J. 08540

Abstract—The literature of organic liquid crystals is briefly surveyed from the viewpoint of the relationships between chemical structure and mesophase stability.

Introduction

The phenomenon of thermotropic liquid crystallinity has been known[1] at least since 1888. Since the early observations by Reinitzer[1,2] and Lehmann[3] of unusual melting behavior in certain organic compounds, mesogenic compounds have been both actively sought and incidentally discovered. Several relatively recent discoveries[4-9] have shown the technological utility of organic mesophases. Substantial impetus has thus been provided for the systematic investigation of the relationships between molecular structure and liquid crystallinity.

The literature of organic liquid crystals has been reviewed several times.[10-13] Reviews of those properties and compounds usable in some electro-optical devices have also appeared.[14] The intention of this paper is to present a brief summary of thermotropic mesophasic behavior in organic compounds as related to molecular structure. Recent activity in this field will be indicated in an attempt to show current trends in theory and experimentation. The cited reviews[15] and the more recent symposia reprints and abstracts are commended to the interested readers.

Organic Mesophases

Organic liquid crystals may be broadly classified as smectic, nematic, or cholesteric. These states are similar in that they exist between the fully crystallized solid state and the isotropic melt and differ in the extent of lattice order preserved in the mesophase. In the smectic phase, molecules are constrained to be parallel with their neighbors in layers, and translational motion between these layers is of low probability. In the nematic phase, molecules are able to translate in any direction with respect to their immediate neighbors but are still constained to be parallel with them along the "nematic director". When an otherwise nematogenic molecule also possesses chirality, a twisting of the nematic director occurs and the resulting structure is termed cholesteric. This phase, so named because it is frequently encountered in derivatives of cholesterol, possesses some unique properties as a result of its twist but can, within limits, be considered as a nematic phase for purposes of structural arguments. Fig. 1 illustrates these three types of ordering.

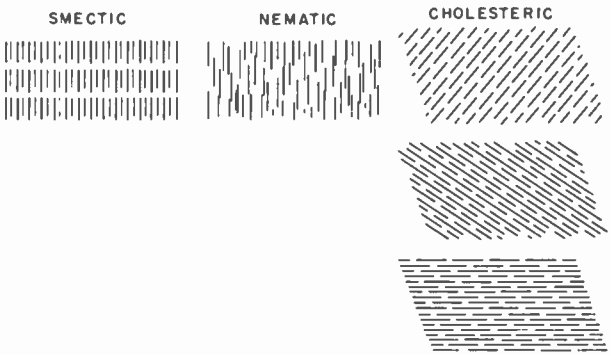

Fig. 1—Molecular ordering in various mesophases.

The molecules in Fig. 1 are illustrated as being rods. When one considers that the various mesophases are differentiated from each other, and from the isotropic liquid, by the degree of freedom of molecular motion, it is reasonable to hypothesize that intermolecular attractive forces play an important role in mesophase stability. For a given level of molecular attractions, long range ordering of molecules would clearly be encountered more often as the molecules become less spherical in shape. Thus, one would anticipate that molecular associations capable of withstanding temperatures higher than the

crystalline melting point, i.e., mesophases, would be more frequently observed for molecules of rod-like shape. In addition to a molecular shape that is considerably longer than it is wide (linear molecules), mesophasic thermal stability is favored by molecular rigidity, permanent dipoles within the molecules, and a high level of molecular polarizability. Nearly all mesogenic compounds contain multiple bonds along their long axes, aromatic nuclei, and either polar or long-chain terminal groups.

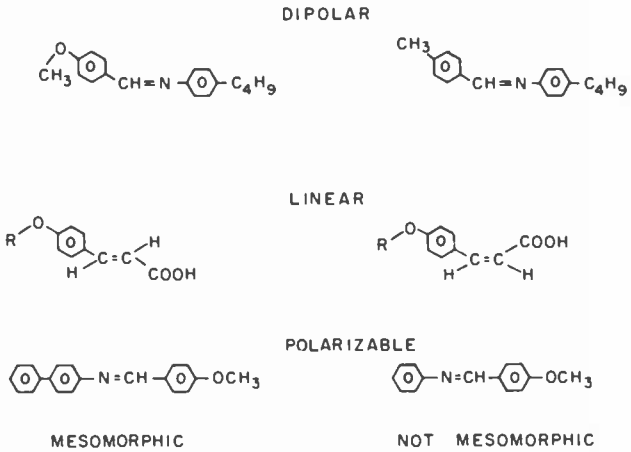

Fig. 2—Some examples of mesogenic and non-mesogenic compounds illustrating some general structural requirements.

Fig. 2 illustrates these points with some well-known mesogens and closely related compounds whose melting behavior is normal. Note that, in this paper, the term melting point is used to refer to the solid-to-mesomorphic (or isotropic) transition while the abbreviations C, S, N, Ch, and I will be used when referring to transitions involving the crystalline, smectic, nematic, cholesteric, and isotropic states, respectively. Thus, the melting point of a nematogen refers to the C-N transition while N-I will describe the nematic clearing transition.

General Structural Features of Mesogens

The vast majority of compounds exhibiting liquid crystalline properties may be regarded as possessing a central linkage and end groups (structure 1). When the central linkage is small, such as $-C{=}N-$ or $-C{\equiv}C-$, aromatic nuclei are nearly always present. Mesogens containing both carbocyclic and heterocyclic aromatic residues are known

Structure 1

and, in a sufficiently long molecule, substitution other than at *para* positions is permissible. Central groups that require no highly polarizable aromatic residues are exemplified by the Δ^5-steroid ring system and the carboxylic acid dimers. Fig. 3 shows the more common central linkages.

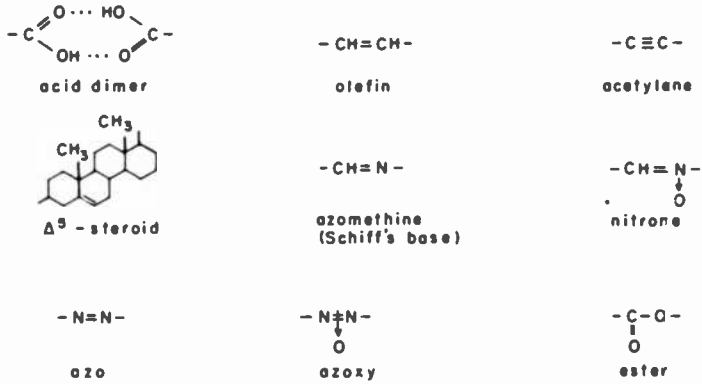

Fig. 3—Common central linkages of mesogenic compounds of Structure 1.

Terminal groups vary widely in chemical nature. Fig. 4 presents those most frequently encountered. The terminal group frequently determines which mesophase will be observed. This will be discussed in detail in the section on homologous series.

Effects of Structure on Mesophase Thermal Stability

Of the transitions observed upon melting a liquid crystalline material, the melting point is least correlated with molecular structure. This is so because the thermal stability of the solid state is principally influenced by attractive forces in the crystal lattice. Since these short-range associations are only secondarily related to molecular structure, the melting point is not usually influenced in an obvious manner by molecular structure.

The forces responsible for the mesophase, however, are primarily dipole-dipole (both permanent and induced) and dispersion forces, which, since the molecules in the mesophase or melt are free to rotate,

should be correlated with molecular structure. If the mesophase is to survive a vibrational excitation that has already exceeded the lattice energy, intermolecular polar attractions are required. In the following considerations, the mesomorphic thermal stability will be used to compare the relative efficiency of various structures in stabilizing a mesophase. It is important to understand that we are refering here to the maximum temperature at which a particular liquid crystalline

$CH_3\text{-}(CH_2)\text{-}$	ALKYL - MAY BE BRANCHED
RO-	ALKYLOXY; ALSO INTERNAL ETHERS
$RO-\overset{\overset{O}{\|}}{C}-$	CARBOALKOXY
$R-\overset{\overset{O}{\|}}{C}-O-$	ALKYLCARBOXY
$R-O-\overset{\overset{O}{\|}}{C}-O-$	ALKYLCARBONATO
F, Cl, Br, I	HALOGEN
- CN	CYANO
$-NO_2$	NITRO
R_2N-	AMINO R MAY BE H

Fig. 4—Common terminal groups of mesogenic compound of Structure 1.

behavior is observed (i.e., the S-N, S-I, N-I, S-Ch, and Ch-I transitions). Thermal stability is not to be confused with the mesomorphic range, which is the difference between the isotropic transition and melting temperatures.

For a mesophase to obtain, it is generally necessary that the terminal groups of the molecules contain permanent dipoles. For example, the N-I transition of 4-octyloxybenzoic acid[16] is some 40° higher than that of 4-nonylbenzoic acid[17] despite the essentially equivalent size of the two molecules. Similarly, the 4-alkoxy-4′-cyanobiphenyls form substantially more stable mesophases than 4-alkyl-4′-cyanobiphenyls.[18] Polarity of the termini, however, frequently gives rise to very strong intermolecular attractions. In such cases, the melting points of the compound may be raised so high that the mesophase cannot survive.

For example, the end-group polarity of 6-hydroxy-2-naphthoic acid (C—I=250°) is certainly greater than that of 6-methoxy-2-naphthoic acid (C—N=206°; N—L=219°).[19] In this case, hydrogen bonding is thought to be responsible for the nonmesogenic property of the hydroxy acid.

Frequently, more than one mesophase occurs upon heating a compound. Under these conditions, not just the presence of polar interactions but their direction is important. Thus, smectic states are stabilized by multiple dipoles acting transverse to the molecular axis (lateral attractions), while terminal attractions appear to be more important in determining nematic thermal stability. It is often found that the lower members of homologous series are purely or predominantly nematic, while in the higher members, the smectic state encroaches on, and eventually prevents observation of, the nematic. The ratio of lateral to terminal attractions increases for an homologous series due to increased dispersion forces and to increased shielding of terminal dipolar attractions of, for example, a normal alkoxy or acyloxy terminal group.

An additional difficulty in assessing the effects of end-group polarity arises when compounds with very differently sized termini are compared. Since it is usually difficult to change polarity substantially without also changing the size of the polar substituent, great care is necessary to predict mesophase stability. Thus, Brown and Shaw[11] point out that N-L temperatures generally fall if the polarity of the termini increase for a given molecular structure other than carboxylic acid dimers. Aaron, Byron, and Gray[20] found, however, that for anils of general structure 2, any substituent X provides a more thermally stable nematic state than does X=H.

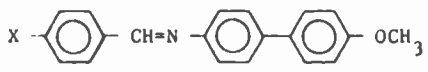

Structure 2

The polarity and polarizability of the central groups of mesogenic compounds are more clearly correlated with thermal stability. Thus, 4-alkoxy-4′-biphenyl carboxylic acids[21] form more stable mesophases than corresponding 4-alkoxybenzoic acids.[16] Similarly, esters of cholesterol form generally more thermally stable mesophases than esters of cholestanol.[22] These differ only by the presence of a double bond, as shown in Fig. 5. Again, certain conjugated unsaturated aliphatic carboxylic acids show liquid crystalline phases,[23] while normal aliphatic

acids are not mesogenic. For compounds based on central linkages that allow approximate linearity, such as azo or azomethine, mesophase thermal stability generally increases with increasing polarity or polarizability of the central linkage. Thus, N,N′-diarylazo nematogens clear some 9° higher than corresponding Schiff bases.[24] Oxidation of both classes of compounds (to azoxy and nitrone, respectively) raises the N-L points by substantial amounts.

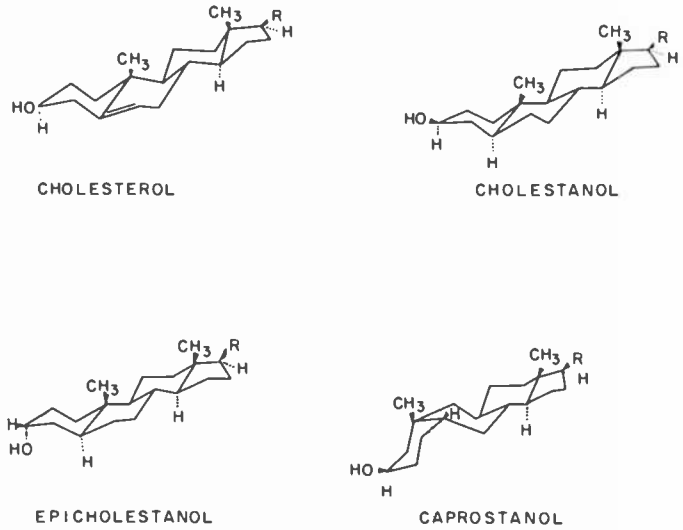

Fig. 5—Ring structures for steroid derivatives discussed in text.

When the central linkage does not provide a linear molecule, however, mesophase stability suffers. Mesophases exhibited by derivatives of phenyl benzoate, for example, are generally some 35° less stable than those of correspondingly substituted azobenzenes.[24] The effect of linearity, or at least planarity, of molecules on mesophase stability is further evidenced on comparison of *trans*-4-alkoxycinnamic acids[25] and *trans*-stilbenes[26] with their corresponding *cis* isomers, which demonstrates that severely nonlinear molecules show no mesomorphic properties. Again, derivatives of epicholestanol[22] and caprostanol (Fig. 5) are not known to be mesogenic.

The geometrical anisotropy of mesogenic compounds is certainly their most obvious common feature. Since lateral attractions play an important role in mesophase formation and stability, the effect of molecular breadth has been studied rather extensively. Generally, smectic states suffer more from molecular broadening than do nematics.

Of course, when a substituent is added that changes both molecular breadth and dipole attractions, a balancing of forces is observed, as in the 5-substituted-6-alkoxy-2-naphthoic acids[19] where broadening is partially attenuated due to molecular geometry. Even more unusual is the effect of addition of a 3-nitro group to 4-amino-4′ nitro-*p*-terphenyl which causes liquid crystallinity by changing terminal-group interactions.[27] A similar effect is known for stilbene derivatives[28] and several examples of Schiff bases exhibiting increased nematic thermal stability as a result of 2-hydroxylation have been reported.[29] By comparing the thermal stabilities of the cholesteric phase of 2-, 4-, and 2, 4-substituted benzoate esters of cholesterol, a marked effect of broadening is seen.[22, 30] This is perhaps surprising considering the size and conformations of these compounds.

As the previous discussion has indicated, despite the intuitive feeling that mesophase thermal stability should be correlated with chemical structure, the correlations are less than crystal clear. When large changes are made in the structure of a molecule in order to study polar effects, for example, other changes frequently occur that reinforce or counterbalance the particular effect under study. Even so small a change as reversing the termini of 4,4′-disubstituted benzylideneanilines causes some drastic changes in melting behavior.[24, 31]

Homologous Series

One of the more common types of recent investigation into structure-property relationships has been the synthesis of groups of molecules differing from one another only by the number of methylene groups in a terminal substituent. There appear to be two principal motivations for this type of study. First, the search for technologically useful liquid crystals is usually directed toward materials of specific nematic temperature ranges. The present lack of ability to predict such ranges, coupled with the usual availability of general syntheses for homologous series, often makes this type of investigation fruitful. To date, few, if any, pure liquid crystals have been found that are usable in display applications. Thus, all device manufacturing utilizes mixtures of mesogenic compounds. In many cases, these mixtures are based on homologous series in order to obtain eutectic mixtures or to guard against deleterious effects of material instabilities such as Schiff base trans-substitution.[32]

The second reason for studying homologous series is more fundamental. Most structure-property studies involving changes in polarity of groups, polarizability, and molecular geometry, require substantial

differences to be present among a collection of compounds. It is true, for example, that a methyl, a cyano, and a nitro terminal group impart very different polarity to a given molecule. The fact that these groups are also quite different in size and shape, however, makes interpretation of structural effects difficult. In proceeding along an homologous series, only very small changes are made at each step. It is thus hoped that more specific conclusions would be possible when the effects on mesophase behavior are correlated with molecular size and shape.

It was Gray who first recognized[10] that if the temperatures of a mesophase-to-isotropic transition were plotted against the length of the hydrocarbon chain being homologated, a smooth curve could be drawn through the points. The same seemed true for mesophase-to-mesophase transition temperatures. Of some seventy series available at that time, seven general types of curves were found that could be used to correlate all of the series. The curves differ from one another in significant ways but some general conclusions are possible as enumerated below. It should be noted that subsequently reported homologous series[33] also can be correlated by one or another of the general curves of Gray, although, again, substantial differences in detail of the fit among series that fit the same curve type are seen.

(1) The mesophase-to-isotropic transition temperature usually falls with increasing chain length. A few exceptions to this rule are known among compounds containing a biphenyl moiety which, due to substitution, is restricted from adopting a coplanar conformation. When the two aromatic nuclei are not coplanar, it is possible for the termini of one molecule to interact strongly with one of the rings of another molecule, causing additional attractions and a more thermally stable nematic state as the terminus grows in length. A similar argument has been proposed for the appearance of mesomorphism in certain Schiff bases.[34]

(2) When more than one mesophase is possible, the smectic state increases in thermal stability, at the expense of the nematic or cholesteric phase, as chain length increases. It is often seen that, while the lower homologues are purely nematic, the higher are purely smectic and the intermediate homologues exhibit both mesophases.

(3) Single smooth curves are usually not available to fit all of the points. It is most often found that transition temperatures for compounds with an odd number of carbon atoms in the chain are correlated by one smooth curve, while homologues with even numbers of carbon atoms fit another smooth curve. The transition temperature difference between adjacent odd and even members of the series may be only a few degrees or several tens of degrees depending on the

particular series and the length of the chain. The odd and even curves frequently converge at chain lengths of 8-10 carbon atoms but this is not a necessary condition. This so-called "odd-even effect" is usually justified in terms of a variation in conformation and, therefore, attractive forces as the methylene chain grows.

Summary

Organic compounds that form mesophases upon melting are characterized by being long, narrow, linear molecules. Both permanent dipoles and polarizable moieties are required. The thermal stability of the mesophase or mesophases formed depends in large measure on subtle structural, steric, and electronic effects in the central and terminal groups. Structure-property relationships have been investigated by systematic variation in polarity, polarizability, molecular size, and nature of the central linkage and termini. Some general principles have evolved but the field must not yet be considered fully understood.

References:

[1] F. Reinitzer, **Monatsh.**, Vol. 9, p. 421 (1888).

[2] F. Reinitzer, **Ann. Physik.**, Vol. 27, p. 213 (1908).

[3] O. Lehmann, **Ber.**, Vol. 41, p. 3774 (1908).

[4] G. H. Heilmeier, L. A. Zanoni, and L. A. Barton, "Dynamic Scattering: A New Electro-optic Effect in Certain Classes of Nematic Liquid Crystals," **Proc. IEEE**, Vol. 56, p. 1162 (1968).

[5] G. H. Heilmeier, J. A. Castellano, and L. A. Zanoni, **Mol. Cryst. Liq. Cryst.**, Vol. 8, p. 293 (1969).

[6] G. H. Heilmeier and J. E. Goldmacher, "A New Electric Field Controlled Reflective Optical Storage Effect in Mixed Liquid Crystal Systems," **Proc. IEEE**, Vol. 57, p. 34 (1969).

[7] G. H. Heilmeier and J. E. Goldmacher, "Electric-Field-Induced Cholesteric-Nematic Phase Change in Liquid Crystals," **J. Chem. Phys.**, Vol. 51. p. 1258 (1969).

[8] M. Schadt and W. Helfrich, "Voltage Dependent Optical Activity of a Twisted Nematic Liquid Crystal," **Appl. Phys. Lett.**, Vol. 18, p. 127 (1971).

[9] F. J. Kahn, "IR-Laser-Addressed Thermo-Optic Smectic Liquid Crystal Storage Displays," **Appl. Phys. Lett.**, Vol. 22, p. 111 (1973).

[10] G. W. Gray, **Molecular Structure and the Properties of Liquid Crystals**, Academic Press, N. Y., N. Y. (1962).

[11] G. H. Brown and W. G. Shaw, "The Mesomorphic State Liquid Crystals," **Chem. Rev.**, Vol. 57, p. 1049 (1957).

[12] A. Saupe, "Recent Results in the Field of Liquid Crystals," **Angew. Chem.** (International Ed. in English), Vol. 7, p. 97 (1968).

[13] G. H. Brown, J. W. Doane, and V. D. Neff, **A Review of the Structure and Physical Properties of Liquid Crystals**, CRC Press, Cleveland, Ohio (1971).

[14] J. A. Castellano, "Liquid Crystals for Electro-Optical Application," **RCA Rev.**, Vol. 33, p. 296 (1972); L. T. Creagh, "Nematic Liquid Crystal Materials for Displays," **Proc. IEEE**, Vol. 61, p. 814 (1973).

[15] See, e.g., R. S. Porter and J. F. Johnson, Eds., **Ordered Fluids and Liquid Crystals**, Amer. Chem. Soc., Wash., D.C. (1967); G. H. Brown, G. J. Diene, and M. M. Labes, Eds., **Liquid Crystals**, Gordon and Breach, N. Y., N. Y. (1966); J. F. Johnson and R. S. Porter, Eds., **Liquid Crystals and Ordered Fluids**, Plenum Press, N. Y., N. Y. (1970).

[16] G. W. Gray and B. Jones, "The Mesomorphic Transition Points of the p-n-Alkoxybenzoic Acids," **J. Chem. Soc.**, p. 4179, Part IV 1953.

[17] C. Weygand and R. Gabler, **Z. Phys. Chem.** (Leipzig), Vol. 46B, p. 270 (1940).

[18] G. W. Gray, K. J. Harrison, and T. W. Nash, Abstracts of the 166th Natl. Meeting of the A.C.S., Chicago, 1973, (Abstract Coll-142).

[19] G. W. Gray and B. Jones, "Mesomorphism and Chemical Constitution. Part IV," **J. Chem. Soc.**, p. 236, Part I 1955.

[20] See Ref. (10), p. 183.

[21] G. W. Gray, B. Jones, and F. Marson, "Mesomorphism and Chemical Constitution. Part VIII." **J. Chem. Soc.**, p. 393, Part I 1957.

[22] C. Wiegand, **Z. Naturforsch,** Vol. 4b, p. 249 (1949).

[23] W. Maier and K. Markau, **Z. Phys. Chem.** (Frankfort), Vol. 28, p. 190 (1961).

[24] L. K. Knaak, H. M. Rosenberg, M. P. Serve, "Estimation of Nematic-Isotropic Points of Nematic Liquid Crystals," **Mol. Cryst. Liq. Cryst.**, Vol. 17, p. 171 (1972).

[25] G. W. Gray and B. Jones, "Mesomorphism and Chemical Constitution. Part II," **J. Chem. Soc.**, p. 1467, Part II 1954.

[26] W. R. Young, A. Aviram, and R. J. Cox, **Angew. Chem.** (International Ed. in English), Vol. 10, p. 410 (1971) and references therein.

[27] P. Culling, G. W. Gray, and D. Lewis, "Mesomorphism and Polymorphism in Simple Derivatives of p-Terphenyl," **J. Chem. Soc.**, p. 2699 (1960).

[28] R. J. Cox, "Liquid Crystal Properties of Methyl Substituted Stilbenes," **Mol. Cryst. Liq. Cryst.**, Vol. 19, p. 111 (1972).

[29] I. Teucher, C. M. Paleos, and M. M. Labes, "Properties of Structurally Stabilized Anil-Type Nematic Liquid Crystals," **Mol. Cryst. Liq. Cryst.**, Vol. 11, p. 187 (1970).

[30] See Ref. (10), p. 194.

[31] H. M. Rosenberg and R. A. Champa, "The Effect on Thermal Nematic Stability of Schiff's Bases Upon Reversal of Terminal Substituents," **Mol. Cryst. Liq. Cryst.**, Vol. 11, p. 191 (1970).

[32] H. Sorkin and A. Denny, "Equilibrium Properties of Schiff-Base Liquid-Crystal Mixtures," **RCA Rev.**, Vol. 34, p. 308 (1973).

[33] See, e.g., the following papers in **Mol. Cryst. Liq. Cryst.**: J. A. Castellano, M. T. McCaffrey, and J. E. Goldmacher, "Nematic Materials Derived from p-Alkylcarbonato-p-Alkoxyphenyl Benzoates," Vol. 12, p. 345 (1971); R. D. Ennulat and A. J. Brown, "Mesomorphism of Homologous Series," Vol. 12, p. 367 (1971); G. W. Gray and K. J. Harrison, Vol. 13, p. 37 (1971); M. J. Rafuse and R. A. Soref, "Carbonate Schiff Base Nematic Liquid Crystals: Synthesis and Electro-optic Properties," Vol. 18, p. 95 (1972); M. T. McCaffrey and J. A. Castellano, "The Mesomorphic Behavior of Homologous p-Alkoxy-p'-Acyloxyazoxybenzenes," Vol. 18, p. 209 (1972); and C. S. Oh, "The Effect of Heterocyclic Nitrogen on the Mesomorphic Behavior of 4-Alkoxybenzylidene-2'-alkoxy-5'-aminopyridenes," Vol. 19, p. 95 (1972).

[34] V. I. Minkin, Y. A. Zhdanov, E. A. Madyantzeva, and Y. A. Ostroumov, "The Problem of Acoplanarity of Aromatic Azomethines," **Tetrahedron.** Vol. 23, p. 3651 (1967); also more recent calculations by H. B. Burgi and J. D. Dunitz, "Molecular Conformity of Benzylideneanilines," **Helv. Chim. Acta,** Vol. 54, p. 1255 (1971).

Introduction to the Molecular Theory of Nematic Liquid Crystals

Peter J. Wojtowicz

RCA Laboratories, Princeton, N.J. 08540

Abstract—This lecture presents a simple phenomenologically derived theory of the nematic liquid crystal phase. The problem is treated as an order-disorder phenomenon, the symmetry and structure of the nematic state being used to identify the natural order parameter. The statistical mechanics is performed in the mean field approximation. The thermodynamics of the nematic phase and its transformation to the isotropic liquid are computed. The theory is compared to previous calculations and is also found to be in qualitative agreement with experiment.

1. Introduction

In this lecture we consider the very simplest approach to the molecular theory of liquid crystals. We shall approach the theory phenomenologically, treating the problem of the existence of the nematic phase as an order-disorder phenomenon. Using the observed symmetry of the nematic phase we shall identify an order parameter and then attempt to find an expression for the orientational potential energy of a molecule in the nematic liquid in terms of this order parameter. Such an expression is easily found in the mean field approximation. Once this is accomplished, expressions for the orientational molecular distribution function are derived and the thermodynamic functions simply calculated. The character of the transformation from nematic liquid crystal to isotropic fluid is then revealed by the theory, and the nature of the fluctuations near the transition temperature can be explored.

The results of this simple theory will be compared with experiment and will be found to account qualitatively for many of the observed features of nematic liquids. Though derived in a simple phenomenological way, this theory turns out to be equivalent to the well-known pioneering theory of Maier and Saupe.[1] The relation of this theory to more rigorous or complete approaches, as well as the required generalizations of this theory will be considered in a subsequent lecture.[2]

2. Symmetry and the Order Parameter

The identification of the appropriate order parameter for nematic liquid crystals is aided by a consideration of the observed structure and symmetry of the phase. As in any liquid, the molecules in the nematic phase have no translational order; i.e., the centers of mass of the molecules are distributed at random throughout the volume of the liquid. Experiments of many varieties, however, do demonstrate that the nematic phase differs from ordinary liquids in that it is anisotropic. The symmetry, in fact, is cylindrical; that is, there exists a unique axis along which the properties of the phase display one set of values, while another set of values is exhibited in all directions perpendicular to this axis. The symmetry axis is traditionally referred to as the "director". The optical properties of nematics provide an example of how the cylindrical symmetry is manifest. For light passing parallel to the director, optical isotropy is observed, while for all directions perpendicular to the director, optical birefringence is observed. Rays polarized parallel to the director have a different index of refraction from those polarized perpendicular to the director.

Many experiments demonstrate that the anisotropy of nematics arises because of the tendency of the rod-like molecules in the fluid to align their long axis parallel to the director. This is shown schematically in Fig. 1(a). The director is denoted by the symbol $\hat{n}$; the rod-like molecules are represented by the short lines. Note that at finite temperatures, the thermal motion of the molecules prevents perfect alignment with $\hat{n}$; the orientations of the molecules are in fact distributed in angle, but with the director as the most probable, or the most populated, direction.

If we look more closely at the orientation of a single molecule with respect to the director, we find that the cylindrical symmetry of the phase requires just a single order parameter to describe the structure. In Fig. 1(b), we let the director lie along the z-axis of a fixed rectangular coordinate system. The orientation of the rod-like molecule can then be described using the three Eulerian angles shown. Because

of the cylindrical symmetry, no order in the angles ψ (rotation about the long molecular axis) or φ (rotation in the azimuthal direction) is permitted. If any angle ψ or φ was in some way preferred, a symmetry lower than cylindrical would necessarily result. Thus, we are left with the remaining angle θ as the only one for which any degree of order can exist. If any angle θ is preferred, then the resultant symmetry is indeed cylindrical; the most probable, or the prefered, angle in nematics has been shown experimentally to be $\theta = 0$, the long molecular axis parallel to $\hat{n}$. If there is no preference for a particular θ, then all such angles become equally probable and complete isotropy obtains; this is the isotropic normal liquid phase.

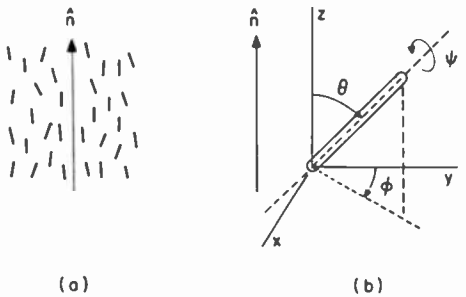

Fig. 1—(a) Schematic representation of the structure of a nematic liquid crystal. (b) The Euler angles required to describe the orientation of a molecule in a nematic liquid.

The observed symmetry and structure of the nematic liquid has enabled us to establish that a single order parameter will suffice to describe the structure of the phase. Clearly, ordering in the polar angle θ distinguishes the nematic structure from the isotropic liquid. However, θ itself is not a convenient order parameter. By analogy with ferromagnetism, one might expect that the projection of the molecules along $\hat{n}$, $\cos\theta$, would be a natural order parameter. This is not quite correct, however, since the electron spins in magnetism have a definite polarity, the heads (north poles) being distinctly different from the tails (south poles). In nematic liquids, the experiments on most materials (there are apparently some exceptions[3]) demonstrate that the heads or tails of the molecules are not distinguished in the nematic structure. That is, as many head ends point up as tail ends; these, furthermore, are randomly distributed throughout the fluid. Thus, to prevent the order parameter from describing situations in which the nematic phase becomes polarized (as in a ferromagnet

polarized with north poles up) we will use $\cos^2\theta$ rather than $\cos\theta$ to describe the structure. But now we must realize that it is not the instantaneous value of $\cos^2\theta$ for a given molecule that we need. Rather, we desire the average value of $\cos^2\theta$, $<\cos^2\theta>$, averaged over all molecules in the liquid. When all the molecules are fully aligned with $\hat{n}$, all $\theta = 0$ and $<\cos^2\theta> = 1$. On the other hand, if the molecules are randomly distributed in direction, all values of θ are equally likely and $<\cos^2\theta> = \frac{1}{3}$.

By tradition, the order parameter in any order–disorder problem is always taken such that it is unity in the perfectly ordered phase and vanishes for the completely disordered phase. Examination of the average values described above shows that the proper order parameter for the nematic liquid crystal is

$$<P_2> = \frac{1}{2}(3<\cos^2\theta> - 1). \qquad [1]$$

Clearly, $<P_2> = 1$ for the completely ordered nematic phase and $<P_2> = 0$ for the disordered isotropic phase. The symbol $<P_2>$ is used for the order parameter because we recognize the particular combination in Eq. [1] to be the second-order Legendre polynominal, $P_2(\cos\theta) = (3\cos^2\theta - 1)/2$. We will continue to use this symbol in this lecture and in the next[2] for its clarity when considering generalizations to the present theory. In the original theory[1] as well as in much of the literature, the symbol S is used to represent $<P_2>$. Values of $<P^2>$ between 0 and 1 describe degrees of ordering intermediate between completely isotropic and completely ordered. It is the task of order–disorder theory to (a) determine the temperature dependence of $<P_2>$, (b) calculate the thermodynamic and other properties in terms of $<P^2>$, and (c) demonstrate the precise way in which the transformation from finite $<P_2>$ to zero order occurs. We will now examine these questions.

3. The Molecular Potential

The stability of the nematic lequid crystal results from interactions between the constituent molecules. Without going into their nature at this time, it is clear that there must exist interactions that cause the molecules to prefer to align parallel to each other (and to the mean direction of alignment, the director). In the spirit of the mean field aproximation, we can attempt to mimic these intermolecular interactions with an effective single-molecule potential function V.

The potental V must have the correct orientation dependence; that is, it should be a minimum when the molecule is parallel to the director (parallel to the average direction of all the other molecules it interacts with) and a maximum when the molecule is perpendicular to this preferred condition. As we have seen above, the angular dependence of $-P_2(\cos\theta) = -(3\cos^2\theta - 1)/2$ is sufficient for this purpose. The potential V representing the field of intermolecular interaction forces should, furthermore, be a minimum when the phase is highly ordered and should vanish when the phase becomes disordered. Thus, V should be proportional to the degree of order, $< P_2 >$. Finally, V should contain a factor v to describe the overall strength of the intermolecular interactions; the differences between various materials will be accounted for by allowing the strength v to vary from one substance to another. Putting all the above together we arrive at mean field approximation to the orientational potential energy function of a single molecule:

$$V(\cos\theta) = -vP_2(\cos\theta) < P_2 > . \qquad [2]$$

By mean field approximation we mean that the interactions between individual molecules are represented by a potential of average force, ignoring the fact that the individual behaviors and interactions of molecules can be widely distributed about the average. This theory therefore ignores fluctuations in the short-range order (mutual alignment of two neighboring molecules); the results of the theory will then only be approximate in so far as near-neighbor fluctuation effects have been neglected in the derivation of V, as well as in subsequent calculations. The strengths and weaknesses of the mean field approximation are particularly well documented in the case of magnetism;[4] similar considerations will apply to the case of nematic liquid crystals.

4. The Orientational Distribution Function

Having derived an approximate expression for the potential energy of a single molecule in the nematic phase, we can now obtain the orientational distribution function. This function, which shall be denoted by $\rho(\cos\theta)$, describes how the molecules are distributed among the possible directions about the director; it gives the probability of finding a molecule at some prescribed angle θ from $\hat{n}$. With this function we can compute the average values of various quantities of interest pertaining to the nematic phase.

The rules of classical statistical mechanics give the orientational distribution function in terms of the potential function V as:

$$\rho(\cos\theta) = Z^{-1} \exp\left[-\beta V(\cos\theta)\right],$$

$$Z = \int_0^1 \exp\left[-\beta V(\cos\theta)\right] d(\cos\theta), \qquad [3]$$

where Z is the single-molecule partition function and $\beta = 1/kT$ (k is Boltzmann's constant and T is the temperature). The integration over all possible orientations of the molecule can be restricted to $0 \leqslant \cos\theta \leqslant 1$, since both V and ρ are even functions of $\cos\theta$. As it stands, however, Eq. [3] is still useless for the calculation of average values. The reason is that the function V (and hence ρ) contains the order parameter $< P_2 >$, and this parameter is an as yet undetermined function of the temperature. Its temperature dependence, however, can be determined as follows. $< P_2 >$ is, afterall, just the average value of the second Legendre function for a given molecule. Therefore, Eq. [3] can be used formally to express this fact:

$$< P_2 > = \int_0^1 P_2(\cos\theta)\, \rho(\cos\theta)\, d(\cos\theta). \qquad [4]$$

Expanding this equation to display its pertinent factors,

$$< P_2 > = \frac{\displaystyle\int_0^1 P_2(\cos\theta) \exp\left[\beta v P_2(\cos\theta) < P_2 >\right] d(\cos\theta)}{\displaystyle\int_0^1 \exp\left[\beta v P_2(\cos\theta) < P_2 >\right] d(\cos\theta)}. \qquad [5]$$

We now see in Eq. [5] a self-consistent equation for the determination of the temperature dependence of $< P_2 >$. The order parameter $< P_2 >$ appears on both the left and right hand sides of the equation. For every temperature T (or β) we can use a computer to obtain the value (or values) of $< P_2 >$ that satisfies the self-consistency equation. This process has been accomplished and the results are depicted in Fig. 2. $< P_2 > = 0$ is a solution at all temperatures; this is the disordered phase, the normal isotropic liquid. For temperatures T below 0.22284 v/k, two other solutions to Eq. [5] appear. The upper branch tends

to unity at absolute zero and represents the nematic phase, i.e., all molecules trying to align with the director. The lower branch tends to $-\frac{1}{2}$ at absolute zero and represents a phase in which the molecules attempt to line up perpendicular to the director without azimuthal order. This phase also has cylindrical symmetry but has not yet been seen experimentally. That it ever will is rather unlikely, since we will see later on that it is unstable with respect to the parallel-aligned nematic phase. In the temperature range where Eq. [5] provides three solutions, we require a criterion to determine which one of the three possibilities actually exists. The laws of thermodynamics provide that the observed solution, the stable phase, will be that one having the minimum free energy.

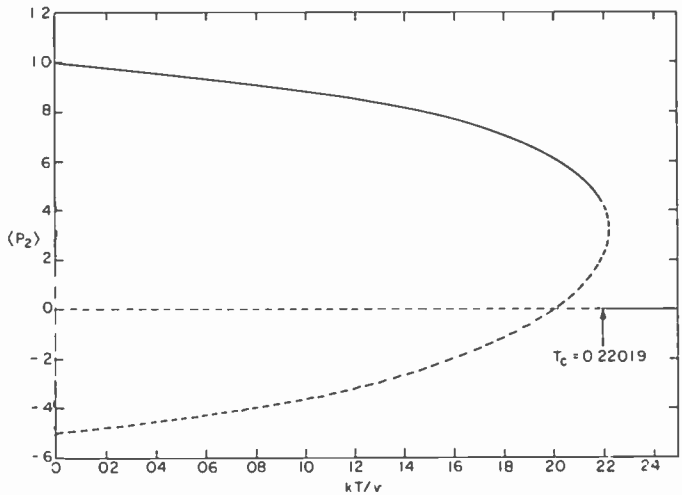

Fig. 2—Temperature dependence of the order parameter obtained from solving the self-consistency Equation, Eq. [5]. The stable equilibrium solutions are shown as the solid lines.

5. Thermodynamics of the Nematic Phase

The derivation of the free energy from the orientational distribution function is straightforward. The free energy F is given by E-TS, where E is the internal energy and S the entropy. The energy is computed by taking the average value of the potential,

$$E = \frac{1}{2} N < V > = \frac{1}{2} N \int_0^1 V(\cos\theta)\, \rho(\cos\theta)\, d(\cos\theta). \qquad [6]$$

The factor N comes in because we are dealing with a system of N molecules. The factor ½ is required to avoid counting intermolecular interactions twice (pair interactions have been approximated by a single molecule potential V). The entropy is computed by taking the average value of the logarithm of the distribution function:

$$S = -Nk < \ln\rho > = \frac{N}{T} < V > + Nk \ln Z, \qquad [7]$$

where the quantities on the extereme right hand side have been defined in Eqs. [6] and [3]. Combining Eqs. [6] and [7],

$$F = -NkT \ln Z - \frac{1}{2} N < V > . \qquad [8]$$

At first sight this equation seems unusual with the presence of the second term. The necessity for its existance can be verified immediately in two ways. If we take the derivative $(\partial F/\partial < P_2 >)_T$ and set it equal to zero we regain Eq. [5], the self consistency equation for $< P_2 >$. Thus, as required by thermodynamics, the self-consistent solutions to our problem must be those that represent the extrema of the free energy. Another verification of the correctness of Eq. [8] comes from forming the derivative $[d\beta F/d\beta]$. Again, as required by thermodynamics, Eq. [6] for the internal energy results. The reason for the appearance of the second term in Eq. [8] is the replacement of pair interactions by temperature-dependent single molecule potentials.[5]

The free energy for each of the three branches of the order parameter, Fig. 2, is computed from Eq. [8] by successive substitution of the three different values of $< P_2 >$ for each T. The free energy for the $< P_2 > = 0$ branch is constant with T and equal to zero. The free energy of the negative $< P_2 >$ branch is negative but small in magnitude. The free energy for the positive $< P_2 >$ branch is negative (with magnitude larger than that for the negative $< P_2 >$ branch) up to a temperature of 0.22019 v/k. The remainder of the positive $< P_2 >$ branch has positive values of F. Thus the stable phases to be observed are as follows: from $T = 0$ to $T = 0.22019$ v/k the nematic phase is stable. The order parameter decreases from unity to a minimum value of 0.4289 at $T = 0.22019$ v/k. For temperatures above 0.22019 v/k the isotropic phase with vanishing order parameter is stable (the stable phases are shown as the solid lines in Fig. 2). At $T_c = 0.22019$ v/k we

see that we have a first-order phase transition with the order parameter discontinuously changing from $< P_2 > = 0.4289$ to $< P_2 > = 0$. T_c is usually called a critical temperature, although in much of the liquid-crystal literature it is referred to as the clearing temperature.

Numerical values of the equilibrium order parameter $< P_2 >$ for various temperatures between zero and $T_c = 0.22019\ v/k$ have been found on the computer and are presented in Table 1 as an aid to anyone wishing to perform numerical calculations based on this or the Maier-Saupe[1] mean field theory.

Table 1—Equilibrium values of the order parameter $< P_2 >$ as a function of temperature in the nematic range:

kT/v	$< P_2 >$	kT/v	$< P_2 >$
0	1.0000	.201	.6091
.01	.9899	.202	.6032
.02	.9794	.203	.5971
.03	.9687	.204	.5908
.04	.9576	.205	.5843
.05	.9461	.206	.5776
.06	.9342	.207	.5706
.07	.9218	.208	.5634
.08	.9089	.209	.5558
.09	.8953	.210	.5479
.10	.8810	.211	.5396
.11	.8657	.212	.5309
.12	.8493	.213	.5217
.13	.8315	.214	.5120
.14	.8210	.215	.5016
.15	.7910	.216	.4904
.16	.7655	.217	.4783
.17	.7372	.218	.4649
.18	.7041	.219	.4500
.19	.6644	.220	.4327
.20	.6148	.22019	.4289

We can get a better feel for Fig. 2 if we discuss it in terms of some real temperatures. A typical nematic liquid crystal used in device applications will have its clearing point T_c at about 50°C. Then room temperature will correspond to about $T = 0.2\ v/k$. Thus, the degree of order at room temperature will be about $< P_2 > = 0.743$. From room temperature upwards, $< P_2 >$ will gradually decrease to about 0.429 at the clearing point. Degrees of order larger than 0.75 to 0.8 are rarely if ever seen. Long before such order can be accomplished by lowering the temperature, the smectic phase and/or the solid crystalline phase become more stable and spontaneously appear. The general trend of the temperature dependence of $< P_2 >$ displayed in Fig. 2 is in qualitative agreement with experimental determinations (the methods by which $< P_2 >$ is measured are dis-

cussed by E. B. Priestley in a separate lecture in this series). A more detailed comparison for several real materials is deferred to the next lecture.[2]

The first-order phase transition at T is very much like the phase transition corresponding to the melting of a solid into its liquid phase. That is, discontinuities in the volume, the internal energy (latent heat), and the entropy of the system are observed. The present theory cannot account for the small volume changes seen at T_c, since no distance (volume) dependence of the potential V was assumed. We have neglected this aspect in the present exercise, since the volume changes actually observed over the short nematic ranges of most materials are not very significant; theories that include the volume dependence are available in the literature.[1,6,7]

The latent heat of the transition from nematic to isotropic liquid can be calculated from Eq. [6] and the fact that $< P_2 >$ changes from 0.4289 to zero at T_c:

$$\Delta E(T_c) = 0.830\, T_c \text{ cal/mol.} \qquad [9]$$

The entropy of the transition can be computed from the formula $\Delta S = \Delta E/T_c$ so that

$$\Delta S(T_c) = 0.830 \text{ cal/mol°K.} \qquad [10]$$

The entropy change is a measure of the change in order at T_c and conveniently comes out of the theory as a number without any parameters to be found or adjusted. First, we note that this is a very small entropy change. Typical entropy changes for solid to liquid transitions of similar organic materials run around 25 cal/mol°K. Thus, the nematic phase at T_c contains only a very slight amount of order, certainly a lot less than a crystalline solid. The smallness of $\Delta S(T_c)$ is, of course, in keeping with the fact that the nematic phase possesses order in only a single degree of freedom, the θ angle of the individual molecules. Secondly, we can compare Eq. [10] with some experimental results; the agreement is quite satisfactory for such a simple theory. As an example,[8] the series of homologous 4,4′-d-n-alkoxyazoxybenzenes from methyl to decyl displays entropy changes in the range from 0.3 to 1.9 cal/mol°K, with most values being around 0.6 to 0.8.

The results obtained here and in the previous several sections are completely equivalent to the mean field theory derived by Maier and Saupe;[1] Eqs. [2], [3], [5], and [8] are identical to those presented in this classic series of papers. Their approach is, of course, more systematic than presented here, and the volume dependence of the

potential is treated explicitly. In the next lecture[2] we will examine a more systematic development of the theory and touch upon the volume dependence of the potential.

6. Fluctuations at T_c

All nematic to isotropic liquid phase transitions have been observed to be first order with a small volume change and a latent heat. The present simple theory, as well as more sophisticated versions in the literature, also display first-order changes in agreement with the experiments. Many articles in the literature, however, refer to this phase change as "nearly second order." Such remarks are not only misleading but are entirely incorrect. The phase transition in nematics cannot be anything but first order. The symmetry of the problem demands it. Fig. 2 shows one way of looking at this: note that the curves of $< P_2 >$ vs T for positive and negative $< P_2 >$ are not symmetrical about $< P_2 > = 0$. Because of this, the curves of positive $< P_2 >$ must intercept the abscissa with finite positive slope. In the temperature range just above where this occurs, moreover, (positive) $< P_2 >$ is double valued. Thus, there is no way that a state of finite $< P_2 >$ can transform into a state of zero $< P_2 >$ except discontinuously. In the case of ferromagnetism or antiferromagnetism, on the other hand, the curves of order parameter vs T are symmetrical about the T-axis; the positive branch is the mirror image of the negative branch. In addition, the free energies of these two branches are identical. The order parameter curves then approach the abscissa symmetrically and with infinite slope. In these cases transformations from states of finite order to ones of vanishing order can occur continuously, and second-order phase changes are allowed.

Why then did the phrase "nearly second order" arise in the literature? One reason is that the latent heat and volume changes at the nematic-isotropic transition are very small and closely approximate the vanishing changes of second-order phase transitions. The most prominent reason, however, is that many properties of the isotropic liquid display critical behavior on cooling to temperatures close to T_c (this phenomenon has been termed "pretransitional behavior" in the liquid-crystal literature). That is, certain response functions (such as the magnetically induced birefringence[9]) are seen to diverge as T_c is approached from above. The divergence of response functions at T_c is one of the hallmarks of second-order phase changes.[10] In ferromagnetism, as an example, the magnetic susceptibility diverges as $(T-T_c)^{-1.35}$ as the Curie point is approached from above. In the case of the isotropic liquid above its clearing point, the divergence never

actually occurs; the first-order phase change to the nematic phase takes place just a few degrees before. Thus the origin of the remark "nearly second order".

Now, critical behavior and the divergence of response functions are not usually seen at first-order phase transitions. No pretransitional behavior is observed in any of the properties of a liquid about to freeze into its crystalline solid. Why then is there pretransitional behavior at the nematic-isotropic transition? My own feeling is that the responsible factor is the small entropy of transition, ΔS, Eq. [10]. The divergence of response functions occur because of the presence of fluctuations. If in a disordered phase a fluctuation occurs such that a very small region of the material rearranges itself into a locally highly ordered structure, that region will have an enhanced response to some external stimulus; the corresponding response function will therefore increase in magnitude. If the fluctuations occur to a very great extent (as they do when second-order phase transitions are approached) then the response functions diverge. It is the small ΔS for nematics (compared to the ΔS of the melting/freezing transition) that permits a substantial amount of fluctuations, giving rise to pretransitional behavior.

We can make this somewhat more quantitative. According to Landau and Lifshitz,[11] the probability of a fluctuation whose change in entropy (order) is Δs is proportional to $\exp(\Delta s/k)$; here Δs is not the molar entropy of the transition, the ΔS of Eq. [10], but the entropy of ordering of a small region of the material. If this small region contains n molecules (which order to a degree normally displayed by a nematic just at T_c), then Δs can be related to ΔS, and the probability of such a fluctuation becomes proportional to

$$\exp(-n\Delta S/R), \qquad [11]$$

where R is the universal gas constant. The negative sign appears because Δs describes fluctuations from disordered to ordered states while ΔS is concerned with the transition from ordered to disordered phases. Consider now a fluctuation in which ten molecules in the isotropic phase get together and become as ordered as the nematic phase at or near its T_c. We find from Eqs. [10] and [11] that the probability of occurrence of such a fluctuation is proportional to about e^{-4}. For a fluctuation in liquid in which ten molecules get together and become as ordered as the crystalline solid, on the other hand, Eq. [11] plus the observation that $\Delta S \sim 25$ cal/mol°K give the probability as $\sim e^{-125}$. Thus we see that a significant fluctuation in the

ordering of ten molecules is $\sim e^{120}$ more probable just above the isotropic-nematic transition than it is just above a typical freezing point. This, then, is why pretransitional behavior is observed in nematics but not in the case of crystalline solids.

References:

[1] W. Maier and A. Saupe, **Z. Naturforschg.**, Vol. 14a, p. 882 (1959) and Vol. 15a, p. 287 (1960).

[2] P. J. Wojtowicz, "Generalized Mean Field Theory of Nematic Liquid Crystals," **RCA Rev.**, Vol. 35, No. 1, p. 118 (1974).

[3] R. Williams, "Optical-Rotary Power and Linear Electro-Optic Effect in Nematic Liquid Crystals of *p*-Azoxyanisole," **J. Chem. Phys.**, Vol. 50, p. 1324 (1969) and D. Meyerhofer, A. Sussman, and R. Williams, "Electro-Optic and Hydrodynamic Properties of Nematic Liquid Films with Free Surfaces," **J. Appl. Phys.**, Vol. 43, p. 3685 (1972).

[4] J. S. Smart, **Effective Field Theories of Magnetism**, W. B. Saunders Co., Philadelphia, Pa. (1966).

[5] E. R. Callen and H. B. Callen, "Anisotropic Magnetization," **J. Phys. Chem. Solids**, Vol. 16, p. 310 (1960).

[6] S. Chandrasekhar and N. V. Madhusudana, "Molecular Statical Theory of Nematic Liquid Crystals," **Acta Cryst.**, Vol. A27, p. 303 (1971).

[7] R. L. Humphries, P. G. James, and G. R. Luckhurst, **J. Chem. Soc., Faraday Trans. II**, Vol. 68, p. 1031 (1972).

[8] G. H. Brown, J. W. Doane and D. D. Neff, **A Review of the Structure and Physical Properties of Liquid Crystals**, p. 43, CRC Press, Cleveland, Ohio (1971).

[9] T. W. Stinson and J. D. Litster, "Pretransitional Phenomena in the Isotropic Phase of a Nematic Liquid Crystal," **Phys. Rev. Lett.**, Vol. 25, p. 503 (1970).

[10] H. E. Stanley, **Introduction to Phase Transitions and Critical Phenomena**, Oxford University Press, N.Y., N.Y. (1971).

[11] L. D. Landau and E. M. Lifshitz, **Statistical Physics**, p. 344, Pergamon Press Ltd., London (1958).

Generalized Mean Field Theory of Nematic Liquid Crystals

Peter J. Wojtowicz

RCA Laboratories, Princeton, N. J. 08540

Abstract—This lecture considers a systematic approach to the molecular theory of nematic liquid crystals. A completely general form of pairwise interaction potential is assumed and expanded in a series of appropriate spherical harmonics. Averages of the expanded pair potential are taken to obtain a generalized version of the single-molecule potential functions in the mean field approximation. The results are compared to previous simpler theories and to a variety of experimental observations.

1. Introduction

In the previous lecture[1] we examined a simple version of the molecular theory of nematic liquid crystals. The problem was treated as an order-disorder phenomenon with the solution based on a phenomenologically derived single-molecule orientational potential. The results of this development were found to be equivalent to the well known mean field theory of Maier and Saupe.[2]

In this lecture we will consider a more systematic approach to the molecular theory of the nematic state. In deriving the theory we will follow the development of Humphries, James, and Luckhurst.[3] We start with a completely general pairwise intermolecular interaction potential. After expanding in a series of appropriate spherical harmonics we will systematically average the pair-interaction potential to

obtain a generalized version of the single-molecule potential function in the mean field approximation. The Maier-Saupe theory[2] will result from the retention of only the first term in the generalized potential. More general versions of the theory result from the inclusion of higher-order terms. In the final sections of the lecture we will discuss the volume dependence of the interaction potential, examine the reasons why higher-order terms in the potential appear to be required, and consider the agreement between the theory and various experiments.

2. The Pair Interaction Potential

The stability of the nematic liquid-crystal phase arises from the existence of strong interactions between pairs of the constituent molecules. As in normal liquids, the potential of interactions will have attractive contributions to provide the cohesion of the fluid, and repulsive contributions which prevent the interpenetration of the molecules. In the case of the rod-like molecules of nematics, however, these interactions are highly anisotropic. That is, the forces acting between such molecules depend not only on their separation but also, and most importantly, on their mutual orientations. From the symmetry and structure of the nematic phase, we see that the rod-like molecules in fact interact in a manner that favors the parallel alignment of neighboring molecules.

A complete understanding of the nature of the intermolecular interactions is not available. The precise mathematical form of the pair potential is not known. In the absence of such detailed information, we proceed by assuming a perfectly general form for the pair potential and then deriving the theory systematically from it.

Many coordinates are required to describe the orientation dependent interaction between a pair of asymmetric molecules. Fig. 1(a) depicts the situation; in addition to the parameter r which gives the separation of the centers of gravity, we require the three Eulerian angles of each of the two molecules. Since in nematics there appears to be no ordering of the molecules about their long axes, we can eliminate the angles ψ_i by assuming the molecules to be axially symmetric. The angles θ_i and ϕ_i can then be considered as polar angles with the intermolecular vector r as the common polar axis. The intermolecular pair potential V_{12} is then a function of five coordinates:

$$V_{12} = V_{12}(r, \theta_1, \phi_1, \theta_2, \phi_2). \qquad [1]$$

Pople[4] has demonstrated a very powerful expansion for the pair potential between axially symmetric molecules:

$$V_{12} = 4\pi \sum_{L_1 L_2 m} U_{L_1 L_2 m}(r) Y_{L_1 m}(\theta_1, \phi_1) Y_{L_2 m}^*(\theta_2, \phi_2), \qquad [2]$$

where the $Y_{Lm}(\theta, \phi)$ are the usual spherical harmonics. For axially symmetric molecules and for the coordinates defined in Fig. 1(a), the potential V_{12} really depends only on r, θ_1, θ_2, and the combination $\phi_1 + \phi_2$; thus, the appearance of only a single m index in Eq. [2].

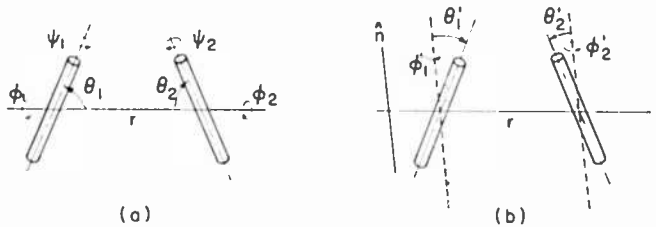

Fig. 1—The coordinate systems required to describe the interaction between two asymmetric molecules: (a) the intermolecular vector r is the mutual polar axis and (b) the director $\hat{n}$ is the polar axis for each molecule.

This expression is particularly convenient, because (a) it separates the distance and orientation dependencies of the potential and (b) the coefficients of the expansion, the $U_{L_1 L_2 m}(r)$, are found[5] to decrease rapidly with increasing L_1 and L_2. If the molecules have reflection symmetry (or if we assume that we can neglect the ordering of heads and tails of the molecules), then only terms with even L_1 and L_2 are required in Eq. [2].

3. The Mean Field Approximation

A rigorous molecular theory of a fluid system based on a pairwise interaction potential as complicated as Eq. [2] is impossibly difficult. A simple but adequate approach is to derive a theory in the mean field approximation. That is, we derive a single molecule potential that serves to orient the molecule along the symmetry axis (the director) of the nematic phase. The single-molecule potential represents (approximately) the mean field of intermolecular forces acting on a given molecule. Mean field theories have been found capable of describing the qualitative behavior of many different cooperative phenomena. The

theories are not quantitatively correct, however, since intermolecular short-range order and fluctuation effects are neglected. The properties of mean field theories in the case of magnetism have been described by Smart.[6]

In order to derive a mean field approximation to the potential, we first have to express V_{12} in terms of a polar coordinate system based on the director, $\hat{n}$, as the polar axis. The coordinate axes for the molecules 1 and 2 must be rotated from that shown in Fig. 1(a) to that shown in Fig. 1(b). The primed angles now describe the orientations of the molecules with respect to the new rotated coordinate system. Mathematically, the rotation of the coordinate axes transforms the spherical harmonics into the form

$$Y_{Lm}(\theta, \phi) = \sum_{p} D_{pm}{}^{L} Y_{Lp}(\theta', \phi'), \qquad [3]$$

where the $D_{pm}{}^{L}$ are the elements of the Wigner rotation matrices.[7] In the new coordinate system V_{12} assumes the form

$$V_{12} = 4\pi \sum_{L_1 L_2 m} \sum_{pq} U_{L_1 L_2 m}(r)\, Y_{L_1 p}(\theta_1', \phi_1')\, Y_{L_2 q}{}^{*}(\theta_2', \phi_2')\, (D_{pm}{}^{L_1})\, (D_{qm}{}^{L_2})^{*}. \qquad [4]$$

To obtain the single molecule potential V_1 in the mean field approximation, it is necessary to take three successive averages of the function V_{12}. First, we average over all orientations of the intermolecular vector r. Next, we average V_{12} over all orientations of molecule 2. Finally, we average V_{12} over all values of the intermolecular separation r. The combination of these three averaging processes provides us with the potential energy of a given single molecule as a function of its orientation with respect to the director. This potential energy, moreover, is that experienced by the molecule when subjected to the average force fields of neighboring molecules, each averaged over all its possible positions and orientations—thus the descriptive phrase, "mean field approximation".

The averaging of V_{12} over all orientations of the intermolecular vector r has an influence only on the Wigner rotation matrices:

$$< (D_{pm}{}^{L_1})\, (D_{qm}{}^{L_2})^{*} > = \delta_{L_1 L_2} \delta_{pq} (2L + 1)^{-1}, \qquad [5]$$

where $< >$ denotes the average value and the δ_{kl} are the usual Kronicker delta functions. The simple result expressed in Eq. [5] is valid

only if the distribution function for the intermolecular vectors is spherically symmetric. Since the symmetry of the nematic phase is cylindrical, this result will only be an approximation. A somewhat different expression obtains if the cylindrical symmetry is taken into account;[3] we will return to this point later. Use of Eq. [5] in taking the first average of V_{12} gives

$$< V_{12} > = 4\pi \sum_{Lpm} U_{LLm}(r)\,(2L+1)^{-1} Y_{Lp}(\theta_1', \phi_1')\, Y_{Lp}^*(\theta_2'\phi_2'). \qquad [6]$$

The averaging of $< V_{12} >$ over all orientations of molecule 2 has influence only on the spherical harmonics in θ_2', ϕ_2':

$$< Y_{Lp}^*(\theta_2', \phi_2') > = \int_0^{2\pi} \int_0^{\pi} Y_{Lp}^*(\theta_2', \phi_2')\, \rho_1(\theta_2')\, \sin\theta_2' d\theta_2' d\phi_2', \qquad [7]$$

where $\rho_1(\theta_2')$ is the orientational molecular distribution function that describes how molecule 2 is distributed among all possible directions about the director (this function has been described in the previous lecture[1] and will be considered further below). Because of the cylindrical symmetry of the nematic phase, ρ_1 can be a function only of the polar angle θ; no ϕ dependence is permitted. Then, since ρ_1 is not a function of ϕ_2', the ϕ_2' integrals vanish except for $p = 0$ and

$$< Y_{Lp}^*(\theta_2', \phi_2') > = \delta_{p0} \left(\frac{2L+1}{4\pi} \right)^{1/2} < P_L >, \qquad [8]$$

$$< P_L > = \int_0^1 P_L(\cos\theta)\, \rho_1(\cos\theta)\, d(\cos\theta), \qquad [9]$$

where the P_L are the Lth order Legendre polynomials and where Eq. [9] is the Lth generalization of $< P_2 >$, the order parameter for the nematic phase (as described in Ref. [1]). Use of Eqs. [8] and [9] in taking the average of $< V_{12} >$ yields

$$\ll V_{12} \gg = \sum_{Lm}' U_{LLm}(r)\, P_L(\cos\theta_1') < P_L > . \qquad [10]$$

The averaging of $\ll V_{12} \gg$ over all values of the intermolecular

separation r has influence only on the $U(r)$:

$$<\!\!\ll U_{LLm}(r)\gg\!\!> = \frac{1}{n}\int U_{LLm}(r)n_2(r)\,dr. \qquad [11]$$

Here $n_2(r)$ is the molecular distribution function for the separation of pairs of molecules and n is the number density of molecules in the fluid. Use of Eq. [11] in taking the average of $\ll V_{12}\gg$ gives

$$\ll V_{12}\gg = \sum_{Lm} < U_{LLm}(r) > P_L(\cos\theta_1') < P_L > . \qquad [12]$$

This is just the desired single-molecule potential in the mean field approximation; we will write it as

$$V_1(\cos\theta) = \sum_L U_L < P_L > P_L(\cos\theta), \qquad [13]$$

$$U_L = \sum_m < U_{LLm}(r) > ,$$

where we have dropped the subscript and prime on the θ. Going back to the discussion following Eq. [2], we assume no preference between the heads and tails of the molecules and restrict the L sum in Eq. [13] to even values of L. The $L = 0$ term, moreover can be discarded, since it is merely an additive constant. The first few terms of Eq. [13] are then

$$V_1(\cos\theta) = U_2 < P_2 > P_2(\cos\theta) + U_4 < P_4 > P_4(\cos\theta) + U_6 < P_6 > P_6(\cos\theta) + \cdots \qquad [14]$$

As shown in Ref. [3], if the true cylindrical symmetry of the distribution function for the orientation of the intermolecular vector were taken into account, terms proportional to

$$< U_{L_1L_2m}(r) > (P_{L_1} < P_{L_2} > + P_{L_2} < P_{L_1} >) \qquad [15]$$

would also appear in the single molecule potential V_1. If only the first term in Eq. [14] is retained, we obtain the mean field theory of Maier and Saupe[2] and the equivalent theory of the previous lecture[1] ($v = -U_2$). Since the original expansion on which V_1 is based (Eq. [2]) converges rapidly, retention of only the first term in V_1 should provide a good approximation to the theory. Comparison with experiment

shows that this is indeed the case. The necessity for including higher-order terms is quite apparent in some of the experiments, however, and we will examine this point shortly.

4. Statistical Thermodynamics

As described in the previous lecture,[1] the orientational distribution function corresponding to the single-molecule potential has the form

$$\rho_1(\cos\theta) = Z_1^{-1} \exp\left[-\beta V_1(\cos\theta)\right], \qquad [16]$$

$$Z_1 = \int_0^1 \exp\left[-\beta V_1(\cos\theta)\right] d(\cos\theta),$$

where Z_1 is the single molecule partition function and $\beta = 1/kT$ (k is Boltzmann's constant and T the temperature). The integration over all possible orientations of the molecule can be restricted to $0 \leqslant \cos\theta \leqslant 1$, since V_1 and ρ_1 are even functions of $\cos\theta$. Again, as it stands, Eq. [16] is not complete and not yet useful in computing average values. V_1 does after all contain the as yet unknown averages, $< P_L >$. The self-consistent determination of the temperature dependence of the $< P_L >$ is realized by combining their definition (Eq. [9]) with Eq. [16]:

$$< P_L > = \frac{\displaystyle\int_0^1 P_L(\cos\theta) \exp\left[-\beta V_1(\cos\theta)\right] d(\cos\theta)}{\displaystyle\int_0^1 \exp\left[-\beta V_1(\cos\theta)\right] d(\cos\theta)}. \qquad [17]$$

There is one such self-consistency equation for each term L included in the potential V_1, Eq. [13]. In each of these equations one of the $< P_L >$ appears on the left-hand side, and all the included $< P_L >$ appear in the integrals on the right-hand side. The simultaneous solution of these equations yields the temperature dependence of all the $< P_L >$ originally included in the potential V_1. In particular, the solution for $< P_2 >$ gives the temperature dependence of the tradi-

tional order parameter of the nematic phase. One of the solutions provided by the set of equations, Eq. [17], is $< P_L > = 0$, all L; this is the isotropic normal liquid. To find which of all the possible solutions is the physically observed stable solution, we must compute the free energy and determine the solution giving the minimum free energy.

The internal energy, entropy, and free energy are obtained in exactly the same way as computed in the simpler theory of the previous lecture:

$$E = \frac{1}{2} N < V_1 > = \frac{1}{2} N \sum_L U_L < P_L >^2, \qquad [18]$$

$$S = -Nk < \ln \rho_1 > = \frac{N}{T} \sum_L U_L < P_L >^2 + Nk \ln Z_1, \qquad [19]$$

$$F = -NkT \ln Z_1 - \frac{1}{2} N \sum_L U_L < P_L >^2. \qquad [20]$$

Just as in the case of the simpler theory,[1] the free energy is found to include additional terms beyond the usually expected $\ln Z_1$ term. The form is correct, however, and arises because we have approximated the action of the pair potential V_{12} by the temperature-dependent single-molecule potential V_1. Note that setting the partial derivatives $(\partial F / \partial < P_L >)_{T,\ P_{L'}}$ to zero regains the required self-consistency equations, Eq. [17]. Furthermore, testing Eqs. [18] and [20], we see that they do satisfy the required thermodynamic identity, $E = (d\beta F / d\beta)$.

5. Nature of the Parameters U_L

The main physics of the problem, the character of the intermolecular interactions, is contained in the parameters U_L of the one molecule potential V_1. In spite of their central importance in the theory, however, not all that much is known about their magnitude or volume dependence. Several attempts to estimate their properties have been made, but very little in the way of definitive results has been obtained. What is usually done in practice is to treat the U_L as simple volume-dependent functions with constants determined by fitting the theory to experimental results.

The first attempt to elucidate the nature of the intermolecular forces in nematics was performed by Maier and Saupe.[2] They did a

calculation of the London dispersion forces (induced dipole–induced dipole) expected between asymmetric molecules. Since the polarizabilities of elongated molecules are anisotropic, the interactions involving these polarizabilities must likewise be anisotropic. Indeed, Maier and Saupe found (within their approximations) an attractive interaction between pair of molecules that led to the form

$$V_1 \approx -\frac{A}{V^2} < P_2 > P_2(\cos\theta). \qquad [21]$$

Thus, U_2 is determined from these calculations to be of the form $-A/V^2$, where A is a constant to be determined from experiment and V is the mean molecular volume. The particular volume dependence should not be surprising; the potential of dispersion forces (whether between symmetric or asymmetric molecules) is expected to depend on the intermolecular separation as r^{-6}. On the average, then, this translates into the above V^{-2} dependence.

Chandrasekhar and Madhusudana[8] have also considered the calculation of the coefficients U_l required in V_1. The first contribution that these authors examined was the permanent dipole–permanent dipole forces. These were shown to vary as r^{-3} and provided a V^{-1} dependence to U_1. It was shown however, that this term vanished when the pair potential V_{12} is averaged over a spherical molecular distribution function. The authors thus discard this term and provide further arguments for its neglect based on the empirical result that permanent dipoles apparently play a minor role in providing the stability of the nematic phase. The second contribution considered was the dispersion forces based on induced dipole–induced dipole interactions and induced dipole–induced quadrupole interactions. As mentioned above, the first of these gives a V^{-2} dependent contribution, while the second provides a contribution depending on $V^{-8/3}$. The final contribution considered was the repulsive forces that arise from the mutual impenetrability of the molecules. Assuming (by analogy with the behavior of the better understood, more simple molecules) that the repulsive potential varies as r^{-12}, this mechanism provides a contribution to the U_l that varies as V^{-4}. All these contributions were then lumped together and an average volume dependence was assumed; the authors chose to allow the U_l to have a V^{-3} dependence.

Humphries, James, and Luckhurst[3] in their development of the mean field theory decided to allow each of the U_l to have the same volume dependence, $V^{-\gamma}$, where γ is a parameter to be determined by

fitting theory to experiment. The use of an arbitrary parameter γ gives great latitude in reproducing experimental results and much success can be expected. The procedure is, however, dangerous. In the first place, the use of γ in the theory provides still another adjustable parameter; with enough adjustable parameters, of course, any experimental observation can be reproduced (but without learning any physics). Second, the introduction of an arbitrary $V^{-\gamma}$ dependence can lead to abuses. There is one instance in the literature where experimental data was force fit using a value of γ equal to 10. Certainly, we know of no substantial attractive intermolecular potential that varies as strongly as r^{-30}.

Great care should be used in choosing and using various forms for the U_L in Eq. [13]. The simplest (and possibly least controversial) procedure is to assume that the U_L are simply constants independent of the volume and to restrict the fitting of theory to experiment to a narrow range of temperature near T_c. Since the volume changes are small over a short temperature interval, the approximation of constant U_L will be quite adequate and will keep the use of the theory simple and straightforward. The region near T_c, moreover, is the most interesting; it is here that $< P_2 >$ has its strongest temperature dependence.[1]

6. The Need for Higher Order Terms in V_1

As stated in Sec. 3, the retention of only the first term in Eq. [14] leads to the mean field theory of Maier and Saupe[2] and the equivalent theory of the previous lecture.[1] This version of the theory has been shown to provide a good qualitative picture of the nematic phase and its transition to the isotropic liquid. What, then, is it about the experimental facts that indicate the necessity of higher order terms in V_1?

In Fig. 2 we display (schematically) the comparison of several experiments with the mean field theory, including only the term in U_2. We use $T - T_c$ as the abscissa, so that the two materials depicted can be conveniently compared on the same graph. The dashed line is the theoretical curve computed from the mean field theory using only the term in U_2. We note that there is a striking difference in the properties of the two materials, PAA (para-azoxyanisole) and PAP (para-azoxyphenetol). We note further that the simple theory cannot account for the order parameter of either material. Fig. 2 is, in fact, clear evidence for the necessity of higher-order terms in the potential. That the two substances have different values of T_c must mean that

the interaction potentials differ by at least a multiplicative constant. However, the fact that the order parameter of PAP is everywhere larger than that of PAA cannot be explained by allowing the interactions to differ only by a multiplicative constant. Such a large difference in the values of $< P_2 >$ can only be accounted for by assuming that the potentials are in some essential way different in the two materials. This difference must be a difference in both the sign and magnitude of the higher-order terms in V_1.

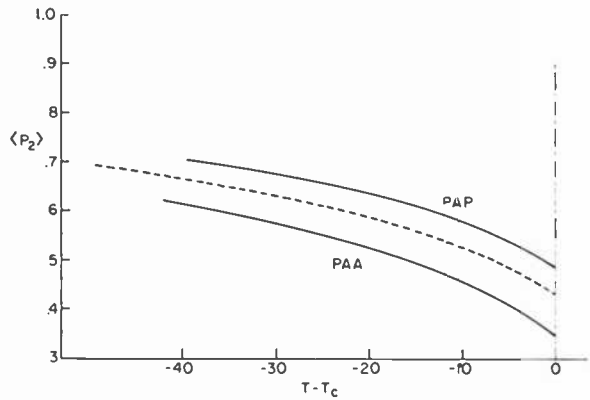

Fig. 2—Schematic representation of the temperature dependence of the order parameter for PAA and PAP. The dotted line is the result of the simple mean field theory.

The mean field theory with higher-order terms included is capable of reproducing the experimental data of Fig. 2. The addition of the term in U_4, Eq. [14], is found to be sufficient.[9] The data on PAP can be accounted for by having $U_4 \approx +0.12\ U_2$, while the data on PAA are fit by assuming $U_4 \approx -0.19\ U_2$. In the case of PAP, U_4 adds to the ordering effects of U_2 and $< P_2 >$ is raised above that predicted by the simple theory. In the case of PAA, on the other hand, U_4 decreases the ordering effects of the U_2 term and a lowered $< P_2 >$ results. Similar results on these two materials have also been reported by Chandrasekhar and Madhusudana.[8]

The most dramatic evidence that the interaction potential must be quite complicated comes from recent experiments by Jen, Clark, Pershan, and Priestley[10] on MBBA (N-(p′-methoxybenzylidene)-p-n butylaniline). Using the Raman scattering technique these authors were able to determine the temperature dependences of both $< P_2 >$ and $< P_4 >$. The experimental data are shown (with their error bars)

as the dots in Fig. 2. As is readily apparent, the value of $< P_4 >$ becomes quite small and then turns negative (!) just before the transition temperature is reached. The simple version of the mean field theory is just not capable of handling this situation; the mean field theory with U_2 only is represented by the solid lines. Note in particular that $< P_4 >$ is predicted to remain positive right up to the transition point. The addition of the term in U_4 does not help very much; the dashed lines represent the results[10] of the theory with $U_4 \approx -0.55\ U_2$. While $< P_2 >$ has been brought into agreement with experiment, $< P_4 >$, though reduced in magnitude, still remains quite positive.

The physical meaning of a negative $< P_4 >$ has been discussed by Jen et al.[10] These authors have demonstrated that a negative $< P_4 >$ implies the existence of a broad orientational distribution function $\rho_1 (\cos \theta)$, Eq. [16]. In the simple mean field theory (U_2 term only), the distribution function is sharply peaked at $\theta = 0$; that is, the probability of locating a molecule whose long axis is at an angle θ with respect to the director is extremely high for angles near zero and quite small when the angle θ becomes appreciable. In the case of MBBA, however, the probability for finite angles is almost as high as for $\theta = 0$. It therefore follows that the interaction potential V_1 required to describe the behavior of MBBA must be of a form which (at high temperatures at least) provides a very shallow minimum at $\theta = 0$ and/or subsidiary minimum at some finite angle. In attempting to reproduce the experimental results shown in Fig. 3, P. Sheng and I have tried numerous potential functions that have this feature and that are compatible with the systematic development, Eqs. [14] and [15]. In addition to terms in U_2 and U_4, Eq. [14], we have also included terms in $(< P_2 > P_4 + < P_4 > P_2)$, Eq. [15]. Though it has been possible to reduce the magnitude of $< P_4 >$ drastically, the desired behavior as depicted in Fig. 3 has not been obtained.

Our most promising attempt at describing the experiments on MBBA was realized by using the following single molecule potential:

$$V_1(\cos \theta) = U < P_2 > P_2(\cos \theta) + U' < f > f(\cos \theta),$$
$$f(\cos \theta) = P_2(\cos \theta) - 2P_4(\cos \theta) + P_6(\cos \theta). \qquad [22]$$

This potential is obtained by taking very special combinations of terms from both Eqs. [14] and [15.] This combination was purposely chosen so that the part in U' gave a strong minimum in orientational potential energy at an angle far from the director ($\theta = 52°$, in fact). Even with

this potential function (specifically engineered to give the desired result) we were unsuccessful in explaining the data on MBBA. For certain values of U'/U we did get negative values of $< P_4 >$ of the right magnitude allright; it just happened, however, that the nematic phase became unstable with respect to other more complex structures. The molecular origin of the negative $< P_4 >$ thus remains a mystery.

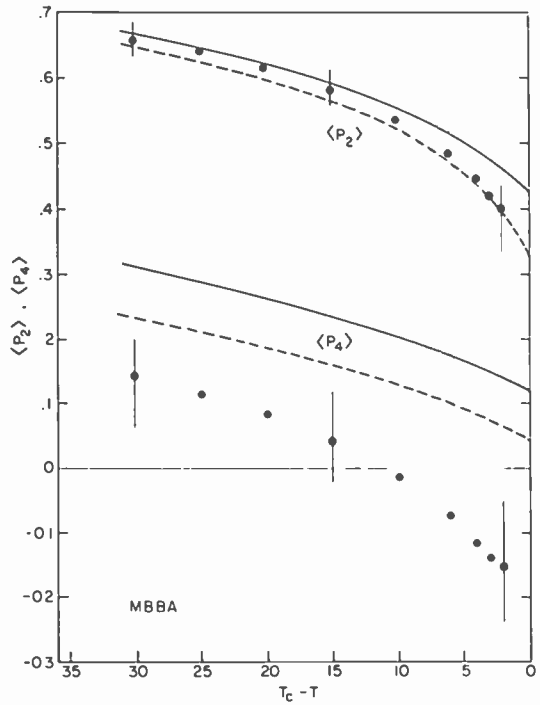

Fig. 3—Temperature dependence of the parameters $< P_2 >$ and $< P_4 >$ for the compound MBBA (data of Ref. [10]). The lines are theoretical curves described in the text.

A final comment. It may be that the source of the negative $<P_4>$ is not to be found in a complicated form of the potential V_1 but in improving the mean field theory itself. As is well known from studies of other cooperative phenomena, the mean field theory is only a first approximation and theories that attempt to include short-range order and fluctuation effects always show great improvements in reproducing the details of experiments. Accordingly P. Sheng and I[11] have derived a theory of the nematic phase based on the well known "constant coupling" theory of ferromagnetism (see Ref. [6]). Though short-

range order is explicitely included and pair-potential functions including terms through P_4 ($\cos \theta_{12}$) have been used, the temperature dependence of $< P_4 >$ for MBBA has not been realized. The explanation of the negative $< P_4 >$ in MBBA, therefore, constitutes one of the outstanding theoretical problems of the nematic liquid-crystal state.

References:

[1] P. J. Wojtowicz, "Introduction to the Molecular Theory of Nematic Liquid Crystals," **RCA Rev.**, Vol. 35, No. 1, p. 105, March 1974 (this issue).
[2] W. Maier and A. Saupe, **Z. Naturforschg.**, Vol. 14a, p 882 (1959), and Vol 15a, p. 287 (1960).
[3] R. L. Humphries, P. G. James and G. R. Luckhurst, "Molecular Field Treatment of Nematic Liquid Crystals," **J. Chem. Soc., Faraday Trans. II**, Vol. 68, p. 1031 (1972).
[4] J. A. Pople, "The Statistical Mechanics of Assemblies of Axially Symmetric Molecules. I. General Theory," **Proc. Roy. Soc.**, Vol. A221, p. 498 (1954).
[5] J. R. Sweet and W. A. Steele, "Statistical Mechanics of Linear Molecules. I. Potential Energy Functions," **J. Chem. Phys.**, Vol. 47, p. 3022 (1967).
[6] J. S. Smart, **Effective Field Theories of Magnetism**, W. B. Saunders Co., Phila., Pa. (1966).
[7] M. E. Rose, **Elementary Theory of Angular Momentum**, J. Wiley and Sons, N. Y., N. Y. (1957).
[8] S. Chandrasekhar and N. V. Madhusudana, "Molecular Statistical Theory of Nematic Liquid Crystals," **Acta Cryst.**, Vol. A27, p. 303 (1971).
[9] G. R. Luckhurst, unpublished notes.
[10] S. Jen, N. A. Clark, P. S. Pershan, and E. B. Priestley, "Raman Scattering from a Nematic Liquid Crystal: Orientational Statistics," **Phys. Rev. Lett.**, Vol. 31, No. 26, p. 1552 (1973).
[11] P. Sheng and P. J. Wojtowicz, to be published.

Hard Rod Model of the Nematic-Isotropic Phase Transition

Ping Sheng

RCA Laboratories, Princeton, N. J. 08540

Abstract—A classical gas of hard rods can exhibit a first-order transition from the isotropic phase to the anisotropic phase as the density is increased. A qualitative discussion of the physics of this phenomenon is followed by a derivation of the Onsager equations, which give a mathematical formulation of the problem when the density is low. The Onsager equations are solved in a simplified model for illustration.

Introduction

In the previous papers we have seen how an anisotropic, attractive interaction between the molecules of the form $P_2(\cos \theta_{12})$ can give rise to a first-order nematic-isotropic phase transition. The origin of the anisotropy lies in the fact that almost all the liquid-crystal molecules are elongated, rod-like, and fairly rigid (at least in the central portion of the molecule). It is clear, however, that besides the anisotropic attractive interaction there must also be an anisotropic steric interaction that is due to the impenetrability of the molecules.

It is natural to ask what effect, if any, the steric interaction might have on the nematic-isotropic phase transition. Onsager recognized that a system of hard rods, without any attractive interaction, can have a first-order transition from the isotropic phase to the anisotropic phase as the density is increased.[1-5] To see how this can come about, we note that in a gas of hard rods there are two kinds of entropy. One is the entropy due to the translational degrees of freedom, and the other is the orientational entropy. In addition, there is a coupling

between these two kinds of entropy that can be described as follows. When two hard rods lie at an angle with respect to each other, the excluded volume (the volume into which the center of mass of one molecule cannot move due to the impenetrability of the other molecule) is always larger than that when the two hard rods are parallel. This fact can easily be illustrated in two dimensions. For simplicity let us take two lines of length L. When they are perpendicular to each other, the excluded area is L^2. When they are parallel, the excluded area vanishes. This is shown in Fig. 1. It is only a short step to

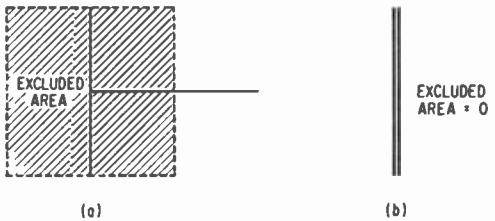

Fig. 1—Excluded area of two lines. In (a), the excluded area between two perpendicular lines is indicated by shade. In (b), the lines are parallel, and the excluded area is zero.

visualize the same situation in three dimensions where the excluded area is now replaced by excluded volume. The importance of excluded volume is that the translational entropy favors parallel alignment of the hard rods because this arrangement gives less excluded volume and, therefore, more free space for the molecules to jostle around. However, parallel alignment represents a state of low orientational entropy. Therefore, a competition exists between the tendency to maximize the translational entropy and the tendency to maximize the orientational entropy.

In the limit of zero density the tendency to maximize the orientational entropy always wins because each molecule rarely collides with another molecule, and the gain in excluded volume due to parallel alignment would only be a minimal addition to the already large volume of space within which each molecule can move about. When the density is increased, however, the excluded volume effect becomes more and more important. We know that in the limit of tight-packing density, the hard rods must be parallel. A transition between the isotropic and the anisotropic states therefore must occur at some intermediate density. But this kind of general argument cannot tell us whether the transition is smooth or abrupt. To be more precise, we will derive the Onsager equations and actually solve them in a simplified case.

2. Derivation of Onsager Equations

Consider a classical system of N hard rods in a volume V. The partition function Z, including the angular part, is[6]

$$Z(N,V,kT) = \frac{1}{N!h^{6N}} \int \cdots \int d^N p_\theta d^N p_\phi d^N p_\psi d^N \theta d^N \phi d^N \psi$$

$$\times \int \cdots \int d^{3N}x d^{3N}p \exp\left\{-\left[\sum_{i=1}^{N}\left(\frac{p_{\theta i}^2}{2I_1} + \frac{(p_{\phi i} - p_{\psi i}\cos\theta_i)^2}{2I_1 \sin^2\theta_i}\right.\right.\right.$$

$$\left.\left.\left. + \frac{p_{\psi i}^2}{2I_2} + \frac{p_{xi}^2 + p_{yi}^2 + p_{zi}^2}{2m}\right) + \sum_{i<j}^{N} v_{ij}(x,\theta,\phi)\right] /kT\right\} \qquad [1]$$

Here k is the Boltzmann constant, T is the temperature, h is Plank's constant, θ, ϕ, ψ are the usual Euler angles (following the notation used in Goldstein, *Classical Mechanics*), p_θ, p_ϕ, p_ψ are the canonical conjugate angular momenta, I_1, I_2 are the two principal moments of inertia of a rigid rod, m is the mass of the rod, v_{ij} is the interparticle steric interaction, and p_x, p_y, p_z are the linear momenta of the hard rod. The kinetic energy part of the integral can be immediately integrated. Integration over the translational momenta yields a term $(2\pi mkT)^{3N/2}$. Integration over the angular momenta gives a term

$$(2\pi I_1\sqrt{2\pi I_2})^N \prod_{i=1}^{N} \sin\theta_i$$

Since nothing in the integrand depends on ψ, this angle can also be integrated to yield $(2\pi)^N$. Grouping the constants and combining the

$$\prod_{i=1}^{N} \sin\theta_i$$

factor with $d^N\theta$ yields

$$Z(N,V,kT) = \frac{(2\pi)^N (2\pi I_1^{2/3} I_2^{1/3} kT)^{3N/2} (2\pi mkT)^{3N/2}}{N!h^{6N}}$$

$$\times \int \cdots \int d^N \cos\theta d^N\phi \int \cdots \int d^{3N}x \exp\left\{-\sum_{i<j}^{N} v_{ij}/kT\right\}$$

$$= \frac{1}{N!\eta^N\lambda^{3N}} \int \cdots \int d^N\Omega d^{3N}x \exp\left\{-\sum_{i<j}^{N} \frac{v_{ij}}{kT}\right\}, \qquad [2]$$

where $\eta = h^3/[kTI_1^{2/3}\,(2\pi I_2)^{1/3}]^{3/2}$ is a dimensionless constant ($\hbar = h/2\pi$), $\lambda = h/\sqrt{2\pi mkT}$ is the thermal wavelength, and Ω is the solid angle. The angular integrals in Eq. [2] can be approximated to arbitrary accuracy by summations in the following manner. Divide the unit sphere into K cells, each containing a solid angle $\Delta\omega$. The orientational distribution of the rods is specified by the integers N_α, which give the number of rods oriented in the direction of αth angular cell. The angular integrals can then be replaced by sum over all the possible partitions $\{N_1, N_2, \ldots N_\alpha, \ldots N_K\}$ with $N_1 + N_2 + \ldots + N_K = N$, multiplied by a factor $[N!/(N_1!N_2!\ldots N_K!)]$ for the number of times the partition $\{N_1, \ldots N_K\}$ has been counted in the angular integrals[5];

$$Z\,(N, V, kT) = \frac{1}{N!\eta^N\lambda^{3N}} \sum_{\{N_\alpha\}} \frac{N!\,(\Delta\omega)^N}{N_1! \cdots N_\alpha! \cdots N_K!}$$

$$\times \int \cdots \int d^{3N}x \exp\left[-\sum_{i<j}^{N} \frac{v_{ij}}{kT}\right] \qquad (3a)$$

$$= \sum_{\{N_\alpha\}} Z\,(\{N_\alpha\}, N, V, kT)\,, \qquad [3b]$$

where $Z\,(\{N_\alpha\}, N, V, kT) = \dfrac{(\Delta\omega)^N}{\eta^N\lambda^{3N} \prod_{\alpha=1}^{K} (N_\alpha!)} \int \cdots \int d^{3N}x \exp\left\{-\sum_{i<j}^{N} \dfrac{v_{ij}}{kT}\right\}$

Let us pick the maximum term in the summation

$$\sum_{\{N_\alpha\}} Z(\{N_\alpha\},N,V,kT) \text{ and label it } Z(\{N_\alpha\})_{\max}.$$

Since the summation can have at most N^K terms, we have the following inequality:

$$Z(\{N_\alpha\})_{\max} < Z(N, V, kT) < N^K Z\,(\{N_\alpha\})_{max}. \qquad [4]$$

Taking the logarithm and dividing through by N, we have

$$\frac{1}{N} \ln Z\,(\{N_a\})_{max} < \frac{1}{N} (\ln Z < \frac{1}{N} \ln Z\,(\{N_a\})_{max} + K \ln N). \quad [5]$$

As $N \to \infty$, the term $(\ln N)/N$ approaches zero and $(\ln Z)/N$ can be exactly replaced by $[\ln Z(\{N_a\})_{\max}]/N$. Therefore, our task can be reduced to the calculation of $Z\,(\{N_a\}, N, V, kT)$ as long as we remember to maximize the result with respect to $\{N_a\}$ afterwards.

Now $Z\,(\{N_a\}, N, V, kT)$ can be put in the following form:

$$Z\,(\{N_a\}, N, V, kT) = \frac{1}{\eta^N \lambda^{3N}} \frac{(\Delta\omega)^N}{\prod_{\alpha=1}^{K} (N_a!)} \int \cdots \int d^{3N}x \exp\left\{ - \sum_{i<j}^{N} \frac{v_{ij}}{kT} \right\}$$

$$= \frac{1}{\eta^N \lambda^{3N}} \frac{(\Delta\omega)^N}{\prod_{\alpha=1}^{K} (N_a!)} \int \cdots \int d^{3N}x \prod_{i<j}^{N} \exp\left\{ - \frac{v_{ij}}{kT} \right\}. \quad [6]$$

Define $\Phi_{ij} \equiv \exp\{-v_{ij}/(kT)\} - 1$. With v_{ij} denoting the steric repulsion, Φ_{ij} has the value zero when the two molecules are not in contact but takes the value -1 when the center of mass of one molecule enters the "excluded volume" of two hard rods. With this definition of Φ_{ij} we can rewrite the integrand as

$$\prod_{i<j}^{N} \exp\left\{ - \frac{v_{ij}}{kT} \right\} = \prod_{i<j}^{N} (1 + \Phi_{ij}) = 1 + \sum_{i<j}^{N} \Phi_{ij} + \sum_{i<j,\, l<m}^{N} \Phi_{ij}\, \Phi_{lm} + \cdots \quad [7]$$

The first term represents the behavior of the ideal gas, and the second term is the first-order correction to this behavior due to steric repulsion between the molecules. If we limit ourselves to densities that are not too high, we can neglect higher-order terms, which represent the effects of excluded volume between more than two molecules. With this crucial approximation, we have

$$Z\,(\{N_a\}, N, V, kT) \simeq \frac{(\Delta\omega)^N}{\eta^N \lambda^{3N}} \frac{1}{\prod_{\alpha=1}^{K} N_a!} [V^N + V^{N-2} \sum_{i<j}^{N} \int\int \Phi_{ij}\, d^3x_i\, d^3x_j]$$

$$= \frac{(\Delta\omega)^N V^N}{\eta^N \lambda^{3N}} \frac{1}{\prod_{\alpha=1}^{K} (N_\alpha!)} \left[1 + \frac{1}{V}\frac{1}{2}\sum_{i\neq j}^{N} \int \Phi_{ij}\, d^3x_{ij}\right]. \qquad [8]$$

We note that Φ_{ij} depends on the relative separation x_{ij} and the relative orientation between two molecules. Therefore, a better way to label the indices should be $\Phi_{\alpha\beta}(x_{ij})$, where α and β denote the angular orientations of the two molecules and x_{ij} the relative separation between their centers of mass. The summation over i and j can be rewritten as

$$\sum_{i\neq j}^{N} \int \Phi_{\alpha\beta}(x_{ij}) d^3x_{ij} = \sum_{\alpha,\beta=1}^{K} N_\alpha (N_\beta - \delta_{\alpha\beta}) \int \Phi_{\alpha\beta}(x)\, d^3x. \qquad [9]$$

As $N \to \infty$, the $\delta_{\alpha\beta}$ term can be neglected. The integral of $\Phi_{\alpha\beta}(x)$ is just the negative of excluded volume $V_{\alpha\beta}^{\text{ex.}}$. $Z(\{N_\alpha\}, N, V, kT)$ is now in the form

$$Z(\{N_\alpha\}, N, V, kT) = \frac{(\Delta\omega)^N V^N}{\eta^N \lambda^{3N}} \frac{1}{\prod_{\alpha=1}^{K} N_\alpha!} \left[1 - \frac{1}{2V}\sum_{\alpha,\beta=1}^{K} N_\alpha N_\beta V_{\alpha\beta}^{\text{ex.}}\right]. \qquad [10]$$

Taking the logarithm, dividing by N, and using Sterling's approximation $\ln N_\alpha! \simeq N_\alpha \ln N_\alpha$, we obtain

$$\frac{\ln[Z(\{N_\alpha\}, N, V, kT)]}{N} = \ln\frac{(\Delta\omega)V}{\eta\lambda^3} - \sum_{\alpha=1}^{K}\left(\frac{N_\alpha}{N}\ln\frac{N_\alpha}{N} + \frac{N_\alpha}{N}\ln N\right)$$
$$+ \frac{1}{N}\ln\left[1 - \frac{N^2}{2V}\sum_{\alpha,\beta}^{K}\frac{N_\alpha}{N}\frac{N_\beta}{N}V_{\alpha\beta}^{\text{ex.}}\right]$$
$$= \ln\left[\frac{(\Delta\omega)}{\eta\lambda^3}\frac{V}{N}\right] - \sum_{\alpha=1}^{K}\frac{N_\alpha}{N}\ln\frac{N_\alpha}{N} + \ln\left[1 - \frac{N^2}{2V}\sum_{\alpha,\beta}^{K}\frac{N_\alpha}{N}\frac{N_\beta}{N}V_{\alpha\beta}^{\text{ex.}}\right]^{1/N}$$
$$\simeq \ln\left[\frac{(\Delta\omega)}{\eta\lambda^3}\frac{V}{N}\right] - \sum_{\alpha=1}^{K}\frac{N_\alpha}{N}\ln\frac{N_\alpha}{N} + \ln\left[1 - \frac{N}{2V}\sum_{\alpha,\beta}^{K}\frac{N_\alpha}{N}\frac{N_\beta}{N}V_{\alpha\beta}^{\text{ex.}}\right]$$
$$\simeq \ln\frac{(\Delta\omega)}{\eta\lambda^3\rho} - \sum_{\alpha=1}^{K}\frac{N_\alpha}{N}\ln\frac{N_\alpha}{N} - \frac{\rho}{2}\sum_{\alpha,\beta}^{K}\frac{N_\alpha}{N}\frac{N_\beta}{N}V_{\alpha\beta}^{\text{ex.}}. \qquad [11]$$

Here $\rho \equiv N/V$ is assumed to be small.

Let us define an angular distribution function f such that $N_a = N \cdot f(\Omega_a) \cdot (\Delta\omega)$. Substituting N_a/N by $f(\Omega_a)$ and making the replacement

$$\sum_a (\Delta\omega) \rightarrow \int d\Omega\,,$$

we can put Eq. [11] in the form

$$\frac{1}{N} \ln Z(\{N_a\}, N, V, kT) = -\ln \eta\lambda^3\rho - \int d\Omega f(\Omega) \ln f(\Omega)$$
$$-\frac{\rho}{2}\int\int d\Omega d\Omega' f(\Omega) f(\Omega') V^{\text{ex.}}(\Omega - \Omega'). \qquad [12]$$

The second term on the right-hand side of Eq. [12] represents the orientational entropy, and the third term represents the effect of excluded volume. In order to maximize the right hand side of Eq. [12], we will use the Euler–Lagrange equation. This equation says if one wants to maximize the integral

$$I[y(x)] = \int_a^b F\left(y, \frac{dy}{dx}, x\right) dx$$

by varying the function $y(x)$, the correct $y(x)$ must satisfy the equation

$$\frac{\partial F}{\partial y} - \frac{d}{dx}\frac{\partial F}{\partial\left(\frac{dy}{dx}\right)} = 0.$$

If in addition $y(x)$ must satisfy the normalization condition

$\int_a^b y(x)\,dx = 1$, then the equation for $y(x)$ becomes

$$\frac{\partial F}{\partial y} - \frac{d}{dx}\frac{\partial F}{\partial\left(\frac{dy}{dx}\right)} - \nu = 0,$$

where ν is the Lagrange multiplier. Applying the Euler–Lagrange equation to Eq. [12] gives

$$\ln f(\Omega) + 1 + \nu + \rho \int f(\Omega') V^{\text{ex.}}(\Omega - \Omega')\, d\Omega' = 0. \qquad [13]$$

Eqs. [12] and [13] are the Onsager equations. In principle, Eq. [13] can be solved to get $f(\Omega)$ as a function of ρ and ν. The quantity ν is then determined by the normalization condition $\int f(\Omega) d\Omega = 1$. When there is more than one solution to Eq. [13], the results must be put into Eq. [12] in order to select the one solution that maximizes the right-hand side of Eq. [12]. Label that solution $f^o(\Omega)$. The free energy is then

$$\frac{F}{NkT} = \ln \eta\lambda^3\rho + \int d\Omega f^o(\Omega) \ln f^o(\Omega) + \frac{\rho}{2}\int\int d\Omega d\Omega' f^o(\Omega) f^o(\Omega') V^{\text{ex.}}(\Omega - \Omega'). \qquad [14]$$

Other thermodynamic quantities can be obtained directly from Eq. [14].

3. Solution of Onsager Equations in a Simplified Case

In practice, Eq. [13] is a nonlinear integral equation and its exact solution in the general case is difficult. Therefore, we will solve the Onsager equations in a very simplified case. Let us constrain the hard rods to point in only three orthogonal directions, say x, y, and z. Choose z as the preferred direction. If the fraction of hard rods pointing in the x-direction is r, the same fraction should point in the y-direction, since x and y directions are equivalent by uniaxial symmetry of the nematic phase. The fraction pointing in the z-direction is then $1 - 2r$. The order parameter

$$S \equiv \int_{-1}^{1} P_2(\cos\theta)\, f(\cos\theta)\, d(\cos\theta)$$

in this case is simply $(1-3r)$. Eq. [12] can now be written

$$\frac{Z_r(N,V,kT)}{N} = -\ln \eta\lambda^3\rho - 2r\ln r - (1-2r)\ln(1-2r)$$

$$-\rho r(2-3r)\,V_{\perp}^{\text{ex.}} - \frac{\rho}{2}(1-4r+6r^2)\,V_{\parallel}^{\text{ex.}}$$

$$= -\ln\frac{\eta\lambda^3\rho}{3} - \frac{1}{3}(1+2S)\ln(1+2S) - \frac{2}{3}(1-S)\ln(1-S)$$

$$-\frac{\rho(1-S^2)}{3}V_{\perp}^{\text{ex.}} - \frac{\rho}{2}\frac{1+2S^2}{3}V_{\parallel}^{\text{ex.}}. \qquad [15]$$

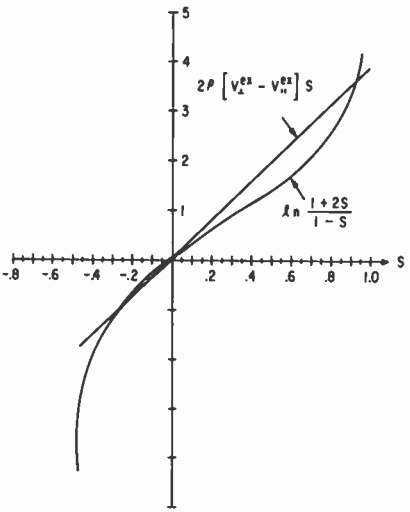

Fig. 2—Graphical solution of Eq. [16].

Here $V_{\perp}^{\text{ex}}$ and $V_{\parallel}^{\text{ex}}$ are the excluded volumes of two hard rods when they are respectively, perpendicular and parallel to each other.

To maximize $Z_r(N,V,kT)/N$, we merely differentiate with respect to S and set the result equal to zero. This gives

$$\ln\frac{1+2S}{1-S} = 2\rho\left[V_{\perp}^{\text{ex.}} - V_{\parallel}^{\text{ex.}}\right]S, \qquad [16]$$

which is the equivalent of Eq. [13]. In order to calculate $V^{ex.}$, we will take the rods to have the shape of rectangular parallelepiped with length L and width D. Then

$$V_{\perp}^{ex.} = \left(4 + 2\frac{L}{D} + 2\frac{D}{L}\right) D^2 L = \left(4 + 2l + \frac{2}{l}\right) V_o\,, \qquad [17a]$$

$$V_{\parallel}^{ex.} = 8D^2 L = 8V_o\,, \qquad [17b]$$

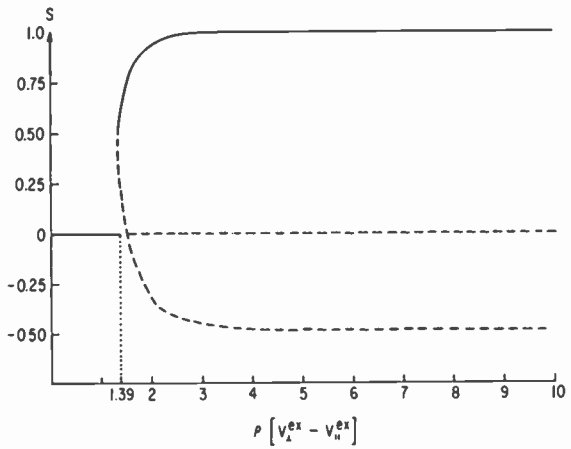

Fig. 3—Solution of Eq. [16] as a function of $\rho[V_{\perp}^{ex.} - V_{\parallel}^{ex.}]$. Dark lines indicate the branch that maximizes the right hand side of Eq. [15].

where $V_o = D^2 L$ is the volume of a parallelepiped and $l = L/D$ is the ratio of length to breadth. Eq. [16] can be solved graphically by plotting the right- and left-hand sides on the same graph and locating the points of intersection. This is shown in Fig. 2. The results are displayed in Fig. 3 as a function of $\rho[V_{\perp}^{ex.} - V_{\parallel}^{ex.}]$. Dark lines indicate the stable solution. Label these values of S by $S^o(\rho)$. The free energy is

$$\frac{F}{NkT} = \ln\left[\frac{N\eta\lambda^3}{3V}\right] + \frac{1}{3}(1 + 2S^o(\rho))\ln(1 + 2S^o(\rho))$$
$$+ \frac{2}{3}(1 - S^o(\rho))\ln(1 - S^o(\rho))$$
$$+ 2\frac{NV_o}{V}\left[\frac{1 - (S^o(\rho))^2}{3}\left(l + \frac{1}{l} - 2\right) + 2\right]. \qquad [18]$$

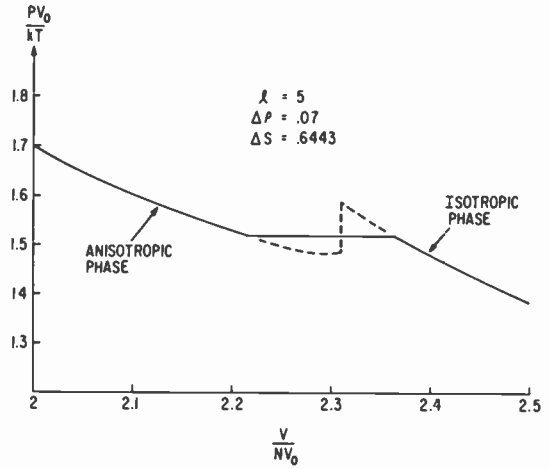

Fig. 4—Reduced pressure PV_o/kT plotted as a function of reduced volume V/V_oN for $l = 5$.

The pressure is obtained by differentiating F with respect to V:

$$\frac{PV_o}{kT} = -\frac{V_o}{kT}\frac{\partial F}{\partial V} = \frac{V_oN}{V} + 2\left(\frac{V_oN}{V}\right)^2\left[\frac{1-(S^o(\rho))^2}{3}\left(l + \frac{1}{l} - 2\right) + 2\right]. \quad [19]$$

In Figs. 4 and 5, reduced pressure PV_o/kT is plotted versus reduced volume V/V_oN for two values of l. It should be noted that there is a

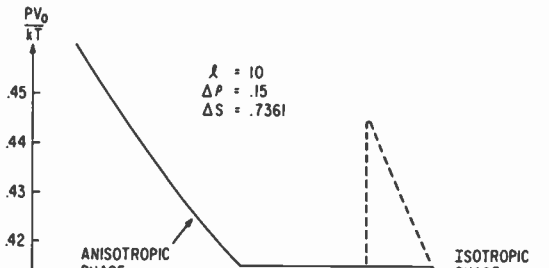

Fig. 5—Reduced pressure PV_o/kT plotted as a function of reduced volume V/V_oN for $l = 10$.

van der Waals loop in each curve. Using the standard Maxwell equal-area construction, we obtain the magnitudes of density and order parameter discontinuities ($\Delta\rho$ and ΔS) across the transition. Their values are typically $\Delta\rho \sim 0.1$ and $\Delta S \sim 0.7$, which are close to the results obtained by the variational solution of the exact Onsager equations. How well do these values agree with the experimental results? Typical experimental values for $\Delta\rho$ and ΔS are $\sim .01$ and .4, respectively. Therefore, there exists a large discrepancy between the theoretical predictions and the experimental results.

What went wrong? The answer probably lies in the neglect of short-range order. In real liquid crystals there are short-range attractive interactions that favor parallel alignment of the molecules. This means that parallel molecules prefer to lie close to each other and form "bundles". In this kind of configuration, a molecule would most probably interact with those molecules pointing in similar orientations, thus reducing the excluded-volume effect. A lattice-gas model calculation[7] that includes the short-range anisotropic attractive interaction as well as the steric repulsion has shown that "bundling" would indeed soften the isotropic-anisotropic phase transition and decrease the values of $\Delta\rho$ and ΔS. Therefore, the joint consideration of short-range order and steric repulsion seems to be the direction for improving the hard-rod model.

References:

[1] L. Onsager, "The Effects of Shapes on the Interaction of Colloidal Particles," **Ann. N.Y. Acad. Sci.**, Vol. 51, p. 627 (1949).

[2] R. Zwanzig, "First-Order Phase Transitions in a Gas of Long Thin Rods," **J. Chem. Phys.**, Vol. 39, p. 1714 (1963).

[3] P. J. Flory, "Phase Equilibriums in Solutions of Rodlike Particles," **Proc. Roy. Soc.** (London), Vol. A234, p. 73 (1956).

[4] E. A. DiMarzio, "Statistics of Orientation Effects in Linear Polymer Molecules," **J. Chem. Phys.**, Vol. 35, p. 658 (1961).

[5] G. Lasher, "Nematic Ordering of Hard Rods Derived from a Scaled Particle Treatment," **J. Chem. Phys.**, Vol. 53, p. 4141 (1970).

[6] R. H. Fowler, **Statistical Mechanics**, p. 62, Cambridge University Press, Cambridge, England (1966).

[7] P. Sheng, "Effects of Bundling in a Lattice Gas Model of Liquid Crystals," **J. Chem. Phys.**, Vol. 59, p.1942 (1973).

Nematic Order: The Long Range Orientational Distribution Function

E. B. Priestley

RCA Laboratories, Princeton, N. J. 08540

Abstract—This lecture presents a detailed discussion of the long range orientational distribution function for the nematic phase. It is shown that experiments measure moments of this distribution function rather than the distribution function itself. Both microscopic and macroscopic definitions of nematic order are discussed and the relationship between them is derived for the case of rigid rod-like molecules. Experimental measurements of the order are described and data from a number of experiments is presented.

1. Introduction

In the third lecture of this series[1] the existence of the nematic phase was presented as an example of an order–disorder phenomenon. The symmetry and structure of the nematic phase were used to identify the natural order parameter $\langle P_2(\cos\theta)\rangle$, where $P_2(\cos\theta)$ is the second Legendre polynomial and the angular brackets denote a statistical average over the orientational distribution function $f(\cos\theta)$. The orientational potential energy of a single molecule was shown, in the mean field approximation, to be

$$V(\cos\theta) = -v\langle P_2(\cos\theta)\rangle P_2(\cos\theta) \qquad [1]$$

where v is a number that scales with the strength of the intermolecular interaction. Using the rules of classical statistical mechanics, the theoretical orientational distribution function $\rho(\cos\theta)$ was given

in terms of the mean field potential $V(\cos\theta)$ as

$$\rho(\cos\theta) = Z^{-1} \exp[-\beta V(\cos\theta)] \qquad [2]$$

with

$$Z = \int_0^1 \exp[-\beta V(\cos\theta)]\, d(\cos\theta).$$

In Eq. [2] Z is the single-particle partition function and $\beta = 1/kT$, where k is Boltamann's constant and T is the absolute temperature.

It is important at this point to distinguish between $f(\cos\theta)$ and $\rho(\cos\theta)$. Given that the nematic phase is truly uniaxial, $f(\cos\theta)$ completely describes the long range orientational molecular order and therefore can be regarded as the exact or true single-particle distribution function. On the other hand, $\rho(\cos\theta)$ is a theoretical approximation to $f(\cos\theta)$. The extent to which it represents a *good* approximation depends upon how closely $V(\cos\theta)$ approximates the true potential of mean torque.

There is an obvious motivation for determining as much as possible experimentally about $f(\cos\theta)$; it describes the long range orientational ordering of the molecules which, of course, is the single feature that distinguishes the nematic phase from the isotropic phase. The average values of various quantities of interest pertaining to the nematic phase could be computed if $f(\cos\theta)$ were known with precision.

2. The Orientational Distribution Function

The main question we want to answer in this lecture is "What do experiments tell us about the orientational distribution function?". To answer this question it is instructive to expand $f(\cos\theta)$ in a formal mathematical sense as[2]

$$f(\cos\theta) = \sum_{l_{even}} \frac{2l+1}{2} \langle P_l(\cos\theta)\rangle P_l(\cos\theta), \qquad [3]$$

where the $P_l(\cos\theta)$ are the l^{th} even order Legendre polynomials. Notice that the expansion has the correct symmetry and that $f(\cos\theta)$ is normalized. The coefficients $\langle P_l(\cos\theta)\rangle$ are defined by

$$\langle P_l(\cos\theta)\rangle = \int_{-1}^{1} P_l(\cos\theta)\, f(\cos\theta)\, d(\cos\theta). \qquad [4]$$

Explicitly, the first three coefficients are

$$\langle P_0(\cos\theta)\rangle = 1,$$

$$\langle P_2(\cos\theta)\rangle = \frac{1}{2}(3\langle\cos^2\theta\rangle - 1), \qquad [5]$$

$$\langle P_4(\cos\theta)\rangle = \frac{1}{8}(35\langle\cos^4\theta\rangle - 30\langle\cos^2\theta\rangle + 3).$$

There is no practical experimental means of measuring $f(\cos\theta)$ directly. Rather, individual experiments each detect some property of the nematic phase averaged over $f(\cos\theta)$. Thus, experiments are sensitive to $f(\cos\theta)$ only through its influence on these averaged properties. The most commonly measured such property is the temperature dependence of $\langle\cos^2\theta\rangle$ and, hence, the temperature dependence of the order parameter $\langle P_2(\cos\theta)\rangle$. Recent measurements of $\langle\cos^4\theta\rangle$ as a function of temperature for two nematic materials[3] have permitted the evaluation of $\langle P_4(\cos\theta)\rangle$ over the entire nematic temperature range as well. Therefore, the answer to the question posed at the beginning of this section is that experiments measure the coefficients in the expansion of $f(\cos\theta)$, (Eq. [3]). In other words, experiments measure different moments of the orientational distribution function. These experimentally determined moments can be used to evaluate truncated series approximations to $f(\cos\theta)$. It is convenient to label these approximate distribution functions as $f^N(\cos\theta)$ where N is the Roman numeral corresponding to the number of terms retained in the truncated series.

In the discussion so far, the constituent molecules of the nematic phase have been assumed to be representable by simple rigid rods so as to make the definition of a molecular axis unambiguous. The order parameter $\langle P_2(\cos\theta)\rangle$ has been defined from a microscopic point of view by treating it as a statistical average of individual molecular behavior. In most cases this is an adequate description since real nematogens most often do behave like simple rigid rods. However, if the molecules do not behave like simple rigid rods, this microscopic description of order is no longer adequate and we must find some other

means for specifying the degree of order. For this, we turn to a consideration of macroscopic response functions of the nematic phase and show how a suitable order parameter can be defined using these response functions.

3. Macroscopic Definition of Nematic Order

In deriving a macroscopic order parameter, we will use the diamagnetic susceptibility as an example. However, any other macroscopic property, e.g., refractive index or dielectric response, could be used as well.

Consider the relationship between magnetic moment $\vec{M}$ and magnetic field $\vec{H}$

$$M_\alpha = \chi_{\alpha\beta} H_\beta, \alpha,\beta = x,y,z\,. \qquad [6]$$

$\chi_{\alpha\beta}$ represents the $\alpha\beta$-component of the diamagnetic susceptibility tensor $\overleftrightarrow{\chi}$ and, for static fields, $\chi_{\alpha\beta} = \chi_{\beta\alpha}$. In Eq. [6], the summation convention over repeated indices is implied. For the uniaxial nematic phase, we can write $\overleftrightarrow{\chi}$ in the diagonal, but completely general form

$$\overleftrightarrow{\chi} = \begin{pmatrix} \chi_\perp & 0 & 0 \\ 0 & \chi_\perp & 0 \\ 0 & 0 & \chi_\parallel \end{pmatrix}, \qquad [7]$$

where $\chi_\parallel$ and $\chi_\perp$ refer to the susceptibility parallel and perpendicular to the symmetry axis, respectively. $\overleftrightarrow{\chi}$ itself is not a useful order parameter because it does not vanish in the isotropic phase, but has the value

$$\begin{aligned} \chi &= \frac{1}{3}(2\chi_\perp + \chi_\parallel) \\ &= \frac{1}{3}\chi_{\gamma\gamma}. \end{aligned} \qquad [8]$$

However, if we extract the anisotropic part of $\overleftrightarrow{\chi}$, viz $\overleftrightarrow{\chi}^a$ defined by

$$\chi^a{}_{\alpha\beta} = \chi_{\alpha\beta} - \frac{1}{3}\chi_{\gamma\gamma}\,\delta_{\alpha\beta}, \qquad [9]$$

which does vanish in the isotropic phase, we can use it to define a suitable order parameter.

Combining Eqs. [7] and [9] we find for the nematic phase

$$\overleftrightarrow{\chi}^a = \frac{2}{3}\Delta\chi \begin{pmatrix} -1/2 & 0 & 0 \\ 0 & -1/2 & 0 \\ 0 & 0 & 1 \end{pmatrix}, \qquad [10]$$

where $\Delta\chi = \chi_\parallel - \chi_\perp$. It should be noted that $\overleftrightarrow{\chi}^a$ is temperature dependent because the magnitude of $\Delta\chi$ is temperature dependent. If we denote the maximum possible diamagnetic anisotropy (i.e., the anisotropy for a perfectly ordered nematic phase) as $(\Delta\chi)_{max}$, we can define the desired order parameter as

$$Q_{\alpha\beta} = \frac{3}{2}\frac{\chi^a{}_{\alpha\beta}}{(\Delta\chi)_{max}}. \qquad [11]$$

Notice that $Q_{\alpha\beta}$ has values between 0 (isotropic phase) and 1 (perfectly ordered nematic phase) and that it has been derived without any assumption about molecular rigidity. $Q_{\alpha\beta}$ is a valid measure of the order for any nematic liquid crystal. As mentioned earlier, $Q_{\alpha\beta}$ could have been defined in terms of the anisotropy in any other macroscopic response function.

One might wonder if there is any relationship between $Q_{\alpha\beta}$ and $\langle P_2(\cos\theta)\rangle$. Indeed, *in nematic phases whose constituent molecules can be approximated by simple rigid rods,* these two measures of the long range order are related. The next section deals explicitly with this relationship.

4. Relationship Between Microscopic and Macroscopic Order Parameters

The diamagnetic susceptibility $\overleftrightarrow{\zeta}$ of a single rod-like molecule can be described by two parameters $\zeta_\parallel$ and $\zeta_\perp$, representing the molecular response to a magnetic field applied parallel and perpendicular to the molecular axis, respectively. In tensor notation the magnetic susceptibility of the molecule is given by

$$\overleftrightarrow{\zeta} = \begin{pmatrix} \zeta_\perp & 0 & 0 \\ 0 & \zeta_\perp & 0 \\ 0 & 0 & \zeta_\parallel \end{pmatrix}. \qquad [12]$$

To find the macroscopic diamagnetic anisotropy we first rotate $\overleftrightarrow{\zeta}$ by an arbitrary rotation $R(\phi, \theta, \psi)$, ϕ, θ, and ψ being the Euler angles of the rotation, and then perform a statistical average. In a uniaxial nematic, the angles ϕ and ψ are isotropically distributed so averages over them can be carried out explicitly. The orientational distribution function $f(\cos\theta)$ describes the distribution of the angle θ, and averages over θ are designated by angular brackets.

From the general formalism for rotation of second rank tensors[4] it can be shown that

$$\zeta_{xx}^{\mathrm{ROT}} = \frac{1}{3}(2\zeta_\perp + \zeta_\parallel) - \frac{1}{6}(\zeta_\parallel - \zeta_\perp)\,[3(1-\cos^2\theta)\cos 2\psi - (3\cos^2\theta - 1)].$$

and [13]

$$\zeta_{zz}^{\mathrm{ROT}} = \frac{1}{3}(2\zeta_\perp + \zeta_\parallel) + \frac{1}{3}(\zeta_\parallel - \zeta_\perp)(3\cos^2\theta - 1),$$

where $\zeta_{ij}^{\mathrm{ROT}}$ are components of the rotated molecular diamagnetic susceptibility tensor. The macroscopic diamagnetic anisotropy is then

$$\Delta\chi = N\,[\langle\zeta_{zz}^{\mathrm{ROT}}\rangle - \langle\zeta_{xx}^{\mathrm{ROT}}\rangle], \qquad [14]$$

where N is the number of molecules per cubic centimeter. Taking the averages of the $\zeta_{ij}^{\mathrm{ROT}}$ and substituting into Eq. [14] gives

$$\Delta\chi = N\,(\zeta_\parallel - \zeta_\perp)\,\langle P_2(\cos\theta)\rangle. \qquad [15]$$

But $N(\zeta_\parallel - \zeta_\perp)$ is simply the macroscopic diamagnetic anistropy of the perfectly ordered nematic phase, i.e.,

$$(\Delta\chi)_{\max} = N(\zeta_\parallel - \zeta_\perp). \qquad [16]$$

Thus,

$$\Delta\chi = (\Delta\chi)_{\max}\langle P_2(\cos\theta)\rangle. \qquad [17]$$

Combining Eqs. [10], [11], and [17] yields

$$Q_{\alpha\beta} = \langle P_2(\cos\theta)\rangle \begin{pmatrix} -1/2 & 0 & 0 \\ 0 & -1/2 & 0 \\ 0 & 0 & 1 \end{pmatrix} \qquad [18]$$

for a nematic liquid crystal composed of rod-like molecules.

As noted at the beginning of Section 3, $Q_{\alpha,\beta}$ can be defined equally well in terms of other macroscopic response functions such as the dielectric tensor $\overleftrightarrow{\epsilon}$. However, a theoretical relationship between $\Delta\epsilon$ (macroscopic measure of the order) and $<P_2(\cos\theta)>$ (microscopic measure of the order) cannot be derived in the absence of certain questionable assumptions. This inability to establish a rigorous relationship analogous to Eq. [14] between the dielectric anisotropy $\Delta\epsilon$ and the polarizability α_{ij} results from complicated depolarization effects caused by the relatively large near-neighbor electrostatic interaction. Nevertheless, it has been established empirically[5] that the analog of Eq. [17] does hold, i.e., the macroscopic anisotropy does scale directly with the microscopic order parameter $<P_2(\cos\theta)>$. Consequently, electrical and optical anisotropy measurements continue to be used to measure $<P_2(\cos\theta)>$ in nematics composed of rod-like molecules, even though theoretical justification for this is presently lacking.

5. Experimental Measurements

Various experimental methods have been used to examine molecular ordering in nematic liquid crystals[6]. All the methods fall into one of two groups—those that measure the anisotropy in some macroscopic response function and those that measure $<P_2(\cos\theta)>$ directly. As we have already seen, those in the first group also permit a determination of $<P_2(\cos\theta)>$ because of equations analogous to Eg. [17] that relate the macroscopic anisotropy to the microscopic order. In general, there is quite good agreement among the various measures of $<P_2(\cos\theta)>$ for materials that have been studied by one or more methods from each group, indicating that nematogenic molecules can be approximated rather well by hard rods. We turn now to a brief description of the various experimental techniques and refer the interested reader to more detailed discussions in each instance.

5.1 Measurements of $<P_2(\cos\theta)>$ Based on Macroscopic Anisotropies

Little need be said concerning this type of order parameter determination. It is evident from Eq. [17] that the only requirement in evaluating $<P_2(\cos\theta)>$ from macroscopic anisotropy measurements is a knowledge of the maximum possible magnitude of the anisotropy being measured. Clearly, this is the anisotropy that would be measured in a perfectly ordered nematic phase and can be obtained by means of a little algebra from the crystalline anisotropy. Diamagnetic, dielectric, and optical anisotropy measurements have been used extensively to

determine the temperature dependence of $<P_2(\cos\theta)>$ for a variety of nematic liquid crystals. Further details about the conduct of these experiments and analysis of the data can be found in References [6] and [7].

5.2 Measurements of $<P_2(\cos\theta)>$ Based on Microscopic Anisotropies

In this section we group techniques that sense the anisotropy in various properties of *individual molecules* as opposed to those discussed above, which sense bulk anisotropies. It is impossible to measure the anisotropy of a single molecule in a nematic phase; rather, these techniques measure the statistical average (both temporal and spatial) of the molecular anisotropy. The averaging process results in the measured anisotropy being proportional to $<P_2(\cos\theta)>$ for most of these techniques. For the technique based on Raman scattering measurements, the anisotropy is related to both $<P_2(\cos\theta)>$ and $<P_4(\cos\theta)>$.

(a) *Magnetic Resonance Techniques*

An excellent review of magnetic resonance methods has been given recently by Brown *et al.*[8] We simply point out that, for molecules having nuclei with spin $I = 1/2$ (such as H), the dipole-dipole splitting in the NMR spectrum of the nematic phase, due to a proximal pair of such nuclei in the same molecule, is proportional to $<P_2(\cos\theta)>$. In addition, for molecules having nuclei with spin $I \geq 1$ (such as D and ^{14}N), the quadrupole splitting can be used to determine $<P_2(\cos\theta)>$. Finally, anisotropy in the Zeeman and hyperfine splitting observed in the EPR spectrum of free radicals dissolved in nematic liquid crystals also allows one to determine the order parameter, assuming the paramagnetic guest aligns sympathatically with the host nematic material.

(b) *Raman Scattering Technique*

Details of the Raman scattering technique have been published elsewhere.[3] Successful utilization of the technique requires the existence of a (preferably) strong, narrow, anisotropic Raman line associated with an identifiable vibration of the nematogen. It is straightforward to show that the anisotropy in the Raman scattering from such a vibration observed in the laboratory frame of reference contains information about the statistical averages $<P_2(\cos\theta)>$ and $<P_4(\cos\theta)>$. This unique feature of the Raman technique, viz. the ability to determine $<P_4>$ as well as $<P_2>$, stems from the fourth rank tensor nature of the scattering interaction.

Having three moments $<P_o>$, $<P_2>$ and $<P_4>$ of the orientational distribution function allows us to evaluate f^{III} (cos θ) (See Sec. 2). In the next section we present NMR, optical and magnetic anisotropy, and Raman measurements of $<P_2$ (cos $\theta)>$, Raman measurements of $<P_4$ (cos $\theta)>$, and representative plots of f^{III} (cos θ).

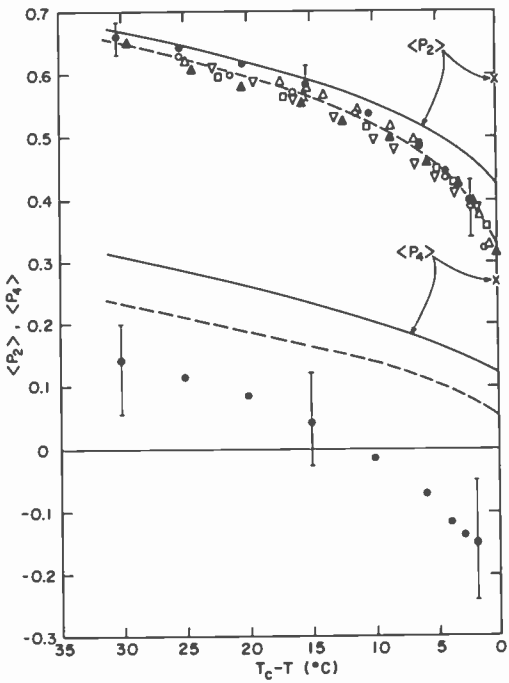

Fig. 1—Theoretical and experimental values of the nematic order parameters $<P_2$ (cos $\theta)>$ and $<P_4$ (cos $\theta)>$: solid line, theoretical results of simple mean field theory[9]; dashed line, HJL theory[10]; crosses, Onsager-Lakatos theory[13]; filled circles, Raman measurements; open circles, NMR data on partially deuterated MBBA; squares, relative values obtained from measurements of the optical anisotropy; and triangles, relative values obtained from measurements of the diamagnetic anisotropy.[7] (Reprinted from Ref. [2].)

6. Experimental Data

In Fig. 1 we display the data of Reference [3]. Notice that the $<P_2>$ results from NMR, optical and diamagnetic anisotropy, and Raman measurements all agree very well. This is reasonably compelling evidence that all of these techniques, and the Raman technique in particular, are indeed measuring $<P_2$ (cos $\theta)>$. The $<P_4>$ data,

which come only from the Raman measurements, are seen to become negative near the nematic-isotropic phase transition. The physical meaning and implications of negative $\langle P_4 \rangle$ have been discussed by Jen *et al*[3] and by P. Wojtowicz[9] in the fourth lecture of this series.

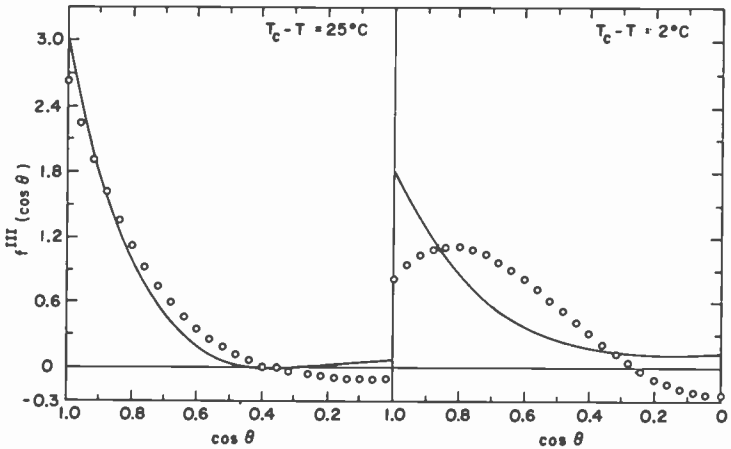

Fig. 2—Plot of the theoretical and experimental truncated orientational distribution function $f^{III}(\cos\theta)$; solid line, HJL theory;[10] circles, Raman measurements. (Reprinted from Ref. [2].)

Fig. 2 shows a plot of $f^{III}(\cos\theta)$ for two temperatures using the experimental Raman values of $\langle P_2 \rangle$ and $\langle P_4 \rangle$ in Eq. [3]. For comparison, we also plot $f^{III}(\cos\theta)$ for the same two temperatures using values of $\langle P_2 \rangle$ and $\langle P_4 \rangle$ calculated from the Humphries-James-Luckhurst model[9,10] after the parameters were adjusted to obtain good agreement with the $\langle P_2 \rangle$ data. Note that f^{III} need not be positive definite because of truncation errors. The principal result to see in Fig. 2 is that the molecules have a stronger tendency to be tipped away from the nematic axis than is predicted by mean field theory. *This tendency is strongest near the nematic-isotropic phase transition.* In addition to mean field theories, other statistical mechanical models of nematic ordering have been developed. In particular there is the Onsager model[11,12] for the ordering of a system of hard rods as a function of density. Using this model, Lakatos[13] has recently calculated values of $\langle P_l(\cos\theta) \rangle$ for all l. In Fig. 1 we also show these results for $\langle P_2 \rangle$ and $\langle P_4 \rangle$ at the transition density. The ratio of $\langle P_4 \rangle / \langle P_2 \rangle$ as a function of $\langle P_2 \rangle$ is essentially the same as that calculated from mean field theory and it also disagrees with the experimental results.

There has been considerable speculation[3,9] regarding the origin of

the discrepancy between experiment and mean field theory. As of this writing, that discrepancy remains unexplained, though extensive work is underway on both the experimental and theoretical fronts in an attempt to better understand the exact nature of nematic ordering and the single-particle orientational distribution function $f(\cos\theta)$.

References:

[1] P. J. Wojtowicz, "Introduction to the Molecular Theory of Nematic Liquid Crystals," **RCA Rev.**, Vol. 35, p. 105, March 1974 (this issue).

[2] E. B. Priestley, P. S. Pershan, R. B. Meyer, and D. H. Dolphin, "Raman Scattering from Nematic Liquid Crystals. A Determination of the Degree of Ordering," **Vijnana Parished Anurandhan Patrike**, Vol. 14, p. 93 (1971).

[3] Shen Jen, N. A. Clark, P. S. Pershan, and E. B. Priestley, "Raman Scattering from a Nematic Liquid Crystal: Orientational Statistics," **Phys. Rev. Lett.**, Vol. 31, p. 1552 (1973); E. B. Priestley and P. S. Pershan, "Investigation of Nematic Ordering Using Raman Scattering," **Mol. Cryst. Liquid Cryst.**, Vol. 23, p. 369 (1973); and E. B. Priestley and A. E. Bell (to be published).

[4] E. B. Priestley and P. J. Wojtowicz, unpublished results.

[5] N. V. Madhusudana, R. Shashidhar, and S. Chandrasekhar, "Orientational Order in Anisaldazine in the Nematic Phase," **Mol. Cryst. Liquid Cryst.**, Vol. 13, p. 61 (1971).

[6] A. Saupe and W. Maier, "Methods for the Determination of the Degree of Order in Nematic Liquid-Crystal Layers," **Z. Naturforschg.**, Vol. 16a, p. 816 (1961).

[7] G. Sigaud and H. Gasparoux, **J. Chem. Phys. Physicochim. Biol.**, Vol. 70, p. 669 (1973); I. Haller, "Elastic Constants of the Nematic Liquid Crystalline Phase of p-Methoxybenzylidene-p-n-Butlylaniline (MBBA)," **J. Chem. Phys.**, Vol. 57, p. 1400 (1972); P. I. Rose, Fourth International Liquid Crystal Conf., Kent State University, Kent, Ohio, 1972 (to be published) see also Ref. (5).

[8] G. H. Brown, J. W. Doane, and V. D. Neff, **A Review of the Structure and Physical Properties of Liquid Crystals**, The CRC Press, Cleveland, Ohio (1971).

[9] P. J. Wojtowicz, "Generalized Mean Field Theory of Nematic Liquid Crystals," **RCA Rev.**, Vol. 35, p. 118, March 1974 (this issue).

[10] R. L. Humphries, P. G. James, and G. R. Luckhurst, "Molecular Field Treatment of Nematic Liquid Crystals," **J. Chem. Soc. Faraday Trans. II**, Vol. 68, p 1031 (1972).

[11] L. Onsager, "The Effects of Shapes on the Interaction of Colloidal Particles," **Ann. N.Y. Acad. Sci.**, Vol. 51, p. 627 (1949).

[12] P. Sheng, "Hard Rod Model of the Nematic-Isotropic Phase Transition," **RCA Rev.**, Vol. 35, p. 132, March 1974 (this issue).

[13] K. Lakatos, **J. Status Phys.**, Vol. 2, p. 121 (1970).

Recent Papers by RCA Authors

Listing is alphabetical by name of primary author. For copies of reprints, the reader should contact the publication directly.

A. Akselrad, R. E. Novak, and D. L. Patterson, "New Si-Based Garnet Films for Magnetic-Bubble Devices with Magneto-optic Applications," **19th Conf. Magnetism and Magnetic Materials,** Boston, Mass., Nov. 13, 1973.

M. P. Bachynski, "The Need for Leadership in Science and Technology," **IEEE International Electrical and Electronics Conf.,** Toronto, Oct. 1973.

D. Balzer and A. C. Belsley, "Ascent Phase and Orbital Correction Propulsion Module," **AIAA 9th Propulsion Conf.,** Las Vegas, Nev., Nov. 7, 1973.

D. L. Balzer, "Block 5D Ascent Phase Propulsion System," 1973 JANNAF Propulsion Mtg.; **Chem. Propulsion Information Agency J.,** Las Vegas, Nev., Nov. 6-8, 1973.

R. A. Bartolini, N. Feldstein, and R. J. Ryan, "Replication of Relief-Phase Holograms for Prerecorded Video," **J. Electrochem. Soc.,** Vol. 120, No. 10, p. 1408, Oct. 1973.

O. E. Bessette, "A High Capacity, High Data Rate Instrumentation Tape Recording System," **International Telemetering Conf. Proc.,** Wash., D.C., Vol. 9, p. 74, Oct. 9-11, 1973.

P. J. Bird, "Modular Switching Approach for Local and Remote Subscribers," **National Telecommunications Conf. Proc.,** Atlanta, Ga., Nov. 28, 1973.

B. F. Bogner, "Ultra Lightweight Stripline RF Manifold," **11th Electrical and Electronic Insulation Conf. Proc.,** Chicago, Ill., Oct. 3, 1973.

A. Bloom and R. A. Bartolini, "A New Volume Phase Hologram Recording Medium," **Optical Soc. Amer. Ann. Meeting,** Rochester, N.Y., Oct. 1973.

B. F. Bogner, "Conformal Arrays Come of Age," **Microwave J.,** Oct. 1973.

J. H. Bowen, M. E. Breese, V. A. Mikenas, and M. Weiss, "Analytic and Experimental Techniques for Evaluating Transient Thermal Characteristics of Trapatt Diodes," **IEEE International Electron Devices Mtg.,** Wash., D.C., Dec. 3-5, 1973.

J. M. Cies, "Combined Modal and Analog Vibration Analysis," **44th Shock and Vibration Symp.,** Symp. Bulletin, Houston, Texas, Dec. 4-7, 1973.

R. S. Crandall, "Collective Modes of a Two-Dimensional Wigner Crystal," **Phys. Rev. A,** Vol. 18, No. 4, p. 2136, Oct. 1973.

G. W. Cullen, M. T. Duffy, and C. C. Wang, "Materials Integration Through Hetero-epitaxial Growth on Insulating Substrates," **Electrochem. Soc.,** 3rd International Conf. on CVD, Boston, Mass., Oct. 7-12, 1973.

B. J. Curtis and J. P. Dismukes, "An Investigation of Convective Effects in a Barrel Reactor," **4th International Conf. on Chemical Vapor Deposition,** Boston, Mass., Oct. 7-12, 1973.

W. Czaja, C. F. Schwerdtfeger, "Evidence for Electron-Hole-Droplet Formation in AgBr," **Swiss Phys. Soc. Mtg.,** Lugano, Switzerland, Oct. 19-20, 1973.

J. Danko, M. Hecht, and T. Altman, "Geometric Corrections—Constant Resolution Processor," Management and Utilization of Remote Sensing Data, **Amer. Soc. of Photogrammetry,** Sioux Falls, S.D., Oct. 30, 1973.

J. G. Davy, and J. J. Hanak, "RF Bias Evaporation (Ion Plating) of Nonmetal Thin Films," **29th Amer. Vacuum Soc. Symp.,** New York, Oct. 1973.

D. A. DeWolf, "Strong Irradiance Fluctuations in Turbulent Air: Spherical Waves," **J. Optical Soc. Amer.**, Vol. 63, No. 10, p. 1249, Oct. 1973.

J. P. Dismukes, J. Kane, B. Binggeli, and H. P. Schweizer, "Chemical Vapor Deposition of Catholdoluminescent Phospor Layers," **4th International Conf. on Chemical Vapor Deposition**, Boston, Mass., Oct. 7-12, 1973.

J. P. Dismukes and J. Kane, "Evaluation of an Organometallic Approach to Garnet Chemical Vapor Deposition," **4th International Conf. on Chemical Vapor Deposition**, Boston, Mass., Oct. 7-13, 1973.

T. J. Faith, and A. F. Obsenschain, "Temperature, Illumination, and Fluence Dependence of Current and Voltage in Electron Irradiated Solar Cells," **IEEE Photovoltaic Specialists Conf., Proc.**, Palo Alto, Calif., Nov. 11-13, 1973.

A. H. Firester, M. E. Heller, and J. P. Wittke, "Inexpensive Laser Mirrors," **Amer. J. Phys.**, Vol. 41, p. 1202, Oct. 1973.

J. Gerber, J. P. Dismukes, and R. J. Ulmer, "Chemical Vapor Deposition of Cathodoluminescent Phosphor Layers of Y_2O_3:Eu (Red) and La_2O_2S:Pr (Green) on TV Glass, Quartz, and Sapphire," **4th International Conf. on Chemical Vapor Deposition**, Boston, Mass., Oct. 7-12, 1973.

J. I. Gittleman, and B. Abeles, "Blocking Temperature Effects in Fine Nicker Particles," **18th Conf. on Magnetism and Magnetic Materials**, Boston, Mass., Nov. 13-16, 1973.

J. L. Grever, "Possibilities for a New Compatible Quadruplex Video Recording Forman," **114th Conf. SMPTE**, New York, Oct. 18, 1973.

H. M. Gurk, "The Need for More Information and Less Data," Management and Utilization of Remote Sensing Data, **Amer. Soc. of Photogrammetry**, Sioux Falls, S.D., Oct. 29-Nov. 2, 1973.

J. J. Hanak, "Automation of the Search for Electronic Materials by Means of Cosputtering," **1973 International Conf. on Sputtering and Its Applications**, Montpellier, France, Oct. 2-5, 1973.

G. Harbeke, "Anisotropic Exciton Polaritons," **Swiss Physical Soc. Mtg.**, Lugano, Switzerland, Oct. 19-20, 1973.

W. I. Harrington and R. E. Honig, "Ion Scattering Spectrometry Below 10 keV," **144th Mtg. Electrochem. Soc.**, Boston, Mass., Oct. 7-12, 1973.

M. Hecht and S. Henry, "Two-Dimensional Interpolative Compressor," Management and Utilization of Remote Sensing Data, **Amer. Soc. of Photogrammetry**, Sioux Falls, S.D., Oct. 30, 1973.

R. Hirota, "Exact Three-Soliton Solution of the Two-Dimensional Sine-Gordon Equation," **Phys. Soc. of Japan Mtg.**, Keio Univ., Japan, Nov. 22-25, 1973.

R. Hirota, "Higher Conservation Laws of the Toda Lattice," **Physical Soc. of Japan Mtg.**, Keio Univ., Japan, Nov. 22-25, 1973.

R. Hirota and K. Suzuki, "Theoretical and Experimental Studies of Lattice Solitons in Nonlinear Lumped Networks," **Proc. IEEE**, Vol. 61, No. 10, p. 1483, Oct. 1973.

H. O. Hook, "The Capabilities and Limitations of Photolithography and Other Non-Electron-Beam Lithography," **20th National Vacuum Soc. Symp.**, New York City, Oct. 9-13. 1973.

C. R. Horton, "User-Oriented Image Data Cartridge Recording System," **Proc. International Telemetering Conf.**, Vol. 9, p. 86, Wash., D.C., Oct. 9-11, 1973.

D. H. Hurlburt, "Multistrip Coupled Acoustic Surface Wave Filters," **IEEE Ultrasonics Symp.**, Monterey, Calif., Nov. 1973.

H. Kiess, "Charge Carrier Transport in ZnO," **2nd International Conf. on Electrophotography**, Wash., D.C., Oct. 24-27, 1973.

R. Klein, "On the Interpretation of Phonon Transport Theory for Structural Phase Transitions," **Swiss Phys. Soc. Mtg.**, Lugano, Switzerland, Oct. 19-20, 1973.

H. Kressel and M. Ettenberg, "Electro- and Photoluminescence of GaAS:Ge Prepared by Liquid Phase Epitaxy," **Appl. Phys. Lett.**, Vol. 23, No. 9, p. 511, Nov. 1, 1973.

H. Kressel, C. J. Nuese, and I. Ladany, "Luminescence from $In_{0.5}Ga_{0.5}P$ Prepared by Vapor-Phase Epitaxy," **J. Appl. Phys.**, Vol. 44, No. 7, p. 3266, July 1973.

B. J. Levin and G. Weidner, "A Distributed Pin Diode Phaser for Millimeter Wavelengths," **Microwave J.**, Vol. 16, No. 11, p. 42, Nov. 1973.

A. F. Martz, "Can Taped ERTS Data by Previewed?" Management and Utilization of Remote Sensing Data, **Amer. Soc. Photogrammetry**, Sioux Falls, S.D., Oct. 29-Nov. 2, 1973.

R. J. McIntyre, "Factors Affecting the Ulitmate Capabilities of High-Speed Avalanche Photodiodes and a Review of the State-of-the-Art," **International Electron Devices Conf.**, Wash., D.C., Dec. 1973.

D. Meyerhofer, "Holographic and Interferometric Viewing Screens," **Appl. Opt.**, Vol. 12, No. 9, p. 2180, Oct. 1973.

B. P. Miller, G. A. Beck, and J. M. Barletta, "ERTS Two-Inch RBV Camera Performance Characteristics," **AIAA J. Spacecraft and Rockets**, Oct. 1973.

L. S. Napoli, J. J. Hughes, W. F. Reichert, and S. Jolly, "GaAs FET for High-Power Amplifiers at Microwave Frequencies," **1973 National Telecommunications Conf.**, Atlanta, Ga., Nov. 26-28, 1973.

J. Newman, "The Growing Importance of Costs and Ways to Maintain Cost Control on a Large Program in Today's Competitive Environment," **Proc. 21st Joint Engineering Management Conf.,** Oct. 25-26, 1973.

F. H. Nicoll, "Intense Recombination Radiation and Room Temperature Lasing in CdS Excited by High Voltage RF Current Pulses," **Appl. Phys. Lett.,** Vol. 2, No. 8, p. 465, Oct. 15, 1973.

M. Schlesinger and N. Feldstein, "Electron Microscope Investigations of Chemical Catalytic Systems for Plating onto Dielectric Substrates," **Electrochem. Soc. Mtg.,** Boston, Mass., Oct. 7-12, 1973.

D. L. Staebler, "Volume Holography, Science, and Application," **2nd International Conf. on Electrophotography,** Wash., D.C. Oct. 24-27 1973.

H. Staras, R. J. Klensch and J. Rosen, "A Microwave Automatic Vehicle Identfiication System," **IEEE Electrical and Electronics Conf.,** Chicago, Ill., Oct. 2, 1973.

R. A. Sunshine and N. Goldsmith, "Use of the Infrared Sensitivity of the Silicon Vidicon to Diagnose Semiconductor Problems," **IEEE 1973 Northeast Electronics Research and Eng. Mtg.,** (NEREM), Nov. 12-14, 1973.

C. R. Thompson, "An Ultra-High Rate Digital Tape Recorder for Spacecraft Applications," **International Telemetering Conf., Proc.,** Vol. 9, p. 220, Oct. 9-11, 1973.

C. R. Thompson, "A 40 MHz Multitrack Tape Recorder for Earth Observation Satellites," **International Telemetry Conf.,** Wash., D.C., Oct. 9-11, 1973.

M. Toda, S. Tosima, E. Shima, and T. Iwasa, "Variable Delay Devices Using Ferroelastic and Ferroelectric Crystal $Gd_2(MoO_4)_3$," **IEEE Trans. Sonics and Ultrasonics,** Vol. SU-20, No. 4, p. 376, Oct. 1973

J. L. Vossen, G. L. Schnable, and W. Kern, "Processes for Multilevel Metallization," **Amer. Vacuum Soc. Material Symp.,** New York City, Oct. 9-12, 1973.

A. L. Waksberg, "A Comparative Evaluation Between Internal External Polarization Modulation of Lasers," **IEEE J. Quant. Electron.,** Vol. 9. No. 11, Nov. 1973.

A. Waksberg, "Corrections to FM Laser Noise Effects on Optical Doppler Radar Systems," **IEEE Trans. Aerospace and Electron. Systems,** Vol. 9, No. 3, July 1973.

C. P. Wen, Y. S. Chiang, A. F. Young and A. Presser, "High-Frequency Electron Conductivity Mobility in Vapor-Base Homoepitaxial Silicon," **Appl. Phys. Lett.,** Vol. 23, No. 7, p. 390, Oct. 1, 1973.

R. K. Whener, "Soft Acoustic Modes in Elastic Layers with Electrostatic Surface Forces," **Swiss Phys. Soc. Mtg.,** Lugano, Switzerland, Oct. 19-20, 1973.

Patents Issued to RCA Inventors Fourth Quarter, 1973

October

P. R. Ahrens High Voltage Regulator (3,767,960)
J. F. Alves III Push-Pull Darlington Amplifier with Turn-Off Compensation (3,764,929)
T. G. Athanas and A. A. Anastasio Method of Making Beam Leads for Semiconductor Devices (3,765,970)
P. K. Baltzer Radiation Resistant Lithium Ferrite Cores (3,767,581)
R. L. Barbin Cathode-Ray Tube with Shadow Mask Having Random Web Distribution (3,766,419)
R. A. Bartolini and D. Karlsons Reduction of Non-Linear Spatial Distortion in Holographic System Employing Different Wavelengths for Recording and Playback (3,763,311)
O. Ben-Dov Circularly Polarized Antenna (3,765,023)
S. L. Bendell and C. A. Johnson Automatic Iris Control (3,767,853)
R. F. Buntschuh and H. G. Rouland Rate Aided Ranging and Time Dissemination Receiver (3,769,589)
T. W. Burrus Blanking Circuits for Television Receivers (RE27793)
T. H. Campbell, P. Schnitzler, and L. J. West Lattice Network Using Distributed Impedance Transmission Lines (3,768,047)
D. J. Carlson and J. B. George Circuit for Transmitting Digital Signals to Conventional Television Receiver (3,766,313)
S. B. Deal Cathode-Ray-Tube-Yoke Combination with at Least Two Spaced Bodies of Organic Thermoplastic Material Therebetween and a Method of Making Said Combination (3,764,740)
E. H. Del Rio and D. F. Pothier Self-Cleaning Read Head (3,763,352)
M. Ettenberg and V. M. Cannuli Method for Epitaxially Growing Layers of a Semiconductor Material from the Liquid Phase (3,767,481)
B. F. Floden Film Handling Apparatus (3,765,586)
P. Foldes Wideband Hybrid System (3,768,043)
G. S. Gordon Method of Preventing Inoperation of a Component by Loose Particles of Material (3,765,941)
F. B. Griswold Phase Measuring System (3,764,903)
F. B. Griswold Analog Phase Tracker (3,769,602)
S. E. Harrison and J. E. Goldmacher Direct Print-Out Photographic Optical Recording Media Comprising a Rhodamine Dye (3,767,408)
D. G. Herzog and C. W. Reno Optical Data Transmission System Employing Polarization-Shift, Multiple-Cavity Laser (3,766,393)
R. A. Ito Communications Between Central Unit and Peripheral Units (3,766,530)
L. B. Juroff Remote Control System for a Television Receiver (3,769,588)
H. Kressel and H. Nelson Method of Forming Region of a Desired Conductivity Type in the Surface of a Semiconductor Body (3,762,968)
R. D. Larrabee Method for Fabrication of Polycrystalline Films (3,767,462)
D. W. Luz Instant-On Circuitry for AC/DC Television Receivers (3,767,967)
R. J. Mason and N. R. Landry Waveguide Assembly Including a Toroid Having Dielectric Material Therein (3,768,040)

J. J. McArdle and R. L. Rauck High Voltage Hold Down Circuit (3,767,963)
R. S. Mezrich Enhanced Readout of Stored Holograms (3,767,285)
M. N. Norman Blanking Circuits for Television Receivers (3,763,315)
P. E. Norris and J. M. Shaw Method of Making MOS Transistors (3,766,637)
R. L. Pryor Multifunction Full Adder (3,767,906)
M. J. Shilling Interference Suppression Circuit (3,763,396)
M. J. Shilling and E. Peak Interference Suppression Circuits (3,763,395)
T. F. Simpson Color Image Reproducing Apparatus (3,767,845)
S. A. Steckler Direct-Coupled Triggered Flip-Flop (3,767,943)
J. A. Tourtellot Automatic Record Changer (3,762,723)
C. L. Upadhyayula and B. S. Perlman Temperature Compensation of Transferred Electron Amplifiers (3,768,029)
E. J. Von Makkay and J. J. Pesce Cutting Pliers (3,763,560)
H. R. Warren Slant Track Rotating Head Recorder-Reproducer System for Selective Retention of Special Information (3,766,328)
P. K. Weimer Digital and Analog Data Handling Devices (3,763,480)
L. J. West Transmission Line Using a Pair of Staggered Broad Metal Strips (3,769,617)
H. E. White Linearity Correction Circuit for a Cathode Ray Tube (3,763,393)

November

J. J. Amodei and D. L. Staebler Process for Fixing Holographic Patterns in Electro-Optic Crystals and the Crystals Produced Thereby (3,773,400)
D. S. Bond Apparatus and Method for the Automatic Navigation of a Sailing Vessel (3,771,483)
T. J. Brady Cathode Ray Display Intensity Control Circuit (3,775,637)
J. G. Butler and A. Mack Universal Data Quality Monitor (3,771,059)
D. J. Carlson Modulator System (3,775,554)
R. J. Clark Multiple Terminal Display System (3,774,158)
R. E. Ernst and S. Yuan Microwave Double Balanced Mixer (3,772,599)
R. A. Gange Light Modulator (3.772,612)
P. J. Griffin Metal Mask Screen for Screen-Printing (3,769,908)
B. A. Hegarty and L. H. Trevail High Heat Dissipation Solder-Reflow Flip Chip Transistor (3,772,575)
R. H. Hughes In-Line Electron Gun (3,772,554)
S. W. Kessler, Jr. and R. F. Keller Method of Making a Electrically-Insulating Seal Between A Metal Body and a Semiconductor Device (3,769,688)
H. B. Law Method for Making an Image Screen Structure for an Apertured-Mask Cathode-Ray Tube Using a Mask Having Temporary Apertures (3,770,434)
F. J. Marlowe and C. M. Wine Electron Beam Addressable Memory System (3,774,116)
W. E. Martin Apparatus for Remotely Measuring the Temperature and Emissivity of a Radiant Object Independent of the Object's Radiant Surface Property (3,770,973)
J. F. Schanne and F. G. Nickl Article Identification Apparatus (3,770,944)
I. Shidlovsky Cathodochromic Image Screen and Method for Preparing Cathodochromic Sodalite for Said Image Screen (3,773,540)
W. I. Smith Dual Channel Balanced Line Type Modulator (3,772,601)
W. I. Smith Balanced Line Type Pulser Circuit (3,772,613)
D. F. Wright and R. A. Rubenstein Braking Arrangement Which Includes Hydraulic Pump (3,771,919)

December

A. F. Arnold Multilayer Heat Sink (3,780,795)
V. Auerbach Controllable Heat Pipe (3,776,304)
G. A. Cutsogeorge Voltage to Pulse Width Converter (3,781,870)

E. B. Davidson Stabilized Photoresist Composition (3,776,736)
W. J. Hannan Gated Holographic Coding System for Reducing Alignment Requirements (3,778,128)
A. G. Lazzery Damping Means for Ultrasonic Transmitters (3,777,700)
A. F. McDonie, R. D. Faulkner and J. L. Rhoads Non-Thermionic Electron Emissive Tube Comprising a Ceramic Heater Substrate (3,777,209)
P. B. Pierson Digitally Variable Delay Time System (3,781,722)
E. C. Ross Storage Circuit Using Multiple Condition Storage Elements (3,781,570)
R. A. Shahbender Method of Making a Magnetic Recording Head (3,777,369)
R. L. Spalding Electron Gun and Method of Assembly (3,777,210)
H. Staras and J. Shefer Harmonic Radar Detecting and Ranging System for Automotive Vehicle (3,781,879)
D. H. Vilkomerson Holographic Memory with Light Intensity Compensation Means (3,781,830)
A. Waksberg and J. I. Wood Automatic Optical Bias Control for Light Modulators (3,780,296)
R. Williams Apparatus for and Method of Reproducing an Electrostatic Charge Pattern (3,776,639)
C. M. Wright Keyboard Encoder (3,778,815)

AUTHORS

James E. Carnes received the B.S. degree from Pennsylvania State University, University Park, in 1961, and the M.A. and Ph.D. degrees in electrical engineering from Princeton University, Princeton, N. J., in 1967 and 1970, respectively. His Ph.D. dissertation was an investigation on photo-induced currents and charge transport in polyvinylcarbazole, an organic polymer. He was in the U. S. Navy from 1961 to 1965. During the summers of 1966 and 1967 he investigated metallic contacts and dc electroluminescence in strontium titanate at RCA Laboratories, David Sarnoff Research Center, Princeton, N. J., which he joined as a member of the technical staff in 1969. Since that time he has studied electrical breakdown, conduction, and interface properties of various insulating films or silicon and is currently involved in the investigation of charge-coupled devices

Dr. Carnes is a member of the American Physical Society, Tau Beta Pi, Phi Kappa Phi, and IEEE.

Walter F. Kosonocky received the B.S. and M.S. degrees in electrical engineering from Newark College of Engineering, Newark, N. J., in 1955 and 1957, respectively, and the Sc.D. degree in engineering from Columbia University, New York, N. Y. in 1965. Since June 1955 he has been employed at RCA Laboratories, Princeton, N. J., where he has conducted research on application of new phenomena and new devices for information processing systems. This work has included ferrite memory systems, parametric digital devices, tunnel-diode circuits, tunnel-diode and transistor circuits, pattern-recognition systems, applications of lasers for digital systems (including a study of saturable absorbers for Q-switched lasers and semiconductor laser digital devices), optical hologram memory systems and page composition, optically controlled p-MOS circuits, and a liquid-crystal image converter. Presently he is working on the development and applications of charge-coupled devices.

Dr. Kosonocky is a member of Sigma Xi, Tau Beta Pi, Eta Kappa Nu, and a senior member of IEEE.

Michael G. Kovac received the B.S. degree from the University of Notre Dame, Notre Dame, Ind., in 1963, and the M.S. and Ph.D. degrees from Northwestern University, Evanston, Ill., in 1967 and 1970, respectively, all in electrical engineering. His research activities have included investigations of an x-ray imaging system based on the electron beam scanning of a mosaic target coupled to a gas-filled detection chamber, of x-ray-induced secondary electron emissions from metal-insulator layers, and of various aspects of a two-dimensional, beam-scanned ultrasonic imaging system. He has worked at the General Electric Industry Control Department, Salem, Va., and since 1970 has been associated with RCA Laboratories, Princeton, N. J., where he has been concerned with silicon and thin-film self-scanned imaging systems. His work has included investigations of both x-y addressed image sensors and of charge-transfer image sensors. He is presently with Dytron, Inc., Waltham, Mass.

Dr. Kovac is a member of Tau Beta Pi, Eta Kappa Nu, and Sigma Xi.

Aaron W. Levine graduated with a B.A. from Yeshiva University in 1963, an M.A. from the City College of the City University of New York in 1966, and a Ph.D. in physical organic chemistry from Seton Hall University in 1970. Dr. Levine worked in the chemical industry and was a teacher of chemistry until 1969, when he joined RCA Laboratories, Princeton, N. J. His research interests include the mechanisms of reactions of organic compounds and polymers, the interaction of ionizing radiation with polymers, organic electrochemistry, and liquid crystals. Dr. Levine is a member of the American Chemical Society, The Society of Plastics Engineers, The Society of Photographic Scientists and Engineers, and is listed in American Men and Women of Science.

Peter A. Levine received the B.S. and M.A. degrees from Cornell University, Ithaca, N. Y., in 1967 and 1968, respectively. He joined RCA Laboratories, Princeton, N. J., in 1968, working in the area of Impatt and Trapatt diode microwave devices, with particular emphasis on noise properties. Most recently, he has been engaged in the development of charge-coupled devices.

Stewart Perlow received his B.E.E. degree from the College of the City of New York in 1963, and his M.S.E.E. degree from the Poytechnic Institute of Brookyn in 1970. From 1963 to 1967, he was employed by RCA's Advanced Communications Laboratory in New York. In 1967 he left RCA to become a co-founder of National Electronics Laboratories. Upon acquisition of National Electronics Laboratories by Harvard Industries, Mr. Perlow became a Project Manager and subsequently Chief Engineer at KMC Semiconductor Corporation, a division of Harvard Industries. His work has been in the field of microwave solid state devices and ultra low noise UHF amplifiers. In January of 1973 Mr. Perlow joined the RCA Laboratories as a member of the Technical Staff. He is presently involved in UHF and microwave work on ceramic substrates.

Mr. Perlow is a member of Eta Kappa Nu and the IEEE.

E. B. Priestley received his B.Sc. degree in Chemistry from the University of Alberta in 1965 and his Ph.D. degree in Chemical Physics from the California Institute of Technology in 1969. He spent two years as a Research Fellow in the Department of Engineering and Applied Physics at Harvard University, and in 1971 joined the technical staff of the Physical Electronics Laboratory at the David Sarnoff Research Center, Princeton, N. J. Dr. Priestley has been studying long-range orientational molecular ordering in nematic and smectic liquid crystals using a Raman scattering technique he developed while at Harvard University. At present he is using Raman scattering and inelastic electron tunneling spectroscopy to investigate chemisorption of liquid crystal and surfactant molecules on a variety of substrates in an effort to understand the forces responsible for surface alignment of liquid crystals.

Dr. Priestley is a member of the American Physical Society and the American Association for the Advancement of Science.

R. L. Rodgers, III, received his training in physics and electrical engineering at the Polytechnic Institute of Brooklyn. He has been working on electro-optic imaging devices since joining RCA at RCA Laboratories in 1964. He was instrumental in the conception and design of RCA's Silicon Vidicon and Silicon Intensifier Target (SIT) camera tubes. He transferred to the Electro-Optic Products Advanced Technology area in Lancaster in 1969 to continue work on silicon camera tubes and LLLTV cameras using these tubes, resulting in the development of a photoelectron noise limited I-SIT camera. He was responsible for the development of an effective nonblooming silicon target design and new lower cost fabrication techniques for silicon targets. Most recently he has been involved with Charge Coupled Devices (CCDs) for imaging and memory applications. Early in 1974, he was promoted to his present position, Manager, CCD Manufacturing and Engineering, Electro-Optic Products, Lancaster, Pa. Mr. Rodgers received an RCA Laboratories Achievement Award in 1968.

Frank V. Shallcross received an A.B. with honors in chemistry from the University of Pennsylvania, Philadelphia, in 1953. He did graduate research in X-ray crystallography and received a Ph.D. in physical chemistry from Brown University, Providence, R.I., in 1958. He joined RCA Laboratories in 1958 as a Member of the Technical Staff. He has done research on the fabrication and evaluation of thin-film photoconductors, and semiconductors, photoconductive television camera tubes, thin-film active devices, and charge-coupled devices. He has participated in the development of a variety of self-scanned image sensors including thin-film photoconductive arrays and silicon arrays based on bipolar, MOS, and CCD technologies, and has worked on the application of charge-transfer devices to signal processing.

Dr. Shallcross is the recipient of two RCA Laboratories Achievement Awards. He is a member of the American Chemical Society, the American Institute of Chemists, Phi Beta Kappa, Sigma Xi and the American Association for the Advancement of Science.

Ping Sheng received his B.Sc. degree in Physics (with honors) from the California Institute of Technology in 1967. He received his Ph.D. in Physics from Princeton University in 1971. After spending two years at the Institute for Advanced Study, Princeton, N. J., as a visiting member of the School of Natural Sciences, Dr. Sheng joined the RCA David Sarnoff Research Center in 1973 as a member of the Physical Electronics Research Laboratory. Dr. Sheng has done research on a variety of subjects. As a graduate student his research effort was mainly directed toward polaron theory and ferromagnetic transmission resonance. As a result of his work on the transmission resonance a new technique was developed for measuring the magnetic critical exponent β. While at the Institute for Advanced Study, Dr. Sheng has developed a theory for electron transport in granular metals and has done research in the theory of liquid crystals. Currently he is engaged in research on the physical properties of granular metals and the theory of liquid crystals.

Dr. Sheng is a member of the American Physical Society.

Issie P. Shkarofsky graduated in 1952 from McGill University, Montreal with a B.Sc. degree and first class honours in physics and mathematics. In the following year, 1953, he obtained his M.Sc. degree, conducting his research at the Eaton Electronics Research Laboratory, McGill University, in the fields of microwave optics and antennas. He then joined the microwave tube and noise group at the Eaton Electronics Research Laboratory, McGill University, and received his Ph.D. degree in 1957 with a thesis on modulated electron beams in space-charge-wave tubes and klystrons. After graduation, he joined the Research Labratory of RCA Limited, Montreal, where he has participated in research on microwave diffraction, millimeter waves, obstacle gain, laser applications, electromagnetic wave interaction with plasmas, plasma kinetics, and plasmas in space. In 1973 he became a R&D fellow at the RCA Research and Development Laboratories, presently in the Physical Electronics Laboratory. In the field of plasma and space studies his particular interest has been in the following topics: plasma transport coefficents, collisional effects in plasmas (slightly, partially and strongly ionized), Boltzmann and Fokker-Planck theory and appropriate expansions, bremsstrahlung, magnetohydrodynamics, re-entry plasma physics, generalized Appleton-Hartree equation for the ionosphere, laboratory simulation of geophysical phenomena such as the interaction between the solar wind and the magnetosphere and the sheaths around satellites, cyclotron harmonic resonances and related dispersion effects, diagnostics of plasmas by laser scattering, nonlinear mixing of plasma modes, the accuracy of Langmuir probes on satellites, VLF sheath admittance of antennas in the ionisphere, high power laser interaction with matter, turbulence and fusion.

Dr. Shkarofsky is a member of the Canadian Association of Physiclsts, of the American Physical Society, the American Geophysical Union, and of the National Research Council Advisory Committee on Physics. He is a professeur invité du Centre de Recherche INRS-Energie, Un. du Québec, and he is also the co-leader of the Task Force on Toroidal Machines for Project Fusion Canada.

Peter J. Wojtowicz received his B.Sc. degree in chemistry (with highest honors) from Rutgers University in 1953. He received his M.S. in chemistry in 1954 and his Ph.D. in physical chemistry in 1956 from Yale University. He was a National Science Foundation Predoctoral fellow while at Yale, 1953-56. His thesis was concerned with the statistical mechanics of the order-disorder phenomenon in solids and the theory of molten salts and fluid mixtures. Dr. Wojtowicz joined the RCA Laboratories in 1956. He is a Member of the Technical Staff of the Physics and Chemistry of Solids Group of the Physical Electronics Research Laboratory. During 1966-67 he was acting head of the General Research Group. His research effort while at RCA has been directed chiefly toward the theory of magnetic materials including the quantum and statistical mechanics of the thermal, structural, and magnetic properties of these substances. This work included the theory of the cooperative Jahn-Teller effect, the statistical mechanics of magnetic interactions and phase transitions, the theory of magnetic semiconductors, the theory of granular ferromagnetic metals, and the theory of the application of ferrites and garnets to various magnetic devices. He is currently engaged in the theory of liquid crystals and liquid-crystal phase transformations. Dr. Wojtowicz is the recipent of two RCA Laboratories Achievement Awards for the years 1962 and 1966. He is a fellow of the American Physical Society and a member of Sigma Xi and Phi Beta Kappa.

STATEMENT OF OWNERSHIP

Statement of Ownership, Management and Circulation (Act of October 23, 1962, Section 4369, Title 39, United States Code.)

1. Date of filing: October 19, 1973. 2. Title of publication: RCA REVIEW. 3. Frequency of issue: Quarterly. 4. Location of known office of publication: RCA Laboratories, Princeton, New Jersey, 08540. 5. Location of headquarters or general business offices of the publishers: RCA Laboratories, Princeton, New Jersey, 08540. 6. Names and addresses of Publisher and Editor: Publisher, RCA Laboratories, Princeton, New Jersey, 08540; Editor: R. F. Ciafone, RCA Laoora-tories, Princeton, New Jersey, 08540. 7. Owner: RCA Corporation, 30 Rockefeller Plaza, New York, New York, 10020; Merrill, Lynch, Pierce, Fenner & Smith, 70 Pine Street, New York, New York, 10005; Cudd & Company, c/o Chase Manhattan Bank, 1 Chase Manhattan Plaza, New York, New York, 10005; Martin B. Seretean, c/o Coronet Industries, Box 1248, Dalton, Georgia, 30720; Burl Jackson Bandy, c/o Coronet Industries, Box 1248, Dalton, Georgia, 30720; TNOM & Com-pany, P.O. Box 577 Central Station, St. Louis, Missouri, 63188.

I certify that the statements made by me above are correct and complete.

Ralph F. Ciafone, Editor